Evaluating the improvement of atmospheric aberration corrections with the use of adaptive optics

Enabling inter-island communication through quantum encrypted optical communications

Serena Maroquin

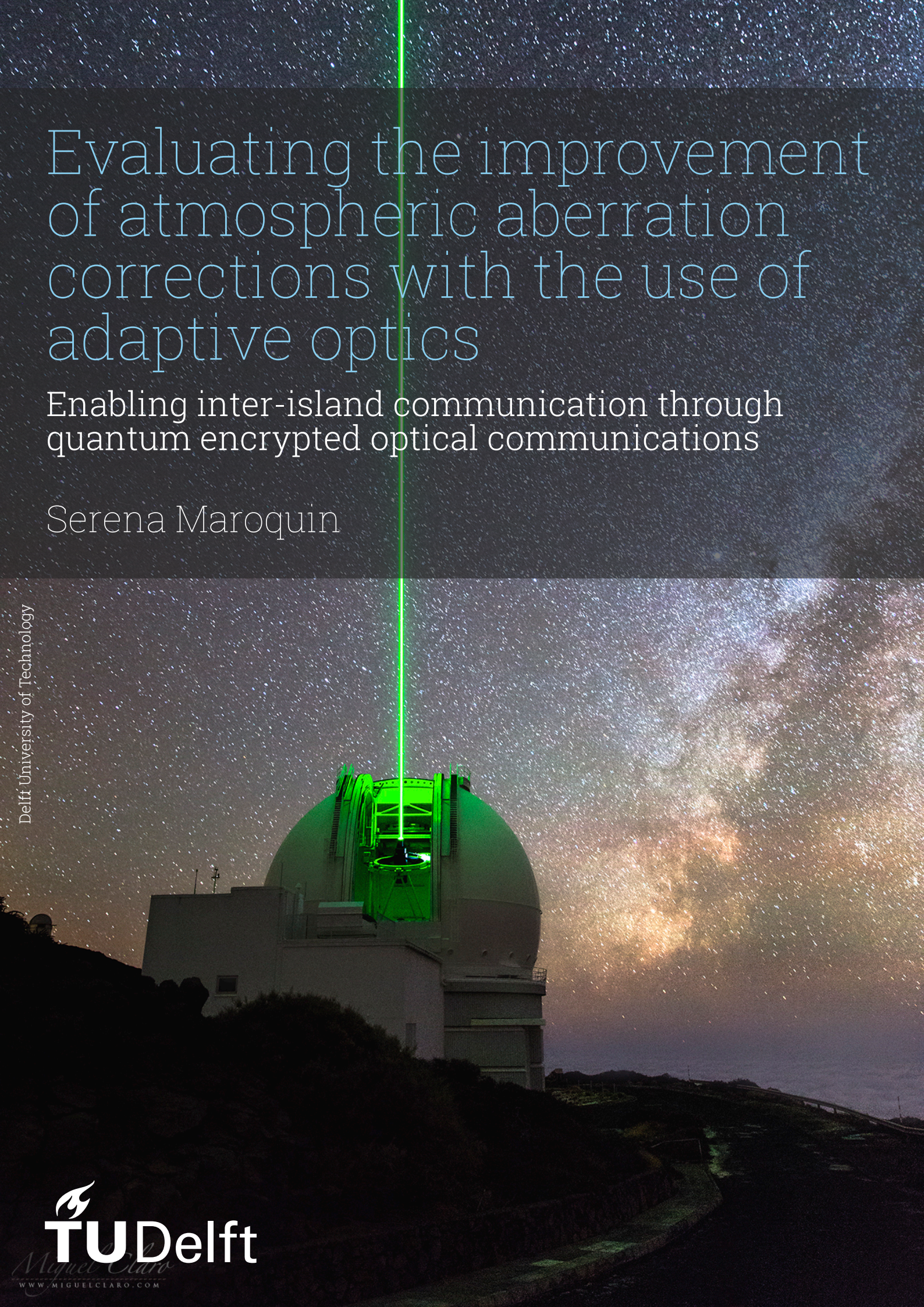

Delft University of Technology

TU Delft

Miguel Claro
WWW.MIGUELCLARO.COM

Evaluating the improvement of atmospheric aberration corrections with the use of adaptive optics

Enabling inter-island communication through quantum encrypted optical communications

Master thesis

Author:
Serena Maroquin
Student Number:
4834445
Supervisors:
Dr.ir. Erwin Mooij & Dr. Luis Fernando Rodriguez Ramos
Department of Space Engineering
Faculty of Aerospace Engineering
Delft University of Technology

July 31, 2023

Cover Image: The milky way seen from the observatory of “el Teide” in Tenerife, the Canary Islands, available at https://www.miguelclaro.com/wp/portfolio

Preface

This thesis has been written as part of the completion of the Masters degree of Aerospace Engineering, for the track space flight at Delft University of Technology. The thesis evaluates the improvement of the atmospheric aberrations corrections performed through the use of adaptive-optics systems.

During the thesis, experimental tests where performed using the laboratories made available by the Canarian Institute of Astrophysics (IAC) in Tenerife, Spain. I would like to thank dr. Luis Fernando Ramos for his supervision during the time at IAC. Moreover, I would like to thank Jorge Socas Negrin and Joan Torras Estruch for the help along the simulations and the experimental set-up.

In Chapter 2, the reader can find background information about the thesis topic, as well as the science case followed by the research question and the requirements. Then, Chapter 3 will describe the physical environment encountered by the TOGS when placed on el Teide and communicating with its target. Chapter 4, addresses the laboratory test set-up, including all the details of the HW components used. Subsequently, Chapter 5 focuses on the SW simulations performed. Chapter 6 includes all the steps carried out for the calibration of the experimental test set-up. Those who are interested in the controller design should read Chapter 7. Once the controller is designed, a sensitivity analysis and a robust design are performed. The results will be presented in Chapter 8. Finally, the conclusions together with recommendations for future work are given in Chapter 9.

Finally, I would like to give my sincere gratitude to my supervisor dr. Erwin Mooij for the guidance and support along the entire thesis. Also, I would like to thank dr. Bert Vermeersen for chairing the thesis defence as well as dr. Alessandra Menicucci for being the examiner.

Summary

Free space optical communication (FSOC) is the wireless transmission of data through a modulated optical beam directed through free space, without fibre optics or other optical systems guiding the light. Using Adaptive Optics (AO) for free-space propagation stabilises the optical signal on a detector significantly. Furthermore, it maximises the received signal by returning near-diffraction limited performance to the optical system, and stabilising the channel transmission and noise.

The Canarian Institude of Astrophysics (IAC) will be developing a new Transportable Optical Ground Station (TOGS). It is a telescope that is intended to be used for quantum key distribution in a number of events. The main event that will be focused upon is to enable inter-island communication between the observatory of “el Teide” in Tenerife, and “el Roque de los Muchachos” observatory in la Palma. AO will be used to compensate for the effects of the atmospheric turbulence to improve the efficiency of the signal coupling to a Single-Mode fibre (SMF). The use of AO as an important part of the ground station is justified by the improvement expected in the coupling efficiency to SMFs . However, the control of an adaptive-optics system can greatly affect the communication between the target and the ground station. Therefore, the goal of this thesis will be to design a controller for an AO system that will be used for the new Transportable Optical Ground Station (TOGS) of IAC. This thesis is supposed to tackle the following research question:

What is the improvement of optical communication when decreasing the atmospheric aberrations with the use of adaptive optics?

Software simulations were performed using the open source software OOMAO. Here the AO system’s components were simulated such that it consisted of the same properties as the hardware components used in the experimental set-up at a later stage. After running the simulations, it was observed that the system’s performance increased with a decreasing atmospheric turbulence, meaning that the quality of the image defined with the Strehl ratio increased as well as the fibre-optics coupling performance. The Strehl ratio is obtained by dividing the intensities of the closed-loop by the open-loop image. However, the quality of the corrections starts to deteriorate after reaching a certain minimum Fried parameter, where the atmospheric aberrations are almost zero. The Fried parameter specifies the severity of the atmospheric aberrations. The higher the Fried parameter, the lower the atmospheric aberrations. At this point, the retrieved fibre-optics coupling performance is less than the fibre-optics coupling performance achieved when atmospheric perturbations are present in an open-loop simulation.

Then, the control system was designed to increase the correction of the atmospheric

aberrations by the AO system. The original I-controller did not meet the predefined requirements, where a minimum fibre-optics coupling of 40% must be attained for aberrations with a Fried parameter between 6 and 20 cm. Therefore, a linear proportional, integral, and derivative (PID) controller, and a non-linear (INDI) controller was designed and implemented. Once the sensitivity analysis of both controllers was performed and a robust design was carried out to optimise the PID-controller performance only, it was seen that the requirements were met. More specifically, the INDI-controller resulted in a better fibre-optics coupling than the PID-controller under the same conditions. For example, for a Fried parameter of $r0$ = 6 cm, the coupling was 82.7% with a PID-controller, whereas the INDI-controller resulted in a coupling of 89.3%. When the aberrations are extremely low, it is seen that, for a predefined actuator stroke, the closed-loop performance for both controllers is lower than the open-loop performance due to the system becoming saturated. Furthermore, a frequency analysis was carried out and it was seen that both controllers corrected for the atmospheric aberrations, which is the frequency area of interest. Additionally, it was proven that the designed controllers resulted in a robust system.

Next, to verify the performance of the designed controller in a closed-loop simulation with the chosen hardware component, an experimental test set-up was created in IAC's laboratories. It consisted of a Laser Guide Star (LGS) to simulate the point source, an atmospheric turbulence simulator, a Deformable Mirror (DM), a Wavefront Sensor (WFS), and an Multi-Mode Fibre (MMF) to retrieve the fibre-optics coupling. The results showed that the fibre-optics coupling increased from 70.0% to 85% for an increasing Fried parameter (from 7.8 m to 15.5 cm), which was expected as it is paired to a lower atmospheric aberration. When the Fried parameter becomes too high, the system reaches again a saturation level. This causes the fibre-optics coupling (14.4%) to be below the initial open-loop fibre-optics coupling retrieved (60.0%) for a maximum actuator stroke of 0.5. Therefore, the actuator stroke had to be limited to a maximum of 0.1 to increase the coupling to 74.4%. These results coincide with the observed behaviour of the AO system in the simulations carried out with OOMAO.

There are a few differences between the simulations and the test set-up. First, the AO system in the laboratory is not connected to an actual telescope, which scales the incoming point-source image. Adding a telescope to the system would require proper optical alignment procedures to retrieve the image. Moreover, the experimental set-up takes place within a controlled environment. In real life, the TOGS will experience uncontrolled atmospheric perturbation. Additionally, since the distance between the LGS and the WFS will significantly be increased, the incoming power of the laser will be altered and other effects, such as scintillation, will take place. However, extrapolation of the data should result in similar results as the one obtained from the laboratory measurements. Finally, the largest difference between the experimental test-set-up and the TOGS is that the results performed do not correspond to a real-time controller, which is what is eventually needed for the TOGS, to correct for the fast changing conditions.

To conclude, the main research question can be answered as follows. The improvement of optical communication when correcting for the atmospheric aberrations with the use of AO, can be achieved by considering several factors. First, it was concluded from the simulations that, with a right controller, the AO system increases both the retrieved fibre-optics coupling performance and the image quality significantly. The improvements in the fibre-optics coupling performance was confirmed with an experimental test set-up that included the same hardware components chosen for the TOGS. However, the type of controller used to send the actuator commands to the DM, influences the performance of the AO-system. The designed INDI-controller resulted in the most improved performance.

Contents

Nomenclature

Abbreviations

Abbreviation	Definition
APD	Avalanche Photon Detectors
API	Application Programming Interface
ARTEMIS	Advanced Relay and TEchnology MISsion
AO	Adaptive Optics
AU	Astronomical Unit
CM	Command Matrix
CMOS	Complementary Metal Oxide Semiconductor
CPU	Central Processing Unit
DARC	Durham Adaptive optics Real-time Controller
DM	Deformable mirror
ECC	Elliptic Curve Cryptography
ELT	Extremely Large Telescopes
ESA	European Space Agency
FFT	Fast Fourier Transform
FSM	Fine Steering Mirror
FSOC	Free Space Optical Communication
FWHM	Full-Width Half Maximum
GEO	Geostationary Earth Orbit
GUI	Graphical User Interface
HSR	High Spatial Resolution
IAC	Instituto de Astrofisica de Canarias
INDI	Incremental Non-linear Dynamic Inversion
LD	Laser Diode
LED	Light Emitting Diode
LEO	Low Earth Orbit
LGS	Laser Guide Star
MC	Monte Carlo
MIIMO	Multi-Input-Multi-Output
MMF	Multi-Mode Fibre
NDI	Non-linear Dynamic Inversion
NGS	Natural Guide Source

Abbreviation	Definition
OGS	Optical Ground Station
OOMAO	Object–Oriented Matlab Adaptive Optics
OPD	Optical Path Difference
OTF	Optical Transfer Function
PID	Proportional Intergral Derivative
PQC	Post-Quantum Cryptography
PSD	Power Spectral Density
PSF	Point Spread Function
QKD	Quantum Key Distribution
RSA	Rivest-Shamir-Adleman
SCAO	Single Conjugate AO
SMF	Single-Mode Fibre
SNR	Signal to Noise Ratio
SNSPDs	Superconducting Nanowire Single-Photon Detectors
STD	Standard Deviation
TIS	Total Integrated Scatter
TOGS	Transportable Optical Ground Station
TTL	Transistor-Transistor-Logic
WFS	Wavefront Sensor

Latin symbols

Symbol	Definition	Unit
B	Control input matrix	various
B	Bezier curves	m
c	Actuator coefficients	μm
C	Command matrix	-
e	Error	various
f	Focal length	m
f	System dynamics	various
G	State dependent control matrix	various
H	Transfer function	-
I	Image	various
I	Intensity	Ws^{-1}
k	Number of array elements	-
k	Time step	s
K	Gains	-
K_v	Modified Bessel function	m
L	Luminosity	W
L_0	Outer scale length	m
M	Magnitude	-
M	Mode matrix	-
n	Power of radial polynomial	W
N	Measurement points	-
P	Mesh points	-
P	Covariance matrix	-
$\mathbf{Q_k}$	Process noise matrix	-
r	Spatial vector	m
r	Radius of curvature	m
r_0	Fried parameter	m
R	Reference image	W
$\mathbf{R_k}$	Measurement noise matrix	dB
s	Variance	-
S	Slopes	-
St	Strehl ratio	-
S	Singular values matrix	-
t	Spacing	m
t	Time	s
T	Sampling time	s
T	Threshold	-
T	Toeplitz matrix	-
u	Horizontal displacement	m
u	Control output	µm
U	Left singular vectors	m
u	Input vector	various
u	Control vector	various
v	Vertical displacement	m

Symbol	Definition	Unit
V	Right singular vectors	m
w	Angular frequency	Hz
x	State vector	m
z	Measurement vector	various

Greek symbols

Symbol	Definition	Unit
α	Displacement angle	rad
Γ	Gamma function	-
δ	Surface roughness	rms
ϵ	Linear approximations of noise parameters	dB
θ	Angle	rad
θ	Dynamics	various
λ	Incident light	rad
λ	Wavelength	m
ν	Virtual input	various
ν	Order of Bessel function	-
$\mathbf{\Pi}$	Projection matrices	various
ρ	Radius image	m
ρ	Radius in the image phase	rad
σ	Variance	-
ϕ	Phase	rads

CHAPTER

1 Introduction

Free space optical communication (FSOC) is the wireless transmission of data through a modulated optical beam directed through free space, without fibre optics or other optical systems guiding the light.

FSOC systems were initially designed for secure and long-distance communication, and mainly targeted ground–satellite or satellite–satellite communication, but have also been used for other purposes, such as enabling communications between buildings or even between naval ships (Chen, 2022).

The observatory of "el Teide" in Tenerife and "el Roque de los Muchachos obsrvatory" in la Palma are the largest observatories in Europe, and are located on the Canary islands. They are being managed by the Canarian Institute of Astrophysics (IAC) (Sanchez, 1985). The telescopes that have been installed have multiple purposes, such as observing exoplanets, cosmic rays, cosmic particles, but also to communicate with satellites.

More specifically, the Optical Ground Station (OGS), built by the European Space Agency (ESA), was part of the long-term efforts for research in the field of inter-satellite optical communications. The original purpose of the station, equipped with a telescope, was to perform the in-orbit tests of laser telecommunication terminals on board satellites in Low Earth Orbit (LEO) and GEO (Berkefeld et al., 2010).

Since November 2001, the bidirectional link between the OGS and the GEO satellite ARTEMIS has been established in more than 100 successful sessions. This is the world's first stable free optical laser link ground-satellite. The purpose of this program was the analysis of the effect of atmospheric turbulence on optical communications between ground stations and satellites in GEO (Garcia-Talavera et al., 2002). Additionally, since 2002, a sodium Laser Guide Star (LGS) has been implemented by the High Spatial Resolution (HSR) group in the IAC to analyse the short/long term variations of the height, width and density of the sodium mesospheric layer. This study is part of the first generation of Adaptive Optics (AO) instruments development. Using AO for free-space propagation stabilises the optical signal on a detector significantly, and maximises the received signal by returning near-diffraction limited performance to the optical system and stabilising the channel transmission and noise (Reyes et al., 2005).

An AO system consists of three main components. The first one is a sensor that measures the aberrations caused by the atmosphere, known as a Wavefront Sensor (WFS). The second one is a Deformable Mirror (DM), which consists of a thin membrane with actuators underneath it to adjust the surface curvature of the mirror. This allows to compensate for the aberrations and improve the output quality. Finally, a controller has to be implemented to steer the actuators of the DM, which in turn forms a closed loop system between the sensor and the DM (Spohn et al., 2014).

IAC will be developing a new Transportable Optical Ground Station (TOGS). It is a telescope that is intended to be used for quantum key distribution in a number of events. The main event that will be focused upon is to enable inter-island communication between the observatory of “el Teide” in Tenerife, and “el Roque de los Muchachos” observatory in la Palma. AO will be used to compensate for the effects of atmospheric turbulence to improve the efficiency of the signal coupling to a Single-Mode fibre (SMF). It is expected that the use of AO will improveme the coupling efficiency to SMFs . However, the control of an adaptive-optics system can greatly affect the communication between the target and the ground station. Therefore, the goal of this thesis will be to design a controller for an AO system that will be used for the new Transportable Optical Ground Station (TOGS) of IAC. The following research question will be addressed:

What is the improvement of optical communication when decreasing the atmospheric aberrations with the use of adaptive optics?

This research question is what drives the research. To answer the research question, it is split into several sub-questions, which deal with the control of the instrument:

1. **How can software implementations of the system help in predicting the controller performance of the deformable mirror within the adaptive optics system?**
   Software simulations will be performed to investigate the behaviour of the controller on a predefined AO system before testing in the laboratory. The results will be compared to the experimental results.

2. **What is the best way to steer a deformable mirror?**
   The DM is the hardware component that corrects for the aberrations in the AO system. Therefore, the controllers that will be designed will aim to steer the DM actuators and correct for the aberrations. First, the original linear I-controller will be evaluated to observe its performance and check whether the requirements are met. Then, two different controllers will be considered to improve the correction of the aberrations using the DM in the AO system. The first one is a linear PID-controller that will be designed and verified using the experimental set-up. The controller will be optimised using a robust design method where the use of factorial design will be applied.

3. **To what extent can the controller performance be improved with the use of non-linear control techniques?**
   Once the linear controller is evaluated, a non-linear controller will be considered and its performance will be compared to the results retrieved with the PID-controller.

4. **What kind of experimental set-up is needed to test the deformable mirror?**
   This thesis allows to test the simulations created with the software into hardware with the available components in the laboratories of IAC. To do this, the test set-up has to be designed and adjusted based on the requirements and available hardware components.

5. **Is the test set-up representative with respect to the transportable optical ground station?**
   The test set-up has to be designed such that is could be used for the TOGS. IAC’s hardware components will be provided to test in the lab, which are the same ones that will be used for the TOGS at a later stage.

To answer these research questions, the objectives for this thesis will consist of the following steps:

1. **Develop a simulator to test the controllers for the adaptive-optics system.**
   This will enable the analysis of the behaviour of the designed controllers prior to its application on the hardware components. Moreover, it will allow the performance of a sensitivity analysis for both the PID- and INDI-controller. Also, a robust design method using factorial design can be implemented using the simulation environment.

2. **Design and build a hardware set-up in the laboratories of IAC to test the control system.**
   To test whether the system will work when applied within a telescope, the system has to be tested first within a laboratory environment. IAC offers the facilities and the hardware equipment to test the PID-controller.

3. **Compare the results of both the simulations and test set-up.**
   Once the PID-controller is tested using an experimental test set-up, the results can be compared to the ones retrieved from the simulations. Moreover, the results of the simulations using the INDI-controller can be compared to the simulated results with a PID-controller.

4. **Formulate specifications on how to use both environments when designing the controller for the AO system.**
   The thesis will formulate how both the simulations and the experimental test set-up were created, and used when the control system was designed and tested.

The thesis will have the following structure. In Chapter 2, background information will be given about optical communication and the use of adaptive optics, as well as the science case followed by the requirements. Then, Chapter 3 will describe the physical environment encountered by the TOGS. In Chapter 4, the laboratory test set-up will be formulated, including all the details of the hardware components. Subsequently, Chapter 5 focuses on the software simulations performed, where each part of the AO system is touched upon. Next, Chapter 6 includes all the steps performed for the calibration of the experimental test set-up, which accounts for most verification tests performed in the laboratory. Moreover, the additional verification tests are stated, together with the sensitivity analysis of the hardware components. The controller design will be specified in Chapter 7. This includes the design of both the PID-controller and the INDI-controller. Moreover, the gain tuning is stated. Once the controllers are designed, the sensitivity analysis is carried out, and a robust design analysis is performed. After the set-up and the simulations are explained, along with the calibration process and the controllers, the results can be obtained for both the simulations and the experimental test set-up. These will be presented in Chapter 8, where a comparison will be made between the results. Finally, the conclusions together with the recommendations are given in Chapter 9.

CHAPTER

2 Background

Free space optical communications have been gaining relevance in the telecommunications field during the last years. They can provide a larger bandwidth than communications through radio-frequency and make much better use of mass, power, and physical dimensions. It is expected that laser-optics communications will have a large impact on the market soon. The use of narrower beams will make interception of communications more difficult, but the effect of weather and other meteorological phenomena can eventually make those communications impossible. Optical communications can also be used for the distribution of secret cryptographic keys, a relatively new field that has added a lot of relevance to the technology. The use of an AO system allows for compensation of the effects caused by atmospheric turbulence.

In this chapter, background information will be given to comprehend how an AO system works and can be controlled. In Section 2.1, the general functioning of a telescope system is described. Then, Section 2.2 provides an explanation about free space optical communications and its main components. Furthermore, a description of adaptive optics is given in Section 2.3. Section 2.4 focuses on fibre-optics coupling, which is the way how information is retrieved from the optical systems. The use of quantum optics communication is touched upon in Section 2.5. Next, the science case related to this thesis is presented in Section 2.6. Finally, the system requirements are given in Section 2.7.

2.1 Telescopes

A telescope is a tool that is used to see faraway objects. Most telescopes, work by using curved mirrors to gather and focus light from the night sky. The light source can be either a far away Natural Guide Source (NGS), such as a star, or a Laser Guide Source (LGS) coming from an orbiting satellite.

The larger the mirrors or lenses, the more light the telescope can gather. Light is then concentrated by the shape of the optics. That light is what is seen when one looks into the telescope.

The optics of a telescope must be almost perfect. That means the mirrors and lenses have to be just the right shape to concentrate the light. They cannot have any spots, scratches or other flaws. If they do have such deficiencies, the image gets warped or blurry. It is hard to make a perfect mirror, but it is even harder to make a perfect lens.

Two types of telescopes exist: refracting telescopes and reflecting telescopes. Refracting telescopes use lenses to magnify the image of a faraway object and are also known as beam expanders (Nussbaum, 2005).

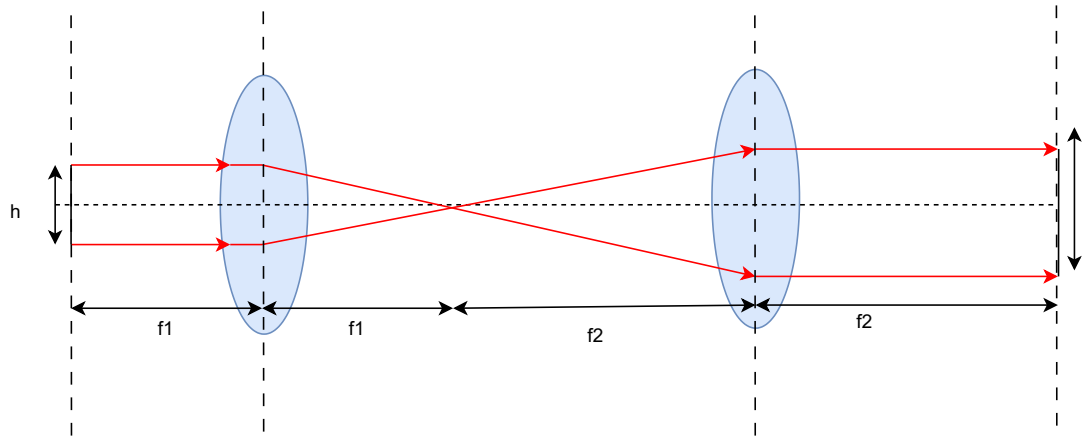

Figure 2.1: Optical relay

Simple beam expanders generally consist of two lenses. The first lens should have a diameter larger than the maximum expected input diameter of the incoming light source as seen in Figure 2.1.

The magnification, M, of a 2-lens system is equal to the ratio of the focal lengths, f, of the lenses, which is also equal to the ratio of the radii of curvatures, r, of the lenses (Kamp, 2007):

$$M = \frac{f_2}{f_1} = \frac{r_2}{r_1} \tag{2.1}$$

The spacing, t, between the two lenses will be equal to the sum of the focal length of the lenses:

$$t = f_1 + f_2 \tag{2.2}$$

where f_1 and f_2 are the focal lenses of the first and second lens, respectively.

A beam expander can be used in reverse, with the larger diameter lens as the input and the smaller diameter lens as the output, to reduce the diameter of the input beam.

Reflecting telescopes use mirrors instead of lenses. Unlike a lens, a mirror can be very thin. A larger mirror does not mean it has to be thicker. Light is concentrated by bouncing off the mirror. It is simpler to make a large, near-perfect mirror than to make a large, near-perfect lens. Also, since mirrors are one-sided, the cleaning and polishing is easier for mirrors than lenses.

Note that, using mirrors will result in flipping the image. Think about the mirror image of letters when one tries to read the reflection of a message on a note. Thus, another mirror has to be placed to flip the image back [1].

Combining the objective lens or primary mirror with the eyepiece results in a telescope. The idea is to collect a maximum amount of light to form a bright image inside the telescope, then use a magnifying glass to enlarge the bright image so it occupies more space on the image plane in a more efficient way.

A telescope has two general properties:

- The quality of collecting the light.
- The quality of magnifying the image.

[1] https://spaceplace.nasa.gov/telescopes/en,retrieved on 05-06-2023

A telescope's ability to collect light is directly related to the diameter of the lens or mirror, also known as the aperture. Generally, the larger the aperture, the more light the telescope collects and brings to focus, and the brighter the final image.

The telescope's magnification, which is its ability to enlarge an image, depends on the combination of lenses used. The eyepiece performs the magnification. Since any magnification can be achieved by almost any telescope by using different eyepieces, the aperture is a more important feature than magnification (Young, 2003).

2.2 Free space optical communication

Free space optical communication (FSOC) is the wireless transmission of data through a modulated optical beam directed through free space, without the use optical systems to guide the light. The fundamental idea goes back to ancient times, as light (or smoke) signals were used to transmit information.

During the 1970s and 1980s, the main proposed application of FSOC systems was to secure a long-distance communication, mainly targeted for ground–satellite or satellite–satellite communication. This focus changed significantly over the last decade, as a new market for FSOC grew in the establishment of high-bandwidth data links and the corresponding integration over a locally restricted area. This makes FSOC a highly attractive candidate for the "last-mile" distribution of high-bandwidth ethernet to the individual homes. Even so, FSOC's application to enable the downlink and uplink between the Earth ground stations and geostationary (GEO) satellites is being studied (Chen, 2022).

The main competitors in this market are the fibre-based optical network, the radio-frequency communication system, as well as the low bandwidth copper cable-based system. In comparison to the closely related wireless radio-frequency transmission, the higher frequency of the optical carrier allows for much higher transmission rates, comparable to those of typical fibre optic networks (Guenther and Steel, 2018). However, FSOC is influenced by atmospheric effects, which limit the sensitivity and achievable data rates. Some of these degradations are turbulence, absorption, and scattering (Majumdar, 2019).

A block diagram showing the general parts necessary for a FSOC system is shown in Figure 2.2. The source generates the information that has to be communicated over the optical wireless system. The modulator, using different techniques, manages the data for transmission. The optical light source can be of two types: Light Emitting Diode (LED) or Laser Diode (LD). A laser is preferred because of the high pointing accuracy and coherence that its beam exhibits. The transmitter and receiver are configured to deliver and receive optical signals propagating in free space. Furthermore, the transmitter converts the incoming electrical signal from the driver circuit into optical form to be transmitted over the atmospheric channel. The atmospheric channel through which the optical beam passes throws many challenges for the transmitted signal. Thus, the signal has to be properly modulated before transmission. Finally, the receiver side contains a photo detector, which converts the received optical signal to electrical form (Sawhil et al., 2018).

2.3 Adaptive optics

Adaptive Optics (AO) is a technique that enables to remove the atmospheric disturbances and allows a telescope to achieve diffraction-limited imaging from the ground. This is crucial to achieve the maximum Signal-to-Noise (SNR) ratio when receiving information by optical communications. The basic idea of AO is to measure first the amount of atmospheric dis-

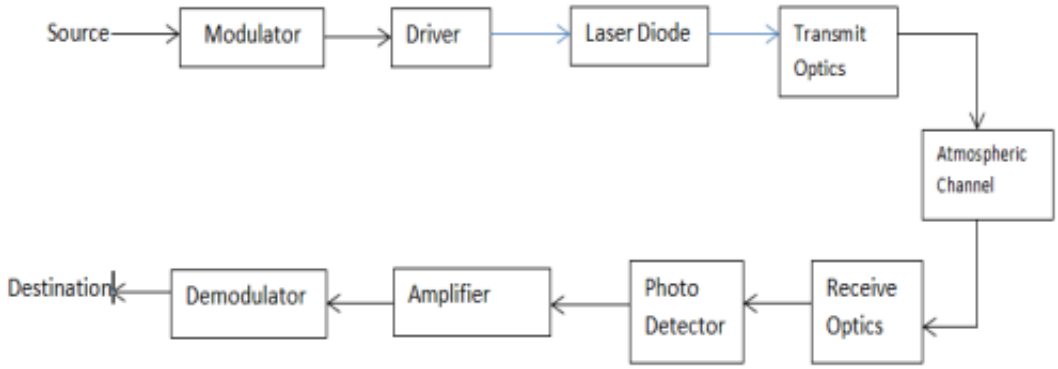

Figure 2.2: Block diagram for a general FSOC system (Sawhil et al., 2018).

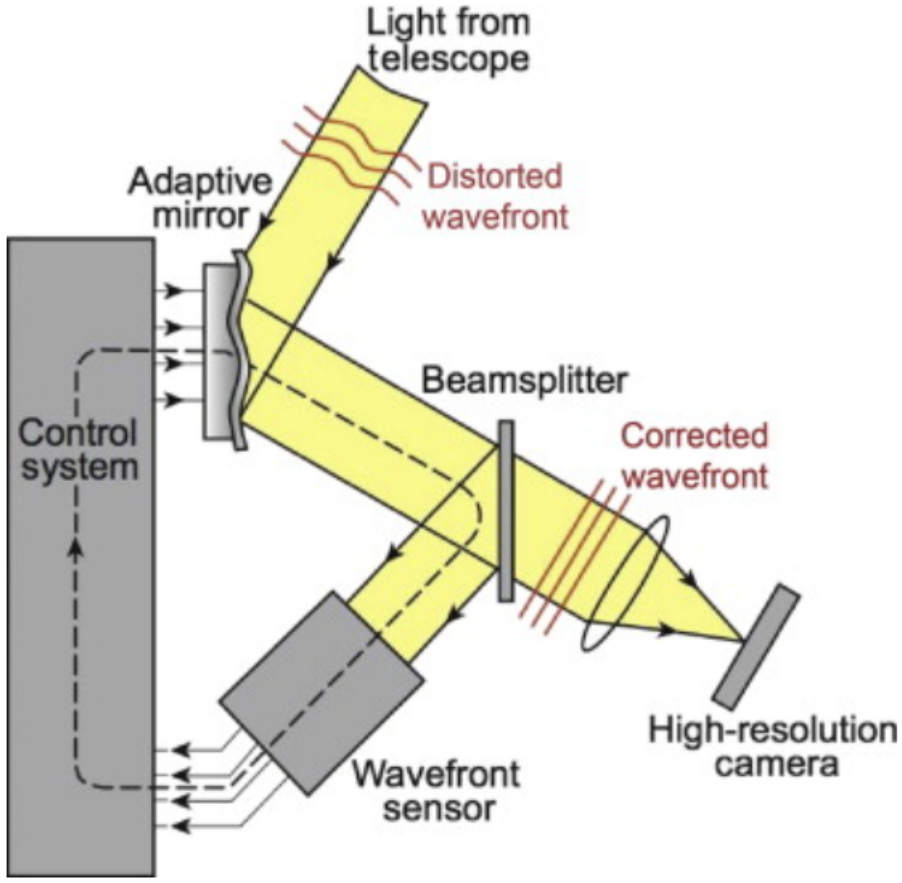

Figure 2.3: A diagram of an AO system (Spohn et al., 2014).

turbance present, and then correct for it before the light reaches the camera or fibre-optics. The main diagram of an AO system is presented in Figure 2.3.

The system consists of three main components: a wavefront sensor, a deformable mirror and a controller. The controller will be further discussed in Chapter 7.

The Wavefront Sensor (WFS) is used in adaptive optics to detect the atmospheric distortions, which feeds back to the Deformable Mirror (DM) to compensate for these distortions.

The most commonly used wavefront sensor in astronomical imaging is the Shack–Hartmann sensor, which is constructed using a lenslet array placed in the aperture plane of the telescope to locally measure the distortions of incident wavefront. This results in a multiple of the image equal to the number of lenslets used. In most AO applications, there is a special point source to be imaged that provides a known signal to the wavefront sensor to measure the distortions. Recently, AO solar observations, LGS or near-to-ground observations have emphasised the need for a wavefront measurement operating on extended sources. Another component that could be used as a WFS is a plenoptics camara. It consists of a plenoptic camera as wavefront sensor that provides a set of measures every millisecond. The plenoptics camera consists of a lenslet array placed in the focal plane of the telescope. Each lenslet re-images the aperture and forms a low-resolution image of the aperture. This means that the plenoptics camera will output a number of images equal to the number of lenslets squared, allowing for better precision when the source is observed.

The wavefront corrector system or DM, is one of the main elements in any AO instrument. These are continuous-surface mirrors with a mechanical means of deformation to match the desired conjugate wavefront. The devices that perform the deformation, called the actuators, can be continuous or discrete. Discrete actuator DMs with stacked piezoelectric actuators were developed in the late 1970s to address the large stroke requirements of infrared systems. Requirements for atmospheric turbulence compensation push the technology of DMs. Hundreds of actuators must be close together. Miniaturisation of actuators to several micrometers, low operating voltages, position accuracy, and low hysteresis become important parameters. The dynamics of an actuator in a DM force train is complicated by the linkage between the actuator and the optical surface. Mechanical, chemical (glues), and electromagnetic connections are commonly used. The structure and damping within the mechanical structure can contribute to hysteresis. Active control of hysteresis has been proposed, but low-hysteresis actuators reduce the complexity of the control system, and increase the closed-loop bandwidth (Tyson and Frazier, 2022).

Some parameters need to be taken into account to verify the suitability of a certain DM model to perform properly within the AO system and its specifications: the number of actuators, the total actuator stroke and the absolute inter-actuator stroke (Rey, 2019):

- The highest possible spatial frequency at which the DM is able to produce useful corrections depends on the number of actuators across the DM optical aperture.
- The maximum turbulent conditions to operate the DM without reaching saturation is directly sustained by the total stroke, which indicates the maximum deformation the DM can suffer.
- The absolute inter-actuator stroke indicates the maximum displacement between two adjacent actuators, which is required to correct for a certain level of turbulence. The higher the turbulence, the more likely it is that two adjacent actuators will have to be pushed away from each other. Note that the inter-actuator stroke is of the order of micrometers.

In short, a DM is composed of a thin membrane with many actuators underneath, which can be controlled individually as depicted later in Figure 4.3. By adjusting the actuator stroke, the deformable mirror corrects for the incoming atmospheric aberrations measured by the wavefront sensor.

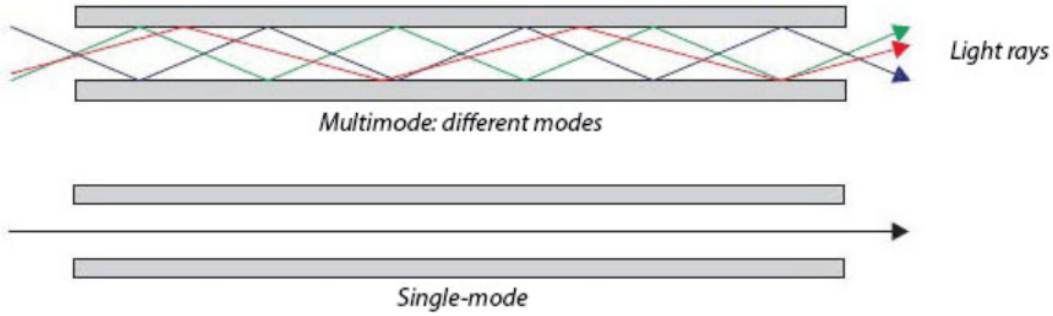

Figure 2.4: Modes passing through SMF vs MMF [2].

2.4 Optical fibre coupling system

Optical-fibre communication systems involve generation, guiding and control of incoming light (Uddin and Chan, 2011). These systems are widely used in the technological society, such as within smartphones and to allow fast internet connection. Despite high transparency, optical fibres have losses and amplification is needed about every 50–100 km. This is achieved by amplifiers (Bunzli, 2016).

There are two types of fibres. The first one is a Single-Mode fibre (SMF), which has a narrow core that allows only a single wavelength of light, also known as single mode of light, to propagate within the core. This means there is no interference or overlap between the different wavelengths of light to influence the data over long distances. The second one is Multimode-fibre (MMF), which has a wide core and allows multiple modes of light to propagate. This means that more types of data can be transmitted. With only a single wavelength of light passing through its core, SMF realigns the light toward the core centre instead of simply bouncing it off the edge of the core as an MMF does. This has been depicted in Figure 2.4. When light propagates through the fibre, light is transmitted within the core in both cases. The cladding keeps the light waves within the core, because the refractive index of the cladding material is less than that of the core.

There are three types of fibres, which are depicted in Figure 2.5. Both SMF and MMF are 125 μm in outside diameter. Single mode has a core size between 8 and 10 μm. Moreover, SMF will support distances up to several thousand kilometers, taking into consideration appropriate amplification, dispersion compensation, and tuning of the heat and light signal where the HW and SW are concerned. This mode requires more expensive light sources, typically operating at a wavelength of 1310 or 1550 nm. Multimode has a core size between 62.5 μm optical multimode 1 and 50 μm optical multimode 2. The wider core allows for the use of incoherent light sources employing many rays, or modes. MMF is conventionally more cost-effective than SMF and operates at a wavelength of 850 or 1310 nm. There is also an optical multimode 3 MMF with a core size of 50 μm. This cable is aqua rather than the traditional orange, and is designed to achieve 10 Gbps at 300 m. Note that, SMF cannot be connected to multimode hardware, and vice versa. At a minimum, this could lead to a 20-dB loss, or 99% of the power. In the worst case, it could burn the equipment out and render it useless (Collins, 2013).

[2] https://www.blackbox.co.uk/gb-gb/page/28533/Resources/Technical-Resources/Black-Box-Explains/Fibre-Optic-Cable/Multimode-vs-Singlemode-Fibre, retrieved on 13-06-2023

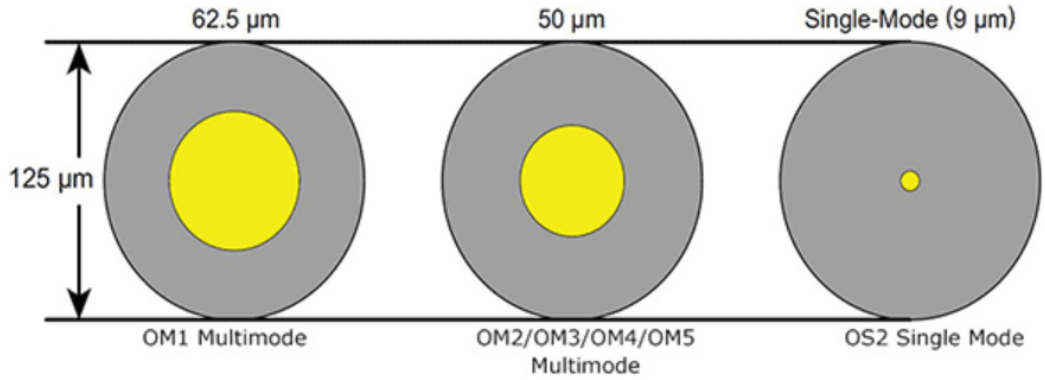

Figure 2.5: Types of optical fibres [2].

2.5 Quantum optics communication

The quantum internet is set to deliver a profound impact across a range of technological frontiers, including quantum communications, computation, and metrology. The working infrastructure to this is a globally interconnected network of quantum information processors, which delivers enhanced capabilities over the use of purely classical information. Attaining such a connectivity over global scale requires the maturity of both ground and satellite nodes that allows efficient distribution and routing of quantum entanglement across the network, and teleportation of quantum states between nodes (Sidhu et al., 2021).

Quantum computation has the potential to solve problems in simulation and optimisation. However, these new computational capabilities also threaten the security of near-ubiquitous public key cryptosystems, such as the Rivest-Shamir-Adleman (RSA) protocol or Elliptic Curve Cryptography (ECC) that underlie much of the internet infrastructure. Progress along this endeavour has primarily proceeded along two distinct routes. First is Post-Quantum-Cryptography (PQC), which replaces RSA with alternative classical cryptosystems that are robust to factorisation and quantum algorithms. However, PQC schemes provide a partial solution since they are not information-theoretically secure. A second more promising candidate for quantum-safe encryption is Quantum Key Distribution (QKD), which guarantees the privacy, authentication, and confidentiality of secure communications. QKD systems are operationally different to classical encryption systems. They take advantage of fundamental properties in quantum mechanics, such as the uncertainty principle or the monogamy of entanglement to safeguard against adversaries with access to arbitrary computational power (Shen et al., 2019; Pirandola, 2021).

2.6 Science case

The aim of the thesis is to design the control system for the adaptive optics system of the TOGS. TOGS is a telescope that will be developed by the IAC, and is intended to be used for quantum key distribution in a number of events. AO will be used to compensate for the effects of the atmospheric turbulence to improve the efficiency of the signal coupling to a Single-Mode fibre. The use of AO as an important part of the ground station is justified by the improvement expected in the coupling efficiency to SMFs. The amount of power delivered to the fibre, provided its extremely small diameter, can be improved by orders of magnitude by the use of AO to compensate the effects of the atmospheric turbulence, without paying

Table 2.1: The use of TOGS for several events (Negrin et al., 2022).

Scenario	*Inter-urban*	*Inter-island*	*LEO-to-Ground*	*GEO-to-Ground*	*Ground-to-Sea*	*Ground-to-Aricraft*
Telescope diameter	355 mm (Meade LX2000) for 2 km	700 mm (Ritchey Chretien) for 2 km	700 mm	1800 mm	700 mm	600 mm
Telescope elevation	-5°	-5°	no negative elevation needed, only movement	no negative elevation nor movement needed	-20°	no negative elevation needed, only movement
Indoor/outdoor	Indoor or outdoor	Outdoor	Outdoor	Outdoor	Outdoor	Outdoor
Type of location	Rooftop in city buidings	Rooftop in city buidings	Rooftop in city buidings	Rooftop in city buidings (weight problem)	Rooftop in city buidings	Rooftop in city buidings

any penalty in the increase of dark counts. This would be derived by the use of thicker fibres or free-space coupling to larger detectors (Negrin et al., 2022).

TOGS Scenarios

TOGS is considered to be used for different events. These events include:

1. Inter-urban link, *e.g.*, two buildings.
2. Inter-island link, *e.g.*, between Tenerife and La Palma.
3. LEO-to-ground. In this case, the ground station needs to track the LEO satellite.
4. GEO-to-ground links.
5. Ground-to-sea link.
6. Ground-to-aircraft.

According to its use, the telescope will have different properties. The properties corresponding to each of the scenarios are listed in Table 2.1. This thesis will mostly focus on the use of inter-island communication. None of the options require automatic pointing.

TOGS product breakdown

The TOGS consists of several parts, which are explained by Negrin et al. (2022) and will be discussed below. In QKD, one party (say Alice) prepares a quantum state and sends the prepared quantum state to another party (say Bob), who will measure it. The TOGS is divided in three components: Alice (sender quantum key), Bob (receive quantum key), and shared parts (parts shared between Alice and Bob). TOGS could behave like Alice or like Bob according to the scenario, where Alice is the transmitting party and Bob is the receiving one.

Beacon tracking will be used to locate the ground or satellite station depending on the scenario. To do this, a classical free-space optical beam will be used as it allows to transmit a data link and clock synchronisation between Alice and Bob. This beacon laser signal will have enough beam divergence to allow the receiver to be illuminated despite of the pointing uncertainty.

In case of inter-urban or inter-island communication, the pointing for course tracking will be performed manually. The fine tracking, however, will be carried out using Fine a Steering Mirror (FSM) controller closed-loop algorithm.

The general schematics of the TOGS is depicted in Figure 2.6. Since the thesis will focus on the adaptive optics system of the receiving party (Bob), this system will be explained in detail. The receiver has a randomising beam splitter, which sets the measurement basis, and the polarising beam splitters measuring the bit value. A click in one of the photon-counting detectors sets the bit value and the measurement basis angle. An AO unit will be used in the TOGS side to compensate the high-order wavefront aberrations. The AO unit will be designed to be directly mounted on the telescope and will deliver the fibre-coupled quantum signal as its output interface.

Bob's adaptive optics system

Using AO for free-space propagation stabilises the optical signal on a detector, and maximises the received signal by returning near-diffraction limited performance to the optical system and stabilising the channel transmission and noise. It consists of a plenoptic camera as wavefront sensor that provides a set of measures every millisecond. Moreover, a DM will be used as the correction element for the AO, due to the high level of aberrations expected. Finally, a separated tip-tilt control will be used using the FSM mirror. This mirror will have a much higher dynamic range and speed in comparison with the DM and will be more suitable for this task. The DM will use 12x12 actuators, and the FSM mirror can be considered to have two actuators, one per axis.

Bob's quantum receiver

The receiver for quantum signals shall accept polarisation encoded quantum communications compatible with the BB84 protocol. This protocol requires polarisation measurements in horizontal and vertical basis, and diagonal and anti-diagonal basis. The selection of the basis for each incoming photon will be randomly selected. The detection will be based on Superconducting Nanowire Single-Photon Detectors (SNSPDs) that provide a high detection efficiency in 1550 nm to operate in daylight and low dark noise. Connected to it, a timestamp unit is retrieved to label each event.

The use of Avalanche Photon Detectors (APDs) as receivers is considered for the quantum channel in some scenarios, like the inter-urban or LEO-to-ground, provided they could enable a reasonable performance at a fraction of the cost. However, using SNSPDs will simplify the design and development of the TOGS. Moreover, a high efficiency, low dark current, and very small jitter will also be obtained.

2.7 Requirements

After defining the main research question along with the sub-questions and the objectives in Chapter 1, and performing the mission heritage, several requirements are retrieved for the TOGS. These are stated in Table 2.2. The functional requirements are indicated with the acronym FR, performance requirements with PR, the design requirements with DR, and the software requirements with SW. The driving requirements are stated by **TOGS-PR-04** and **TOGS-PR-07**, which are used to observe the performance of the entire AO system.

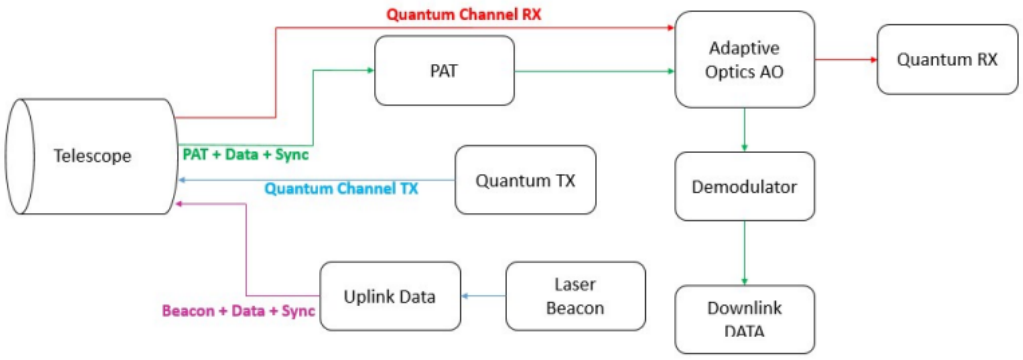

Figure 2.6: Schematics of the TOGS for quantum communications (Negrin et al., 2022).

Table 2.2: The requirements defined for the TOGS (Negrin et al., 2022).

ID	Requirement
TOGS-FR-01	The TOGS shall incorporate hardware and software to behave as the source of the quantum communications and as the receiver of them.
TOGS-FR-02	The TOGS shall be transportable using commercially available transport systems.
TOGS-PR-01	The TOGS shall be able to provide its full functionality during the daytime.
TOGS-PR-02	The fine pointing accuracy shall be better than 10 micro-radian (2 arc-seconds) for data acquisition.
TOGS-PR-03	The course pointing accuracy shall enable direct line of sight (carried out manually).
TOGS-PR-04	TOGS shall use AO to compensate for the aberrations caused by the atmospheric turbulence with a Strehl of 40%.
TOGS-PR-05	The AO system shall compensate aberrations with a Fried parameter between 3 cm and 20 cm [TBC]
TOGS-PR-06	The AO system shall compensate aberrations present at a wind speed between 0 m/s and 15 m/s
TOGS-PR-07	The Single-Mode fibre shall deliver a least a coupling of 40%.
TOGS-DR-01	TOGS shall operate the quantum link at 1550 nm when the solar light intensity is 5x weaker than 850 nm, and the Rayleigh scattering is only 7% of its value at 850 nm.
TOGS-DR-02	The design shall include a Nasmyth focus to keep the movement of the AO system in just the gravity invariant azimuth axis and to allow for stable integration and operation for the AO.
TOGS-DR-03	The AO system shall deliver the quantum signal at its output interface through a Single-Mode Fibre.
TOGS-DR-04	The maximum control loop frequency shall be 1000 Hz.
TOGS-DR-05	The DM shall use 144 actuators (12x12).
TOGS-DR-06	The system shall have a maximum delay of 2 samples.
TOGS-DR-07	The telescope shall have a diameter of 700 mm.
TOGS-SW-01	The software platform shall be Matlab.
TOGS-SW-02	The toolbox used to represent the AO system in the most realistic way shall be OOMAO.
TOGS-SW-03	The AO system shall not be modelled using equation of motions.
TOGS-SW-04	The AO system shall be modelled as a discretised system.

CHAPTER

3 Physical environment

The environment of the telescope will influence the accuracy of the adaptive optics caused by perturbations. Here, the type of aberrations encountered will be addressed upon in Section 3.1, followed by the environmental perturbations that cause these aberrations in Section 3.2.

3.1 Types of aberrations

Ideally, an optical system will produce a unique image point for each object point. Any departures from this ideal theory of Gaussian theory, also known as paraxial or first-order optics, are known as aberrations and can be categorised into two main types: monochromatic single colour aberrations and chromatic (varying wavelengths) aberrations. When aberrations occur, the peak intensity will be reduced and the image or laser beam propagating to an object will appear to be blurred. Seven primary types of aberrations will be considered, five of monochromatic and two of chromatic variety.

Deformable mirrors are theoretically capable of removing all types of monochromatic aberrations from a wavefront to allow for the formation of an ideal, diffraction-limited image (Kamp, 2007; Tyson and Frazier, 2022).

Monochromatic aberrations

There are five primary monochromatic aberrations, which can be further divided into two subgroups: the ones deteriorating the image and the ones deforming the image. These aberrations are a direct result of departures from first-order theory, which states $\sin(\theta) \approx \theta$, meaning it assumes that the light rays make small angles with the principal axis. As soon as one wants to consider light rays incident on the periphery of a lens, the statement $\sin(\theta) \approx \theta$, is no longer satisfactory and one must consider more terms in the expansion:

$$\sin(\theta) \approx \theta - \frac{\theta^3}{3!} + \frac{\theta^5}{5!} + \frac{\theta^7}{7!} + ... \tag{3.1}$$

First the types of monochromatic aberration causing image deterioration, including spherical aberrations, coma and astigmatism will be explained. Then, the two types causing image deformations will be described, referring to field curvature and distortion.

Spherical aberration

For parallel incoming light rays, an ideal lens should focus the rays to a single point on the optical axis, as seen in Figure 3.1(a). This will result in the image of a point source that is

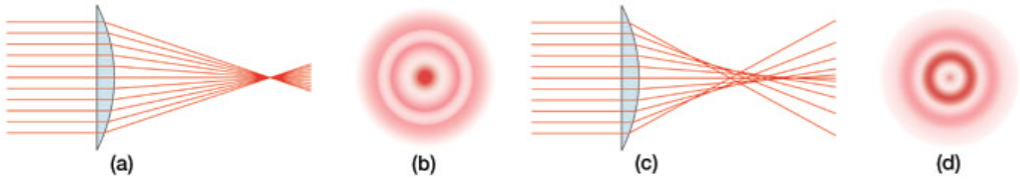

Figure 3.1: Comparison of an ideal situation to one where spherical aberration occurs [3].

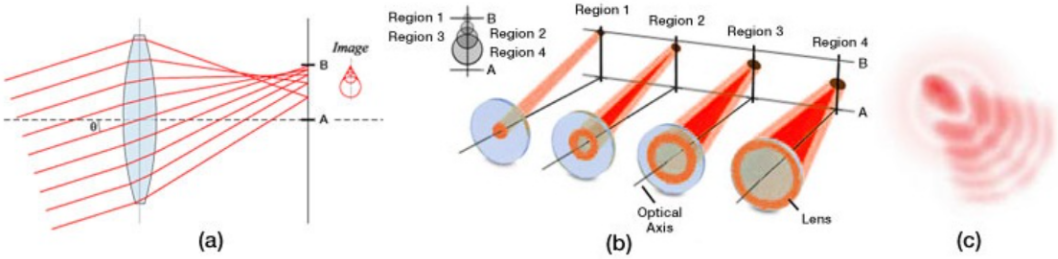

Figure 3.2: The effects of positive coma [3].

located on the optical axis to be a bright circular disk surrounded by faint rings, as seen in Figure 3.1(b), also known as the Airy diffraction pattern. This effect is always present when light passes through an aperture. Nevertheless, in reality, the light rays that reach a spherical converging lens far from the principal axis will be focused to a point that is closer to the lens than those light rays that reach the spherical lens near the principal axis, as shown in Figure 3.1(c). Subsequently, there is no single focus for a spherical lens, and the image will appear to be blurred. Thus, instead of having an Airy diffraction pattern, where almost all the light is enclosed in a central bright circular spot, spherical aberration will cause the light to be distributed from the central disk to the surrounding rings, as depicted in Figure 3.1(d). Whenever spherical aberration is present, the best focus for an uncorrected lens will be somewhere between the focal planes of the peripheral and axial rays. Note that spherical aberration only pertains to object points that are located on the optical axis.

Coma

Coma is an image-degrading aberration associated with object points that are only slightly off-axis. When an off-axis bundle of light is incident on a lens, the light will undergo different amounts of refraction depending on where it hits the lens, as shown in Figure 3.2(a). As a result, each annulus of light will focus onto the image plane at a slightly different height and with a different spot size, as shown in Figure 3.2(b), which leads to different transverse magnifications. The central region of the lens forms a point image at the vertex of the cone, while larger rings correspond to larger comatic circles that are displaced farther from the principal axis. This leads to the image of a point source depicted in Figure 3.2(c), being a complicated asymmetrical diffraction pattern with a bright central core and a triangular flare that departs drastically from the classical Airy pattern shown in Figure 3.1(b) above. The elongated comet-like structure form can extend either towards or away from the optical axis depending on whether the comatic aberration is negative or positive, respectively.

[3] https://www.thorlabs.com/newgrouppage9.cfm?objectgroup_ID=3258, retrieved on 25-01-2023

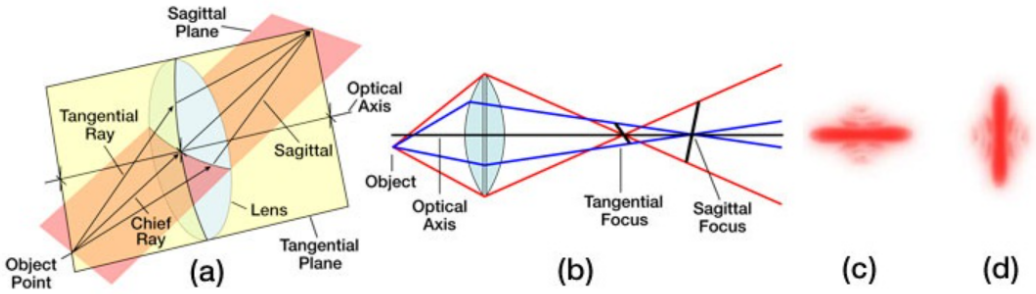

Figure 3.3: The effects of astigmatism [3].

Astigmatism

Astigmatism, like coma, is an aberration that occurs when an object point is moved away from the optical axis. Under such conditions, the incident cone of light will reach the lens obliquely, leading to a refracted wavefront characterised by two principal curvatures that ultimately determine two different focal image points. Figure 3.3(a) depicts the two planes to be considered: the tangential plane and the sagittal plane. The tangential plane is defined by the chief ray, which is the light ray from the object that passes through the centre of the lens, and the optical axis. The sagittal plane is a plane that contains the chief ray, and is perpendicular to the tangential plane.

In addition to the chief light ray, Figure 3.3(a) also shows two other off-axis light rays, one passing through the tangential plane and the other passing through the sagittal plane.

Consequently, in general, the focal lengths associated with these planes will be different as shown in Figure 3.3(b). If the sagittal focus and the tangential focus coincide, then the object point is on axis and the lens does not cause astigmatism. However, as the amount of astigmatism increases, the distance between these two foci will also increase, resulting in the image losing definition around its edges. The presence of astigmatism will cause the ideal circular point image to be blurred into a complicated elongated diffraction pattern as seen in Figure 3.3(c) viewed from the tangential focal plane and Figure 3.3(d) viewed from the sagittal focal plane.

Field curvature

For most optical systems, the final image must be formed on a planar surface. However, in reality, a lens that is free of all other off-axis aberrations creates an image on a curved surface known as a Petzval surface. The nominal curvature of this surface, which is known as the Petzval curvature, is the equivalent of the lens radius. For a positive lens, this surface curves inward towards the object plane, whereas for a negative lens, the surface curves away from that plane. The field curvature aberration arises from forcing a naturally curved image surface into a flat one. For the image, the presence of field curvature makes it impossible to have both the edges and central region of the image be crisp simultaneously. If the focal plate is shifted to the vertex of the Petzval surface, denoted as Position A in Figure 3.4(a), the central part of the image will be in focus while the outer portion of the image will be blurred, making it impossible to distinguish minor structural details in this outer region as seen in Figure 3.4(b). Alternatively, if the image plane is moved to the edges of the Petzval surface, equal to position B in Figure 3.4(a), the opposite effect occurs; the edges of the image will come into focus, but the central region will become blurred. The best compromise between

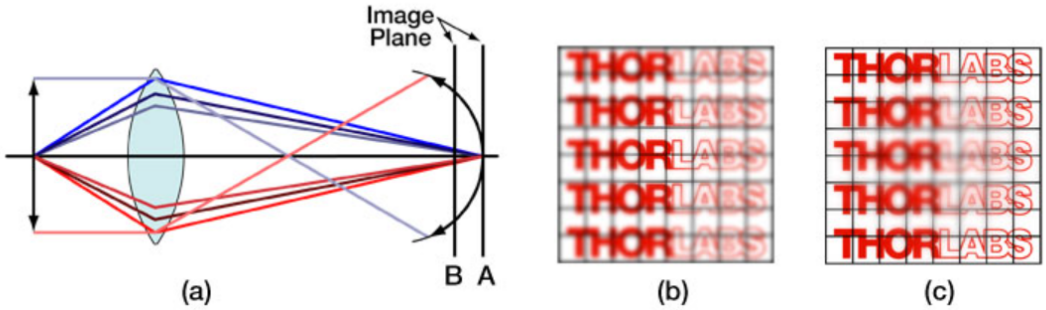

Figure 3.4: The effect of field curvature [3].

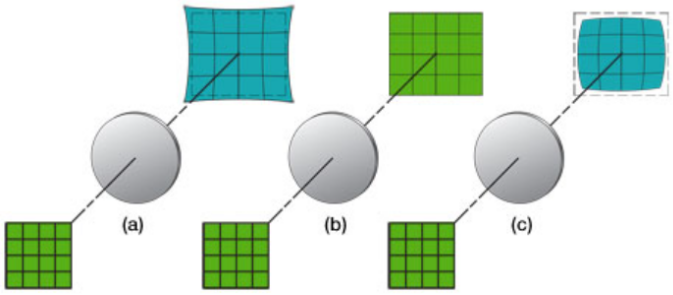

Figure 3.5: The effect of positive (pincushion) and negative (barrel) distortion [3].

these two extremes is to place the image plane somewhere in between the vertex and edges of the Petzval surface. However, regardless of its location, the image will never appear sharp over the entire field of view as seen in Figure 3.4(c).

Distortions

The last type of the monochromatic aberrations is distortion. This is easily recognised in the absence of all other monochromatic aberrations, because it deforms the entire image even though each point is sharply focused. Distortion arises because different areas of the lens usually have different focal lengths and magnifications. If no distortion is present in a lens system, the image will be a true magnified reproduction of the object, Figure 3.5(b). However, when distortion is present, off-axis points are imaged either at a distance greater than normal or less than normal, leading to a pincushion (Figure 3.5(a)) or barrel shape (Figure 3.5(c)), respectively. Positive or pincushion distortion occurs when the transverse magnification of a lens increases with the axial distance. This effect causes each image point to be displaced radially outward from the centre, with the most distant points undergoing the largest displacements. On the other hand, negative or barrel distortion occurs when the transverse magnification of a lens decreases with axial distance. In this case, each image point moves radially inward toward the centre. Again, the most distant points undergo the largest displacements.

Chromatic aberrations

The monochromatic aberrations discussed above can all theoretically be compensated for using a deformable mirror. However, when a broadband light source is used, chromatic aberrations will result. Chromatic aberrations arise from the variation of the index of refraction

of a lens with incident wavelength and come in two forms, lateral and longitudinal. Since blue light is refracted more than red light, the lens is not capable of focusing all colours to the same focal point. Therefore, the image size and focal point for each color will be slightly different, leading to an image that is surrounded by a halo. Generally, since the eye is most sensitive to the green part of the spectrum, the tendency is to focus the lens for that region; if the image plane is then moved towards the lens, the periphery of the blurred image will be tinted red. Note that a deformable mirror cannot compensate for these aberrations. However, for optical communications, a point source of only one wavelength is used, meaning no chromatic aberrations are present.

The types of aberrations that will be encountered during the analysis of the AO system performance will be explained with the results in Chapter 8.

3.2 Environmental perturbations

Many environmental perturbations could cause the aberrations explained above in the retrieved images. These perturbations will be discussed in this section. Note that the deformable mirror is not necessarily capable of correcting all these perturbations (Tyson and Frazier, 2022).

Atmospheric turbulence

A quantum signal propagating through the Earth's atmosphere is affected by turbulence and an increase in background noise owing to daylight operation. Both effects directly limit the attainable key and entanglement distribution rates. Specifically, interaction with turbulent eddies in the atmosphere cause rapid fluctuations in the transmission efficiency of a communication link. This leads to a stochastic broadening of the beam waist and wandering of the beam centroid. Generally, the sensitivity of the quantum signal to atmospheric turbulence depends on the type of encoding chosen.

The effect of atmospheric aberrations are represented by the Fried parameter r_0. The lower r_0, the more severe the atmospheric turbulence. Moreover, the atmospheric turbulence may be increased with increasing wind speed. From requirement **TOGS-PR-05** and **TOGS-PR-06**, the system will have to correct for turbulences with a Fried parameter between 3 cm and 20 cm and a wind speed between 0 and 15 m/s, respectively.

Daylight

Daylight operation of QKD leads to increased back-scattering of solar radiation in the atmosphere, which increases the background noise in the signal. The the use of Single-Mode fibre as spatial filtering, allows QKD in daylight, as only the wavelength chosen to communicate with will be detected.

Turbulence and pointing errors

Turbulence will also influence the communication, depending on the timescale. On a fast timescale, the beam waist is broadened due to the interaction with smaller turbulent eddies. This causes the received spot size to increase. On a slow timescale, the beam is deflected due to the interaction with the larger eddies, which causes the random Gaussian wandering of the beam centroid with a certain variance. The dynamics is in the order of 10-100 ms. This means that it can be resolved using a sufficiently fast detector.

Moreover, pointing errors from jitter and imprecise tracking also cause centroid wandering with a slow timescale. For a typical 1μrad error at the transmitter, a variance of $\sigma_{\mathrm{P}}^2 \simeq \left(10^{-6}z\right)^2$ occurs, where z is the distance between the two objects.

Thermal blooming

Atmospheric turbulence occurs whenever an amount of thermal agitation is present, while thermal blooming occurs whenever the atmosphere absorbs enough energy from a beam to alter the local index of refraction. The resultant self-induced distortion is called thermal blooming. In one study, when continuous-wave laser beams were sufficiently developed in the kilowatt range, expansion of the beam size ("blooming") was observed. Both steady-state and transient thermal blooming have been investigated. When the absorbed laser power is balanced by thermal conduction, natural convection, or forced convection due to wind or beam motion, the thermally bloomed beam turns into the wind. For a zero-wind case, thermal blooming occurs, often called thermal defocusing, because the lowest index of refraction occurs near the centre of the beam, where the beam intensity is the highest. This atmospheric negative lens causes the beam to defocus.

An important case occurs when the wind, or an artificial wind caused by beam slewing, causes the beam to take on a characteristic crescent-shaped pattern. Light is refracted more toward the dense portion of the air, the least intense region. Interaction with a compensated high power beam has been a subject of many studies. The combined effects of blooming and turbulence are even more complex and are being investigated with detailed wave optics and fluid models. This effect cannot be corrected for with a DM. Therefore, its effect will be neglected when studying the performance of the new AO system for the TOGS.

Optical Misalignments and Jitter

The presence of tilt or dynamic tilt (jitter) into a system can reduce its performance. In some cases, this performance is only slightly reduced, as in the case of an imaging system where tilt simply moves the position of the image without affecting its quality. These problems often can be accepted. On the other hand, slight misalignments in optics inside a laser resonator can greatly reduce its performance and, in many cases, can eliminate the possibility of lasing altogether. Errors in setting up or mounting or mounting the system as well as external error sources, and thermal problems can all contribute negatively to a poorly performing system.

Adaptive optics in a tilt-correction mode can be used to correct for these errors. The problem of maintaining alignment or beam pointing has evolved from early electromechanical telescope and radar control systems, to the present-day scanning and control systems that operate in the megahertz range. A tilted component in a system can induce other higher-order aberrations. A tilted mirror or beam splitter intercepting a converging beam will introduce the next higher-order aberration, astigmatism. A tilted spherical optical element in a telescope will introduce coma. Severe tilts in complicated optical configurations can introduce many high-order aberrations.

The elimination of tilt, or pointing error, is the first business of adaptive optics. Control of fast tilt (jitter) or slow tilt (drift) is often all that is needed in an adaptive optics system.

Manufacturing and Micro-errors

The manufacturing technology of the optical surfaces limits the overall performance of the optical system. With adaptive optics technology, many of the defects that arise from manufacturing can be corrected. The materials chosen for refractive or reflective optics may have

surface errors that figuring and polishing cannot remove. Generally, they are of such low magnitude or high spatial frequency that adaptive optics is useless. Occasionally, a large systematic error may occur that produces a low-order aberration. A variation in polishing pressure, for instance, may produce such a defect that can be removed with adaptive optics when the optical element is used.

Usually, these static, low-order defects can be calibrated out or compensated for during system setup, without relying on closed-loop control. Even after polishing and coating, there may be roughness on the surface, called microstructure, that would affect an adaptive optics system. The adverse effects of the aberrations are usually less than the increased scattering from the optical surface. Scattered light affects sensors and can result in reduced-control system performance. The microstructure of polished optical materials is expressed in root mean square (rms) roughness. The roughness can range from about 10 Å for fused quartz to over 100 Å for materials such as molybdenum and beryllium. The fraction of incident light scattered, the Total Integrated Scatter (TIS), from a surface with rms roughness, δ, is

$$TIS = \left(\frac{4\pi\delta}{\lambda}\right)^2 \tag{3.2}$$

where λ is the incident light wavelength. For a roughness approaching even small fractions of a wavelength, the negative effects of scattering can be severe. Large roughness values are also known to be extremely sensitive to incident high powers. If light is multiply reflected in the hills and valleys of the surface, absorption and microthermal mapping can lead to stresses that result in permanent damage to a mirror surface.

The environmental conditions that will be corrected for by the DM will be the manufacturing errors given by the manufacturers, optical misalignments, and the dominant atmospheric turbulence that will be simulated in the laboratories as explained later in Chapter 4.

CHAPTER

4 Hardware experimental test set-up

This chapter describes all the hardware components used for the experimental set-up, as well as the set-up configuration. First, the measured source will be described in Section 4.1, followed by how the atmospheric turbulence will be simulated in Section 4.2. Then, the sensor used to measure the aberrations and the controller to correct these aberrations are defined in Section 4.3 and Section 4.4, respectively. Next, the coupling used to retrieve the quality of the AO system's performance is included in Section 4.5. Finally, the entire experimental set-up is explained in Section 4.6.

4.1 Source

To reproduce the light source, Thorlabs LDM635 laser will be used. The ∅1.40" by 5.8" housing contains a laser diode, collimating lens, and automatic power control circuit. Its properties are listed in Table 4.1. For this experiment, the laser will be set to 633 nm.

4.2 Atmospheric turbulence simulator

The atmospheric perturbations will be simulated using a Lexitek Motorised rotary stage together with a stepper controller, which allows precise motion control of stepper motor stages, and is optimised for rotary stages. It is able to control two axes of motion. Its interface consists of a numeric keypad and LCD display, in addition to an RS-232 serial port.

Table 4.1: The properties of Thorlab's LDM 635 laser (Thorlabs, 2020b).

Property	**Value**
Wavelength	635 nm
Wavelength, min/max	625-645 nm
Beam diameter	3.0 mm x 5.0 mm (elliptical)
Power (adjustable)	4.0 mW
Stability, short term drift	0.01 dB
Stability, long term drift	0.1 dB
Operating temperature	10-40 °C
Power supply (±10%)	100-240 VAC, 0.48 A 50-60 Hz Output: 9 VDC @ 2.2 A

Table 4.2: Properties of the Lexitec atmospheric simulator [4].

Property	**Value**
Motorised Rotary Stage	
Dimensions	150 mm x 225 mm x 37.5 mm
Step error	1.5 arcmin
Rotation rate	10 rpm
Cycles per revolution	32-2500
Stepper Motor Controller	
motor control	12.5-25,000 pps (two axis)
Pulse rate	100 kHz
Turbulent phase plate	
Transmission	400-1600 nm
Diameter	100 mm
Phase grid	20 μm
Optical path difference step	0.02 μm
Optical path difference range	5-30 μm

The controller outputs step and direction, and enables Transistor-Transistor-Logic (TTL) signals to a stepper driver. The standard motion profile is a trapezoid with two parameters, the maximum rate and the slope of the ramp up and down.

With this controller, a disk with aberrations, also known as turbulent phase plate, will be moved stepwise, which will cause the light source to be aberrated. For this specific instrument, three phase plates with a Fried parameter of r_0 = 1 mm, r_0 = 2 mm, and r_0 = 3 mm, respectively, are available, which are scaled to the aperture of the WFS. Furthermore, all the properties of the atmospheric simulator are stated in Table 4.2.

4.3 Wavefront sensor

As mentioned previously in Section 2.6, the TOGS will use a plenoptics camera as WFS. Therefore, an attempt was made to initially use a plenoptics camera. However, hardware difficulties occured during the set-up that could not be solved. Therefore, it was decided to use a Shack-Hartmann wavefront sensor instead. Nevertheless, the work performed with the plenoptics camera has been described in Appendix A.

The Thorlabs WFS20-5C will be used as WFS, and its properties are stated in Table 4.3. The lenses to create the micronlens array are formed using photolithographic techniques based on a semiconductor processing technology. This allows for excellent uniformity in the shape and position of each microlens, unlike some microlens arrays produced from molded epoxy. More specifically, the chrome mask blocks light from being transmitted unless it goes through a microlens and, therefore, increases image contrast.

The WFS instruments comprise a Complementary Metal Oxide Semiconductor (CMOS) camera and a microlens array that is mounted at a defined distance in front of the camera sensor chip. Each microlens of the lenslet array collects the light incident to its aperture and generates a single spot on the detector plane that is located at a distance of one focal length behind the lenslets.

[4] https://www.lexitek.com/ls100.html, retrieved on 10-05-2023

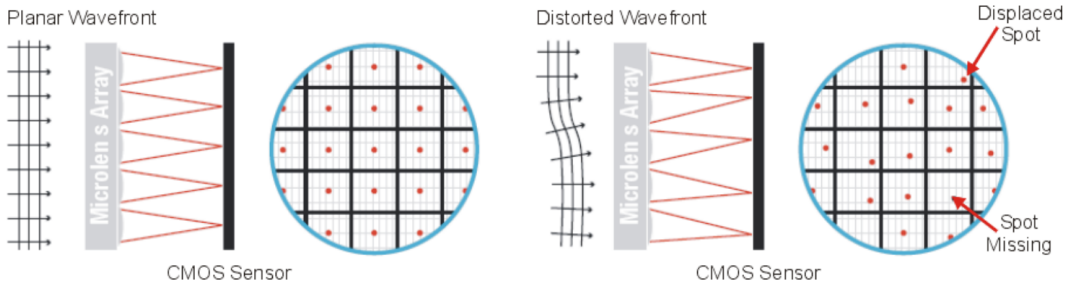

Figure 4.1: Sketch of the CMOS sensor function within the Shack-Hartmann sensor [5].

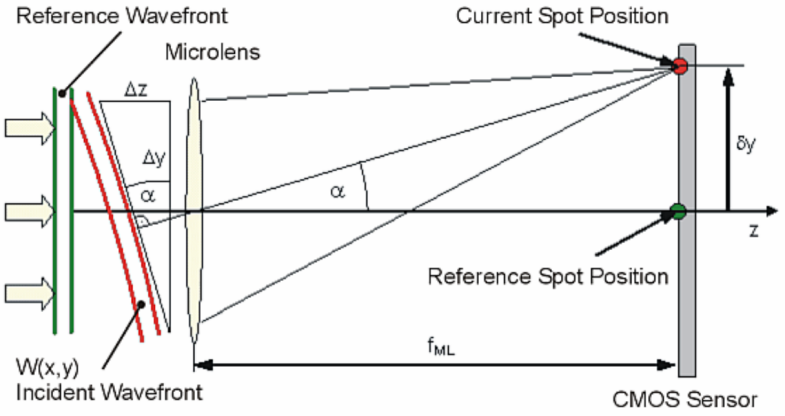

Figure 4.2: Slope reconstruction [5].

Each spot is centred behind the lens that generates it only if the incident wavefront is planar and parallel to the plane of the lenslets. These are the reference spot positions, also known as the reference spotfield.

In case of a distorted wavefront incident on the sensor, the focal spot positions shift along the X and Y directions, away from the optical axis Z of its associated microlens and the predetermined reference spot. The displacement is described by the angle α.

The sketch seen in Figure 4.2 shows that this deviation from the reference spot is caused by the deviation of the wavefront incident angle on the microlens, or in geometrical terms:

$$\tan\alpha = \frac{\Delta z}{\Delta y} = \frac{\delta y}{f_{ML}} \tag{4.1}$$

If $W(x,y)$ describes the shape of the wavefront, then its partial derivatives relative to X and Y are determined by the spot shifts δx and δy, respectively, as well as by the distance between microlens and detector. This is usually equal to the focal length of the microlens f_{ML}:

$$\frac{d}{dx}W(x,y) = \frac{\delta x}{f_{ML}} \quad \frac{d}{dx}W(x,y) = \frac{\delta y}{f_{ML}} \tag{4.2}$$

The spot deviations δx and δy are determined by calculating the centroid coordinates of all detectable spots and, subsequently, subtracting the corresponding reference coordinates. The wavefront shape function $W(x,y)$ is the result of a 2-dimensional integration process of these spot deviations. For example, take the left image of Figure 4.2 to be the reference slopes. The dots are all centred, meaning that the slopes at this point in time are zero. Then, a distortion is introduced as seen in the right image of Figure 4.2. This causes the points to be

Table 4.3: The properties of Thorlab's WFS20-5C Shack-Hartmann sensor [5].

Property	**Value**
Microlens arrays	
Wavelength range	300-1100 nm
Free aperture	∅9 m
Mask or Coating	Chrome mask
Reflectivity	25%
Lenslet pitch	150 μm, square grid
Lens shape	Round, Plano-convex spherical
Lens size	∅146 μm
Number of active lenslets	47 x 35
Focal length (typical, nominal, mounted)	4.1 mm, 5.6 mm, 5.2 mm
Array size	10 mm x 10 mm x 1.2 mm
Substrate material	Fused Silica (Quartz)
Camera	
Sensor type	CMOS
Resolution	1048 pixels x 1080 pixels
Sensor size	7.20 mm x 5.40 mm
Pixel size	5.0 μm x 5.0 μm
Shutter	Global (exposes entire sensor at once)
Exposure range	0.004 - 83.3 ms
Image digitisation	8 bit
Wavefront measurement	
Accuracy (at 633 nm)	λ/30 rms
Sensitivity (at 633 nm)	λ/100 rms
Dynamic range (at 633 nm)	>100λ
Slope	± 1.0°
Local curvature	>7.4 mm

moved. The slopes then become the displacement of those points with respect to the centre in the y-direction, divided by the displacement in the x-direction.

4.4 Deformable mirror

Here, the Boston Micromachines Multi-3.5-DM Deformable Mirror will be used. Boston Micromachines DMs consist of a mirror membrane supported by an underlying actuator array. Each actuator can be individually deflected by electrostatic actuation to achieve the desired pattern of deformation. They feature large strokes, high dynamic motion and a great optical quality for fast and accurate wavefront correction. More specifically, an actuator array is built upon a Cartesian layout of electrodes. The supported mirror facesheet moves without strong inter-actuator coupling, enabling a better control.

[5] https://www.thorlabs.com/newgrouppage9.cfm?objectgroup_id=5287&pn=WFS20-5C, retrieved on 12-05-2023

[6] https://bostonmicromachines.com/products/deformable-mirrors/standard-deformable-mirrors/, retrieved on 14-04-2023

[7] https://www.thorlabs.com/newgrouppage9.cfm?objectgroup_id=3258, retrieved on 14-04-2023

Table 4.4: The properties of Boston's deformable mirror [6].

Property	**Value**
Mirror	
Active actuator array size	12 x 12
Active aperture size	4.4 mm x 4.4 mm
Number of available actuators	140
Stroke	3500 nm
Interactuator coupling	13%
Actuator pitch	400 μm
Av. stepsize	<1 nm
Hysteresis	None
Fill factor	>99%
Acceptance angle	±15°
Mechanical response time	<75 μs (13.3kHz)
Surface quality	<30 nm (RMS)
Max. operating voltage	236 V
Window	
Window coating	400-1100 nm AR Coating
Window mount	6° Wedge
Electronic controller	
Control type	Multi driver
Frame rate	2 kHz
Resolution	14 bit
Dimensions	229 mm x 178 mm x 64 mm

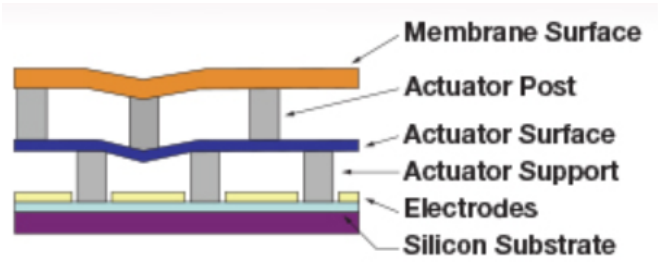

Figure 4.3: Boston Micromachine MEMS DM [7].

4.5 Fibre optics

To study the performance of the controller placed in a closed loop, a fibre coupling will be used that collects the light after the aberrations are corrected for and compares it to the case where no aberrations are present.

However, before the light can be retrieved through the fibre optics, the maximum amount of light that can be collected before the fibre-optics coupling, has to be measured. This is done using a polarimeter manufactured by Thorlabs called PAX1000IR1. Its properties are stated in Table 4.5. The polarimeter is placed after the beam splitter, in front of the fibre optics as shown in Figure 4.4(a). Then, the polarimeter is coupled to the laptop to open the software and read the information, such as the wavelength of the source and the direction of

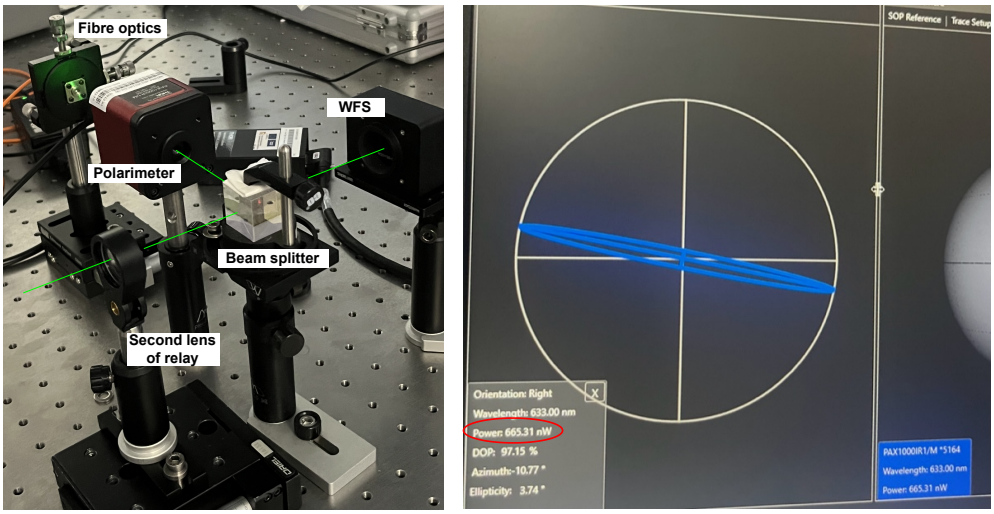

(a) Experimental set-up with the polarimeter. (b) Max. light retrieval with polarimeter SW.

Figure 4.4: Retrieving the maximum amount of light received.

Table 4.5: Properties of Thorlabs' polarimeter PAX1000IR1 [8].

Propery	**Value**
Wavelength range	600-1080 nm
Dynamic Range	-60 to +10 dB
Sampling Rate	30 (default) 400 samples/s (maximum)
Azimuth Accuracy	±0.25°
Ellipticity Accuracy	±0.25°
DOP Accuracy	±1.0%
Free Space Aperture	∅3 mm
Maximum Input Beam Divergence	2°
Warm-Up Time for Rated Accuracy	15 min

the source, denoted by the azimuth angle. The screen is shown in Figure 4.4(b). As seen, the maximum amount of light retrieved , denoted by the power, is **665.31 nW**.

After the maximum amount of light is determined, a 52.5/125 multi-mode fibre coupling will be used as fibre optics coupling,as explained in Chapter 2. The MMF is coupled to an optical power and energy meter console provided by Thorlabs called PM400, and its properties are stated in Table 4.6. Here, the f50 lens is placed in front of the MMF to converge the light to one point. The MMF is then placed in the focal point were the light converges the most. With the PM400, the amount of light measured by the fibre optics can be retrieved as seen in Figure 4.5. After coupling the MMF, 10% of the maximum amount of light should be retrieved from it when no aberrations are present. This amount of light should serve as the maximum and ideal amount of light retrieved by the system. When aberrations are present, this amount of light will be reduced. The fibre-optics coupling is then calculated by the ratio between the incoming light intensity measured, I_{in}, and the maximum intensity measured

[8] https://www.thorlabs.com/newgrouppage9.cfm?objectgroup_id=1564&pn=PAX1000IR1/M, retrieved on 12-06-2023

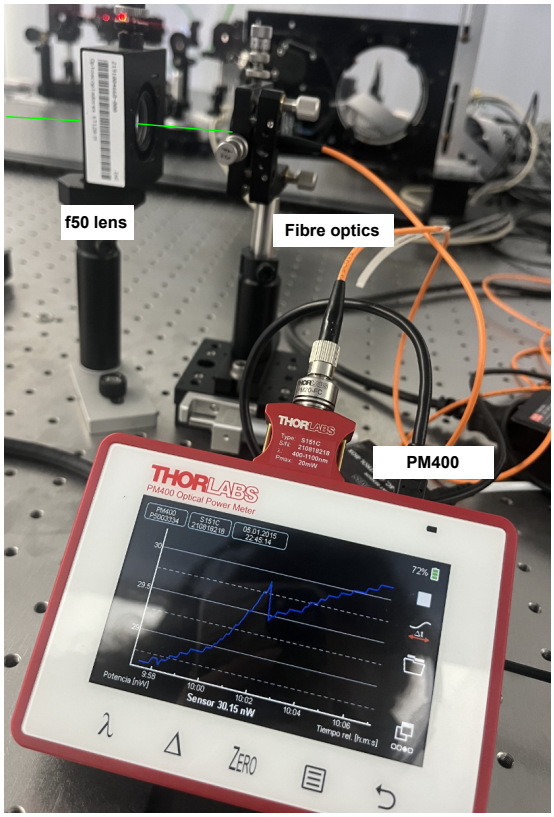

Figure 4.5: PM400 measurements for the optical fibre coupling.

Table 4.6: Properties of Thorlabs' PM400 Optical Power and Energy Meter Console [9].

Property	**Value**
Display	
Type	400 pixels x 272 pixels, 16 bit Color
Viewing Area	95 mm x 54 mm
Update rate (max)	10 Hz Numerical, 25 Hz Analog Simulation
Analog Output	
Voltage range	0 to 2 V
Accuracy	± 3%
Bandwidth	100 kHz
General	
Dimensions	136 mm x 96 mm x 29 mm
Weight	0.35 kg

when no aberrations were introduced, I_{ideal}:

$$FO = \frac{I_{in}}{I_{ideal}} \tag{4.3}$$

Note that a multi-mode fibre is used instead of an single-mode fibre, as intentionally stated in requirement **TOGS-DR-03**, because there was no single-mode fibre available in the

[9] https://www.thorlabs.com/newgrouppage9.cfm?objectgroup_id=10562&pn=PM400, retrieved on 12-06-2023

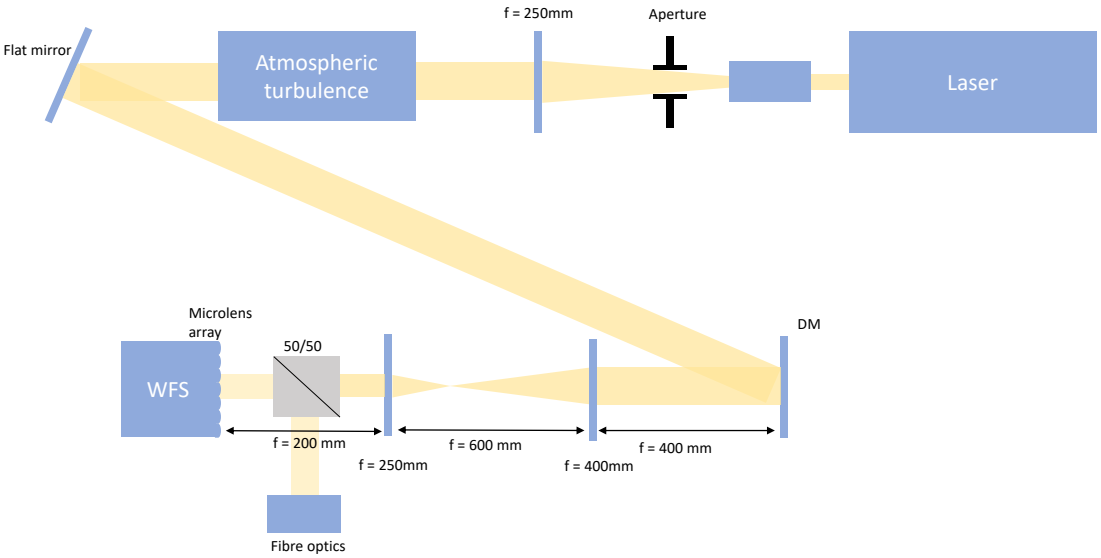

Figure 4.6: Test set-up diagram

laboratories of IAC. However, this should not affect the measurements as a single wavelength laser is used to model the light source. The only difference is that the diameter of the MMF is larger than most SMFs.

4.6 Experimental test set-up

In Figure 4.6 a flow chart is created of the test set-up. The collimated LDM 635 laser passes first through an amplifier that diverges the beam. The source is then spatially filtered by an aperture, also known as a pinhole, of 10 microns. This allows to constrain the laser beam width to only the centre of the light source, which is the most intense and most uniformly distributed part. Then, the laser beam is collimated with an f250 lens, meaning the lens is placed at 250 mm of the pinhole to collimate the light source again. Next, it will travel through the optical path until the Lexitec motorised rotary stage with the turbulent phase plate, which simulates a single turbulent layer atmosphere. After the light source is aberrated, it will continue until reflected by a flat mirror and continue its path to the DM.

After hitting the DM, the optical path is reflected towards a relay, which scales the image of the DM, to the image of the WFS. This step is necessary to scale the pitch of the actuators with the pitch of the microlens arrays. Since the actuator pitch equals 400 μm and the microlens array pitch of the WFS equals 150 μm, the scaling ratio should be 150/400 = 3/8. Therefore, the relay consists of an f400 and an f150 lens. The relay follows the inverse of the set-up of a beam expander, as seen in Figure 2.1. Thus, the DM is placed 400 mm in front of the first lens, the second lens of the relay is placed at a distance of 550 mm from the first lens, and the WFS is placed 150 mm away from the second lens. After passing the relay, the optical path will be split by a beam splitter and travel to the WFS and an f50 lens, which converges the light source where a fibre optics coupling is placed 50 mm away from this lens. The correction by the DM is then measured based on the amount of light measured by the fibre optics. A front view and side view of the actual test set-up with these hardware components is depicted in Figure 4.7 and Figure 4.8, respectively.

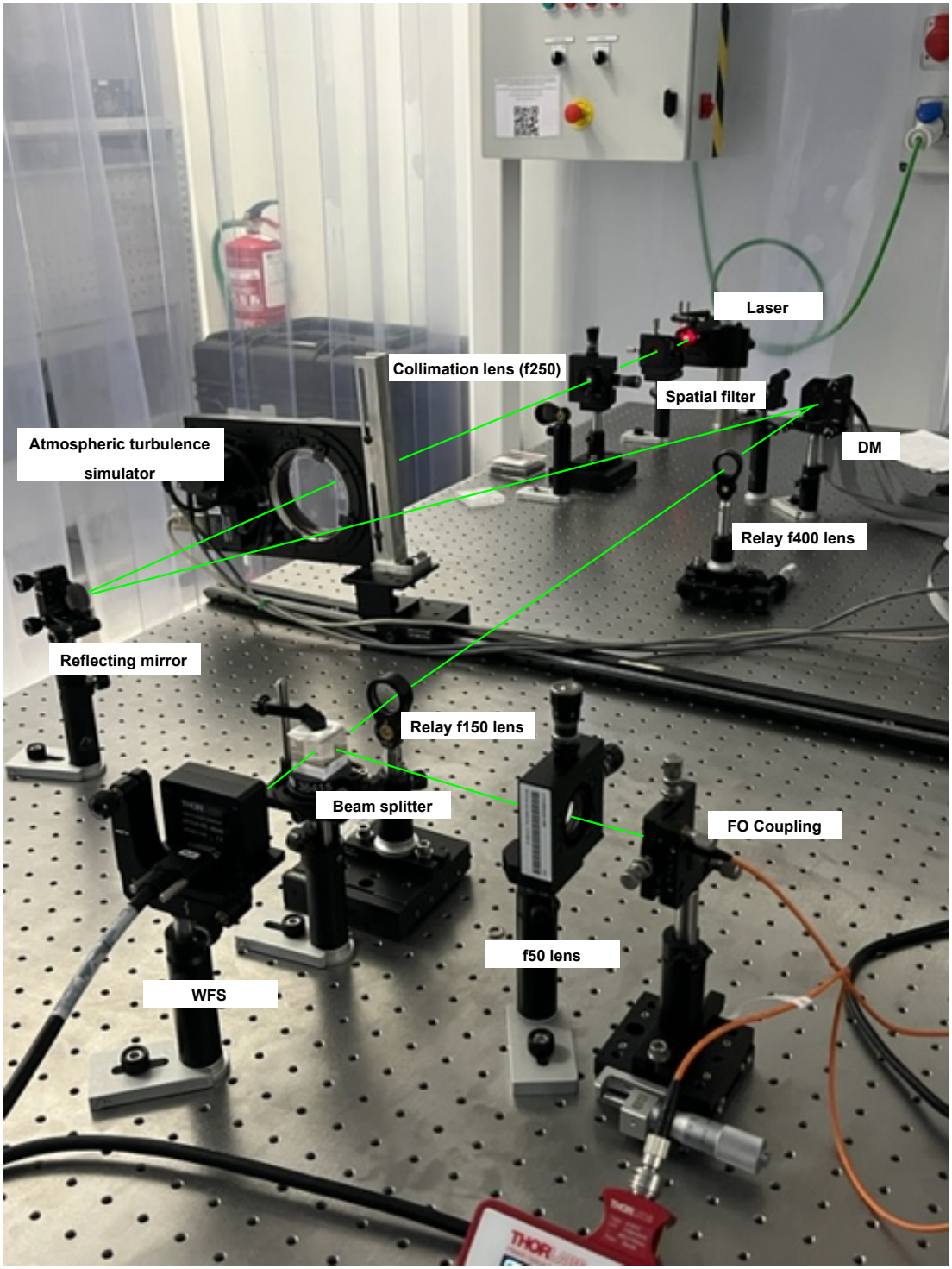

Figure 4.7: Test set-up side view

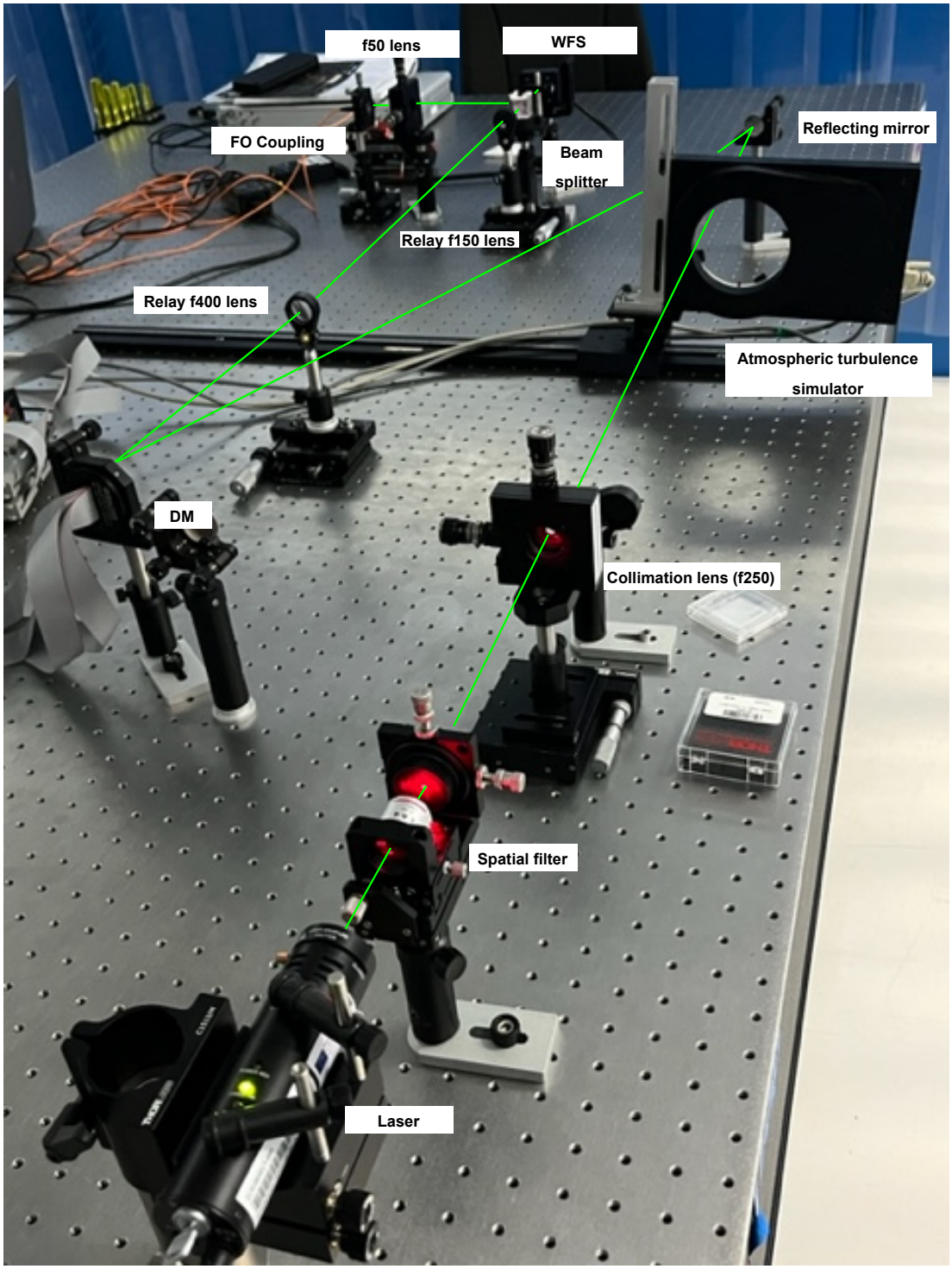

Figure 4.8: Test set-up front view

CHAPTER

5 Adaptive-optics system modeling

To study the behaviour of the designed controller on the AO system, SW simulations will be initially performed. Section 5.1 discusses the open software and SW platform that will be used. Next, the system model is elaborated upon, including a detailed description of all components of the AO system in Section 5.2. Then, the graphical use interfaces used to interact with the HW components in the experimental set-up will be touched upon in Section 5.3. Finally, the verification tests performed to verify the SW code are stated in Section 5.4.

5.1 Software platform

Object–Oriented Matlab Adaptive Optics (OOMAO) will be used to recreate the adaptive optics system. It is a Matlab toolbox dedicated to Adaptive Optics (AO) systems. OOMAO is based on a set of classes, each representing an object of the system, such as the source, atmosphere, telescope, WFS, DM or an imager for the AO system. These classes allow simulating Natural Guide Stars (NGS) and Laser Guide Stars (LGS), Single Conjugate AO (SCAO), and tomography AO systems on telescopes up to the size of the Extremely Large Telescopes (ELT). The discrete phase screens that make the atmosphere model can be of infinite size, and are useful for modeling system performance on large time scales. OOMAO comes with its own parametric influence function model to emulate different types of DMs. Also, OOMAO has an extensive library of theoretical expressions to evaluate the statistical properties of turbulence wavefronts. OOMAO has been used before in the design process of the Multi–Object AO prototype Raven at the Subaru telescope and the laser tomography AO system of the currently under construction Giant Magellan Telescope, in Chile (Conan and Correia, 2014).

5.2 System model

To design the control system for the AO system, the components of the system have to be understood. Therefore, a system SW architecture is made and depicted in Figure 5.1. As seen, the system consists of three main components: a wavefront sensor, a deformable mirror and a controller. The controller will be addressed in Chapter 7. All the models for the other components will be explained in detail here, including the classes used to simulate them. Moreover, the input parameters for each class will be given.

A flowchart of these classes is given in Figure 5.2. The classes are separated each with an individual colour. The sub-classes are denoted with a lighter shade of the corresponding main colour of the class. Propagation of the classes is marked with a cross '×'.

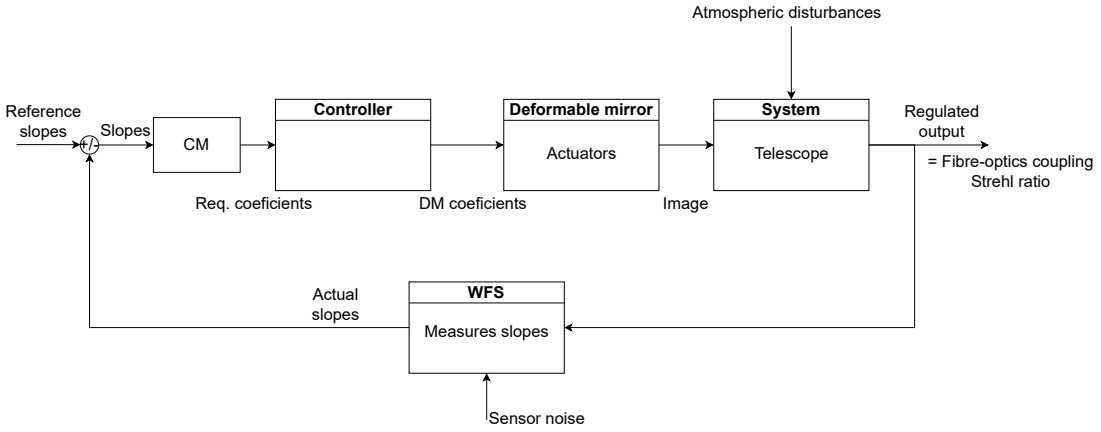

Figure 5.1: System architecture

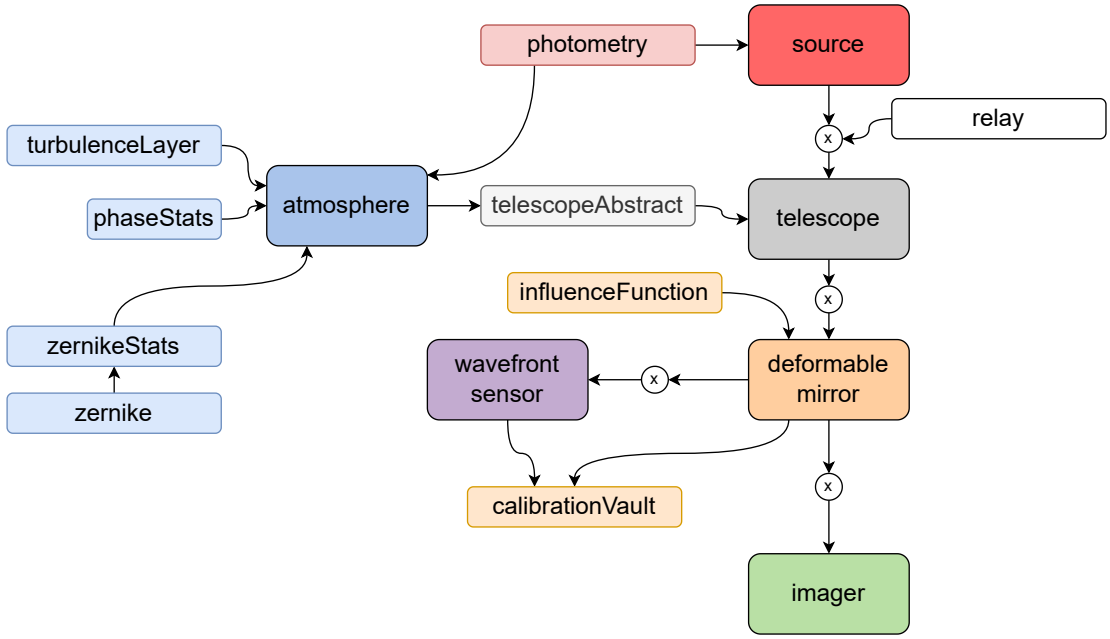

Figure 5.2: Flowchart of the OOMAO

Atmospheric perturbations

OOMAO created the atmosphere class to simulate the atmospheric perturbations that cause the wavefront aberrations. The atmospheric model follows the Kolmogrov theory, which is the set of hypotheses suggesting that a small-scale structure is statistically homogeneous, isotropic, and independent of the large-scale structure. The source of energy at large scales is either wind shear or convection. When the wind velocity is sufficiently high, large unstable air masses are created. The theory assumes that energy is added at the largest scale of the system, also known as the outer scale, L_0. Then, the energy cascades from larger to smallest scales, which means that the turbulent eddies "break down" into smaller structures until the eddy size becomes so small that it is subject to dissipation from viscosity, also known as the inner scale, l_0 (Max, 2014). The turbulence layers computed in the atmospheric class, are grouped as a sub-class itself called "turbulenceLayer" and is called within the atmosphere object.

Table 5.1: The input parameters and properties of the atmosphere object created by OOMAO.

Input Parameters	**Parameter name**	**Input OOMAO**
required	Wavelength Fried parameter Outer scale	photometry.V (550 nm) 0.06-0.2 m 30 m
Optional	Altitude Fractional fried parameter Wind speed Wind direction	0 m 1 15 m/s 0 rad
Output parameters	Turbulence layer properties Phase screen generation	

The OOMAO atmospheric class required the inputs stated in Table 5.1. The wavelength is given through another class called "photometry", where predefined wavelengths can be called through the corresponding letter. Here, the visible range is desired and, therefore, the a wavelength of 550nm will be called using the letter V. The inputs are used to compute the atmospheric turbulence layers, which in turn serve to compute the phases at each pixel of the telescope resolution. Thus at the end, an nPx by nPx phase matrix is computed. This phase screen is retrieved as follows. First, the phase covariance is computed using the von Karman phase structure function (Irbah et al., 2016):

$$D_\phi(r) = \frac{\Gamma(11/6)}{2^{-1/6}\pi^{8/3}}\left[\frac{24}{5}\Gamma(6/5)\right]^{5/6}\left(\frac{r_0}{L_0}\right)^{-5/3} \times \left[\frac{5/6}{2^{1/6}} - \left(2\pi\frac{r}{L_0}\right)^{5/6} K_{5/6}\left(2\pi\frac{r}{L_0}\right)\right] \tag{5.1}$$

where r, r_0, and L_0 are the spatial vector, the Fried's parameter and the outer scale length, respectively. $K_\nu(r)$ is the modified Bessel function of the third kind known as the McDonald function, and $\Gamma(s)$ is the Gamma function. This equation is called upon from the class called "phaseStats".

Then, a square phase screen of D meter and sampled with n pixels using the Cholesky factorisation of the atmospheric phase covariance matrix is created. This method decomposes a positive-definite matrix into the product of a lower triangular matrix and its conjugate transpose. To do this, samples are created with a 2-D meshgrid with a size equal to the amount of pixels. The sample values go from $-D/2$ to $D/2$. Also, a Toeplitz matrix is created using the phase covariance function. A Toeplitz Matrix, $\mathbf{T}$, is a diagonal-constant matrix, which means that elements along a diagonal have the same value. Next, the Cholesky factor of matrix $\mathbf{T}$ is computed using the diagonal and upper triangle of the matrix, such that $\mathbf{T} = \mathbf{R}'\mathbf{R}$. $\mathbf{T}$ must be positive definite, and the lower triangle is assumed to be the (complex conjugate) transpose of the upper triangle, which is retrieved from the complex values of the meshgrid. Finally, a phase "map" is created by multiplying the Cholesky factor by a random atmospheric stream generator and an nPx by nPx matrix is obtained. Moreover, Zernike polynomials will be used to describe optical system aberrations types described in Chapter 3. These are a set of orthogonal polynomials that arise in the expansion of a wavefront function for optical systems with circular pupils. They are usually described in terms of normalised polar coordinates $Z_n^m(\rho,\phi)$, where n describes the power of the radial polynomial, m describes the angular frequency, ρ is the radius in the image phase in the normalised plane, and θ is the angle between image phase and x axis. The Zernike polynomials are modelled for each aberration in the class "zernike" and "zernikeStats" and are called upon in

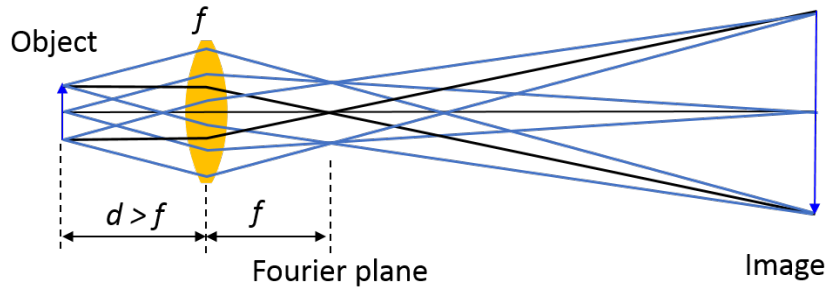

Figure 5.3: Definition of a Fourier plane [10].

the atmosphere class. As mentioned in Chapter 3, the low-order aberrations, such as tip/tilt, defocus, astigmatism and coma, are the most present. These aberrations can be represented by low-order Zernike polynomials. (Niu and Tian, 2022).

For example, tilt aberration is the first order of Zernike Polynomials and comprises 87% of the energy from a wavefront aberration. For tilt in the y-direction, n equals 1 and m equals -1. For tilt in x-direction, n equals 1 and m equals 1 (Liu et al., 2020):

$$\begin{aligned} y &: Z_n^m(\rho,\theta) = 2\rho\sin(\theta) \\ x &: Z_n^m(\rho,\theta) = 2\rho\cos(\theta) \end{aligned} \tag{5.2}$$

$$\begin{aligned} y &: Z_n^m(\rho,\theta) = 2\rho\sin(\theta) \\ x &: Z_n^m(\rho,\theta) = 2\rho\cos(\theta) \end{aligned} \tag{5.3}$$

Telescope

The telescope class creates a telescope object from the inputs stated in Table 5.2. The outputs contain the shape and crucial telescope properties. For instance, when working with wavefront aberrations, understanding the pupil properties is important. According to Fourier optics, the wavefront is defined in the exit pupil system and is the Fourier transform of the Point Spread Function (PSF), which is also known as the Optical Transfer Function (OTF). The PSF is a representation of the image quality and is a two-dimensional distribution of light in the instrument focal plane for point sources. The PSF is reconstructed using the cross-sectional area of the telescope and the Bessel function of first kind:

$$J_\nu(\mathbf{z}) = \left(\frac{\mathbf{z}}{2}\right)^\nu \sum_{k=0}^{\inf} \frac{\left(\frac{-z^2}{4}\right)^k}{k!\Gamma(\nu+k+2)} \tag{5.4}$$

Here, z is the input usually defined as an array, k is the number is elements in that array, ν is a positive integer defining the order of the Bessel function, and $\Gamma(\nu+k+2)$ is the gamma function of $(\nu+k+2)$. The Bessel function is used to express the sum of phase contributions from the points on the wavefront. This form, replaces much more involved direct integration (Kraus and Welty, 2001).

It is often evaluated by a comparison of the corresponding Full-Width Half Maximum value (FWHM), which is the value for the width of the function where the intensity is half its maximum value (Kamp, 2007). Note that, the pupil plane is not an actual physical plane, but a Fourier plane as seen in Figure 5.3. Additionally, the telescope class depicts the movement of the aberration according to the allocated wind speed as seen in Figure 5.4.

[10] https://www.linkedin.com/pulse/taking-fourier-plane-out-objective-lens-dileep-kottilil/,

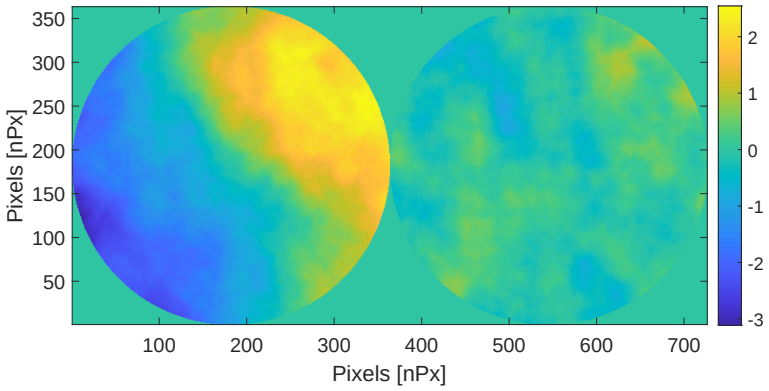

Figure 5.4: Movement of the aberrations with the corresponding wind speed.

Table 5.2: The input parameters and properties of the telescope object created by OOMAO.

Input Parameters	**Parameter name**	**Input TOGS**
Required:	Diameter	0.7 m
Optional:	Obstruction ratio	-
	Sampling time	0.001 s
	Field of view	-
	Resolution (nPx·nLenslet)	32·11 px
	Optical Aberration	-
Output parameters	Telescope area	
	Telescope pupil	
	Telescope shape	
	Fourier transform of telescope pupil	
	Phase screen (displacement)	
	Optical transfer function	
	Point spread function	
	Full Width Half Maximum	

Source

The source object carries a wavefront, both amplitude and phase, through different objects representing the atmosphere, the telescope, the wavefront sensor, and the deformable mirror. Both a Natural Guide Star (NGS) and a Laser Guide Star (LSG) can be simulated. The input and outputs are stated in Table 5.3. Asterism simply refers to the use of a small group of stars instead of a single star as a source. Moreover, the zenith angle is defined between the zenith of an observer, which is the celestial point vertically above a certain position or observer, and the astronomical object. The azimuth angle is the direction in which an astronomical object appears. The azimuth is measured from true north in eastward direction. The angles are visualised in Figure 5.5. Additionally, a height can be set so the source becomes a LGS. Here, the a wavelengths of 1550nm and 2179nm will be used, which are called upon using the letters H and K, respectively. Moreover, the magnitude of the source is calculated here, which serves as an indication for the amount of photons received per square

retrieved on 27-04-2023

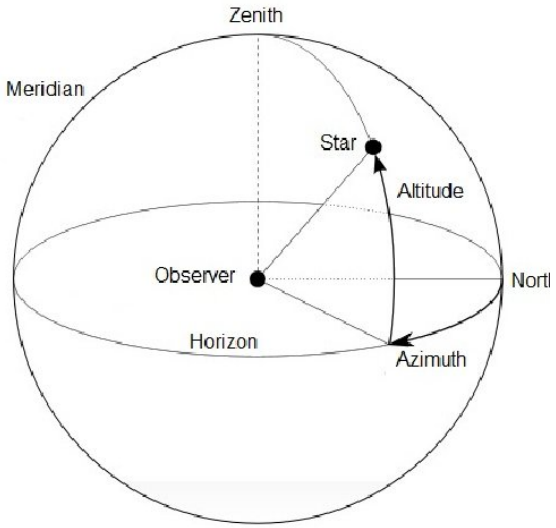

Figure 5.5: Schematic of the zenith and azimuth angles of a source object [11].

meter per second, also known as the luminosity. It is a measure of the brightness of an object in a defined pass band. The relation between the luminosity L and the magnitude M is given by (Cameron, 1993):

$$L = L_0 10^{0.4M - M_0} \tag{5.5}$$

where L_0 and M_0 is the luminosity and the absolute bolometric magnitude of the Sun. The output includes the optical path, which in turn serves to propagate the source through other objects of the AO system. The source class propagates the source by multiplying the source amplitude by the transmittance of the intended object and adding the phase of that object to the source's phase. The function describing this is called from the "relay" class. After the source is propagated, the source class also updates the operator by streaming the source object through its optical path. The Optical Path Difference (OPD) is calculated as follows:

$$OPD = \frac{\phi\lambda}{2\pi} \tag{5.6}$$

where ϕ is the changing phase and λ is the wavelength.

Wavefront sensor

OOMAO offers a Shack-Hartmann sensor object, which requires the input seen in Table 5.4. The total resolution defined in pixels, called from the telescope class, is divided by the number of lenslets to obtain an image of equal quality in each lenslet of the entire lenslet array. From the deviation of the spot image with respect to the centroid of the corresponding lenslet, the x- and y- coordinate is obtained, which results in the wavefront sensor slopes. Additionally, the class allows to add noise effects. The noise effects that can be added numerically are:

1. Readout noise:
   Noise generated when producing the electronic signal during the readout process due the electrons being subjected to the analog to digital conversion.

[11] https://www.researchgate.net/figure/\protect\discretionary{\char\hyphenchar\font}{}{}The-horizontal-coordinate-system-The-pole-of-the-upper-hemisphere-is-the-zenith_fig1_287645191, retrieved on 27-04-2023

Table 5.3: The input parameters and properties of the source object created by OOMAO.

Input Parameters	**Parameter name**	**Input TOGS**
(all optional)	Wavelength Asterism Zenith Azimuth Height Magnitude Width	prop. source: photometry.H (1550nm) scientific camera: photometry.K (2179 nm)
Output parameters	Optical path difference Source propagation Updates stream operator	

Table 5.4: The input parameters and properties of the Shack-Hartmann object created by OOMAO.

Input Parameters	**Parameter name**	**Input TOGS**
required	Lenslets Resolution min. Light ratio	11 Same as telescope 0.5
Output parameters	Slopes Noise	

2. Photon noise:
   The statistical noise associated with the arrival of photons at the pixel.

3. Dark current:
   The accumulation of thermal energy, which causes thermal electrons to build up on the sensor when the imaging device is exposing an image.

4. Quantum Efficiency:
   The measure of the effectiveness of an imaging device to convert incident photons into electrons.

Deformable mirror

A deformable mirror is composed of a thin membrane with many actuators underneath, which can be controlled individually. By adjusting the actuator stroke, the deformable mirror corrects for the incoming atmospheric aberrations measured by the wavefront sensor. OOMAO allows to create a deformable mirror model as follows. A numerical deformable mirror is made of a set of influence functions or modes defined in the “influenceFunction” class. In OOMAO, a mode shape is derived from two cubic Bézier curves (Conan and Correia, 2014):

$$\begin{aligned} B_1(t) &= \left(1-t^3\right)P_0 + 3(1-t)^2 t P_1 + 3(1-t)t^2 P_2 + t^3 P_3, t \in [0,1] \\ B_2(t) &= \left(1-t^3\right)P_3 + 3(1-t)^2 t P_4 + 3(1-t)t^2 P_5 + t^3 P_6, t \in [0,1] \end{aligned} \tag{5.7}$$

$P_k = (x_k, z_k)$ are points in the $x-z$ plane. As t varies from 0 to 1, $B_1(t)$ will go from P_0 to P_3 and $B_2(t)$ will go from P_3 to P_6. P_0 will correspond to the highest point of the mode and is

Table 5.5: The input parameters and properties of the deformable mirror object created by OOMAO.

Input Parameters	**Parameter name**	**Input TOGS**	**Input Lab**
required	Number of actuators	12	12
optional	Modes Resolution	Call bif Same as telescope	Call bif Same as telescope
Output parameters	Valid actuators Least squares fit Fitting error Actuator coefficients DM shape		

set to the coordinates $(x_0 = 0, z_0 = 1)$. The derivative of the mode at P_0 must be zero, this is ensured by setting $z_1 = 0$. The mode is forced to zero at P_6 by setting $z_6 = 0$. x_6 is set to 2. The derivative of the mode in P_6 is forced to zero by setting $z_5 = 0$. To ensure a smooth junction between both Bézier curves, the following condition is imposed $P_3P_2 = -\alpha P_3P_4$ leading to $P_4 = -P2/\alpha + (1 + 1/\alpha)P_3$.
From the conditions stated above, a DM mode is set with the following parameters: x_1, (x_2, z_2), (x_3, z_3), α and x_5. An influence function is created with two arguments passed to its constructor: the list of parameters in a cell and the mechanical coupling value. Instead of the list of parameters, the keywords $'monotonic'$ (0.2, [0.4, 0.7], [0.6, 0.4], 1, 1) and $'overshoot'$ (0.2, [0.4, 0.7], [0.5, 0.4], 0.3, 1) can be used to call predefined parameter lists.

The 1-D half plane mode is obtained by concatenating both Bézier curves:

$$B(t) = [B_1(t), B_2(t)] \tag{5.8}$$

$B(t)$ is a vector of $x-z$ coordinates, $B(t) = (B_x(t), B_z(t))$. $B_x(t)$ is normalised by $B_x(t_c)$; $B_x(t_c)$ is the x coordinate where $B_z(t) = c$, with c being the mechanical coupling of the DM actuators. The full 1–D mode $M(t)$ is made by concatenating $B(t)$ and its symmetric with respect to the z axis, i.e,

$$M_x(t) = ([B_{-x}(t), B_x(t)], [B_z(t), B_z(t)]) \tag{5.9}$$

The 2–D mode is the product of the 1-D modes in the $x-z$ plane and in the $y-z$ plane,

$$M(t) = M_x(t)M_y(t) \tag{5.10}$$

In Table 5.5, it is seen that the input parameters are the number of actuators on de diagonal of the deformable mirror, which means there are n by n actuators in total. Furthermore, the mode used to calculate the influence function that is computed with the Bézier curves (bif) is called upon, and the resolution stating the sampling pixels, which is the same as the telescope object. However, the actuators in the corners do not correct for aberrations. Therefore, the program computes the valid actuators that will be commanded to correct the aberrations. Once the valid actuators are known, the stroke of each actuator, equal to $3.5{\cdot}10^{-6}$ m, is used to compute the required actuator amplitudes. These are known as actuator coefficients. Moreover, the object includes a least square fit method to fit the influence function previously explained, and calculates the fitting error.

Calibration process

Furthermore, to calculate the DM shape that fits the measured aberrations best, the AO system has to be calibrated. This means that the transfer function from the DM to the WFS has

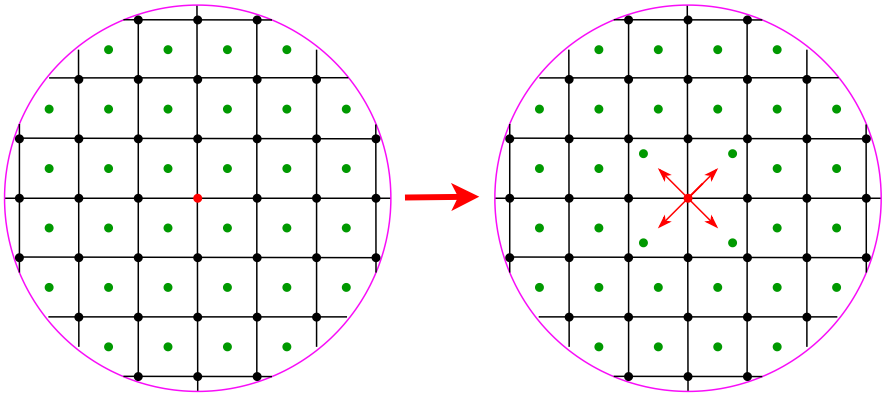

Figure 5.6: Fried configuration

to be measured. An easy way of doing the calibration is to push the individual DM actuators one after the other and measure the corresponding response vectors of the WFS, observing a reference source located in a focal plane in front of the DM. This can be a tedious procedure for high-order AO systems with many actuators, noisy measurement conditions caused by photon noise, and aberrations between the reference source and the WFS that vary during the calibration. The latter disturbance can become severe if the distance between the reference source and the WFS is large or if a natural star has to be used as a reference. This could be solved either by taking very long measurements to cancel the aberrations by averaging, or by taking very short measurements, such that the aberrations can be considered frozen.

OOMAO has a predefined calibration function within the deformable mirror class that calculates this interaction matrix. The interaction matrix between the wavefront sensor and the deformable mirror explains the relation between the retrieved image and the actuator movements of the DM. Ideally, it follows the Fried Configuration, which is a configuration where each actuator is placed in the intersection of the microlens arrays as seen in Figure 5.6. Here, the lenslets are the white squares, the actuators are defined as black dots on the intersection of the squares, and the green dots are the spots imaged by the camera. So, when moving one of the actuators, denoted in red on the right side of the image, the spots in the four surrounding microlens arrays should move as depicted (Wang et al., 2017).

With this said, interaction matrix is derived by normalising the influence functions to 1, followed by setting the stroke of the actuators to $\pm$ 3.5·10^{-6} m, which indicates the maximum and minimum actuator displacement. Note that the stroke value is directly related to the control saturation, as this is the range within the actuator is able to move to correct for the aberrations as mentioned in Chapter 2. The calibration process then "pokes" each actuator with the given stroke value and calculates the corresponding spot displacements measured by the WFS for each lenslet of the microlens array with respect to the reference centroids, which are ideally equal to 0. Note that four spots will be moved every time one actuator is poked when the system follows the Fried configuration. As mentioned before, the four slopes have each an x- and y-coordinate, which are saved for all images of each lenslet every time an actuator is moved. Thus, a $2mxn$ interaction matrix can be constructed, m being the amount of lenslets and n the actuators. This results in the image seen in Figure 5.7(a). As seen, the interaction matrix are slopes, meaning that every time an actuator is moved, the four surrounding microlens arrays are moved with respect to the reference centroids. Therefore, four sets of slopes are seen. The yellow lines denote the displacement in the negative direction, whereas the blue lines denote the displacement in the positive direction. Additionally, note that the four spots will ideally move an equal amount from the poked actuator,

Table 5.6: The input parameters and properties of the calibration function created by OOMAO.

Input Parameters	**Parameter name**	**Input TOGS**
required	Deformable mirror	Call DM object
	Wavefront sensor	Call WFS object
	Calibration source	Call source
	Actuator stroke	$3.5{\cdot}10^{-6}$ m
Output parameters	Interaction matrix	

meaning that the values of the x-coordinates are equal and the value of the y-coordinates are equal, but in opposite direction. The input parameters required by the function are stated in Table 5.6, and simply consist of calling the previously mentioned objects, including the WFS object, the source object, the DM object, and the actuator stroke value.

The command matrix is then obtained by computing first the singular value decomposition of the interaction matrix, which is composed of a matrix containing the left singular vectors, **U**, a matrix with the singular values **S**, and a matrix with the right singular values **V**. The 4 last eigen values are filtered out and an inverse matrix of **S** is created. The command matrix simply becomes:

$$\mathbf{CM} = \mathbf{VS^{-1}U} \tag{5.11}$$

OOMAO created a class called "calibrationVault" that includes the singular value decomposition method to obtain de command matrix. The retrieved command matrix should look like the one depicted in Figure 5.7(b). Here, an inverse of Figure 5.7(a) is shown, hence, the significant low values in the order of 10^{-7}. Again, four sets of slopes can be seen due to the movement of the four microlens arrays with respect to the reference centroids every time an actuator is moved. The yellow lines denote the displacement in the positive direction, whereas the blue lines denote the displacement in the negative direction. It can be clearly seen that, starting for actuator one, the four first lenslets are moved. Note that every lenslet movement in the x-direction is paired with a movement in the y-direction. Hence, the two separate pairs of slopes.

Science camera

A science camera will be used to measure the image quality retrieved after the aberration is corrected by the deformable mirror. OOMAO created the class "Imager" to create the science camera object. A source is created in the H-band that will propagate through the science camera. The optional input refers to the resolution of the detector in the Shack-Hartmann sensor.

The parameter to measure the image quality is called the Strehl ratio, which is defined as the normalised peak intensity of the PSF of the lens. It is calculated as follows. First, the intensity at each pixel that constructs an nPx by nPx frame is measured in the camera, which is then summed and normalised to retrieve the intensity and the location of the peak when no aberrations occur. Then, the same is performed with aberrations. The Strehl ratio, S, results in:

$$S = \frac{I_{real}(0,0)}{I_{ideal}(0,0)} \tag{5.12}$$

which results in a number between 0 and 1. An illustration of the obtained intensity peaks is given in Figure 5.8, where the difference between the intensity of an aberrated image is

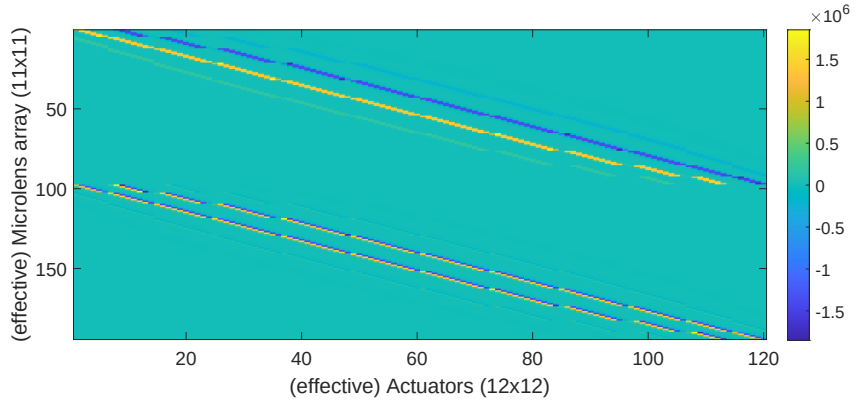

(a) Interaction matrix retrieved from OOMAO

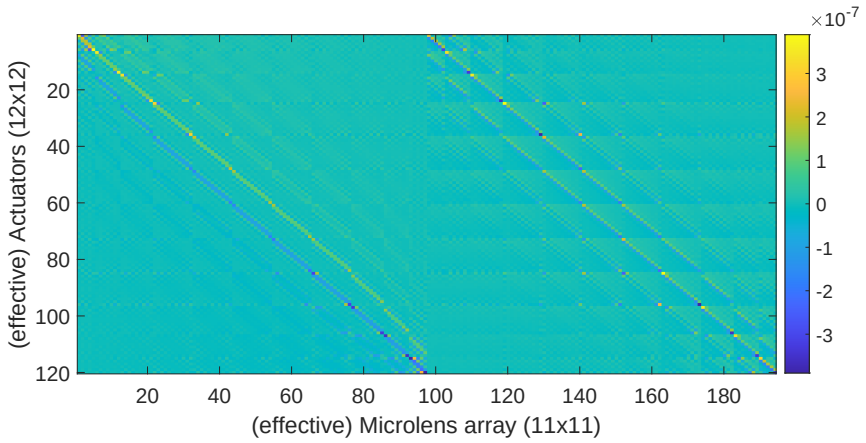

(b) Command matrix retrieved from OOMAO

Figure 5.7: Calibration process in OOMAO

plotted against the intensity of a non-aberrated image. Taking the ratio of the maximum of these plots results in the Strehl ratio.

Fibre optics

OOMAO has a built-in function within the "Imager" class that outputs the camera frame. This function measures the intensity of light per pixel within the frame. Using this function, the quantity of light actually absorbed by a fibre-optics coupling can be computed.

The quantity of light is measured before a fibre-optics coupling for the entire telescope system. Then, a smaller frame is defined, which corresponds to the opening of the fibre-optics coupling. The quantity of light measured is centred around the maximum amount of light. Similar to the Strehl ratio, dividing the amount of light before and after the fibre optics coupling results in the maximum amount of light that can be measured by the system when no aberrations occur (M. Chen et al., 2015).

Then, the same is done after the atmospheric effects are added and after the controller is placed in the CL system. Using this, the ratio between the light with atmospheric aberrations and the light with the correction provided by the controller can be computed, which defines the performance of the AO system with the designed controllers.

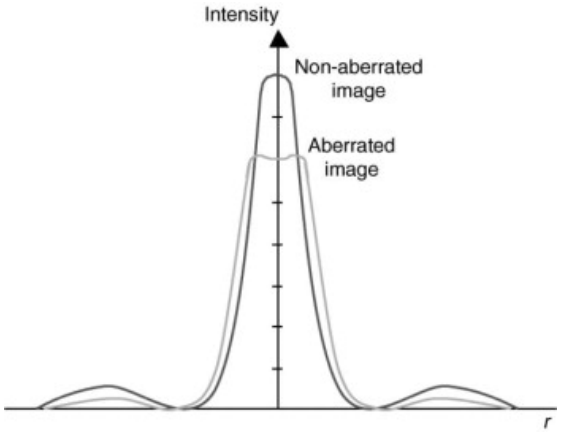

Figure 5.8: An illustration of the Strehl ratio principle (Ottevaere and Thienpont, 2005).

Table 5.7: The input parameters and properties of the imager object created by OOMAO.

Input Parameters	**Parameter name**	**Input TOGS**
Optional	Resolution	-
Output parameters	Strehl ratio	

Summary of the OOMAO SW objects

To conclude this section, a summary is given in Table 5.8 of all the classes defined by OOMAO that will be used to create the model of the system. Note that, OOMAO includes many more files with classes. However, these classes are not touched upon as they are not crucial for the model created for this specific AO system.

Table 5.8: Summary of all the classes that will be used to recreate the model of the system.

Class name	**Description**
atmosphere	Creates the atmosphere object containing information about the predefined turbulence layers, including the calculation of the phases, and phase screen generations.
phaseStats	Includes the function to calculate the covariance of each turbulence layer, the Toeplitz matrix conversion and many other functions related to the phase to retrieve statistical information about each turbulence layer.
turbulenceLayer	Creates the turbulence layer objects within the atmosphere object with all of the corresponding information, including the phases.
zernike	Includes all polynomials to represent the different types (low-order) aberrations .
zernikeStats	States all functions for to calculate the Zernike statistics with, for example, different types of power spectrum densities. .

Table 5.8: Summary of all the classes that will be used to recreate the model of the system.

Class name	**Description**
telescope	Creates the telescope object, including the generation of its area and shape & pupil, the Fourier transform of the telescope pupil, the phase screen generation, the PSF and the FWHM.
telescopeAbstract	Creates the telescope properties as input for the telescope class, including the generation of its area , shape & pupil, and the Fourier transform of the telescope pupil.
source	Creates a source object, which can either be a NGS, or a LGS. It includes the functions for source propagation, stream operator and the calculation of the OPD.
photometry	Includes the predefined wavelength that are connected to a specific letter, which allows to call the letter directly as wavelength instead of adding a number as input. Moreover, it calculates the magnitude of the source that indicates the luminosity of the source.
relay	Sets the amplitude and phase of the source object based on the wave input, which serves to propagate the source in the source class.
influenceFunction	Creates the modes required for the deformable mirror object using the Bezier curves. Also, the Zernike modes are included to create an additional tip tilt mirror (not used here).
deformableMirror	Creates the deformable mirror object from the influence functions. It computes the coefficient for each actuator from the corresponding strokes, and created the DM shape. Furthermore, it includes the calibration function to create the interaction matrix.
calibrationVault	Contains the singular value decomposition to retrieve the command matrix from the interaction matrix.
shackHartmann	Creates the Shack-Hartmann object by using the detector class. It includes the computations for the measured slopes, which result from the deviations of the placement of the image with respect to the centroid for each of the lenslets in the array computed using correlations.
detector	The detector class is used in the Shack-Hartmann class to create the detector, and all the crucial noise effects that come with the detector.
imager	A scientific camera object is created with this class, and the image quality in terms of Strehl ratio is obtained.
lensletArray	Contains the function for the Fraunhoffer wave propagation to the lenslets focal plane, which is needed to compute the intensity in the frame of the scientific camera to obtain the Strehl ratio.

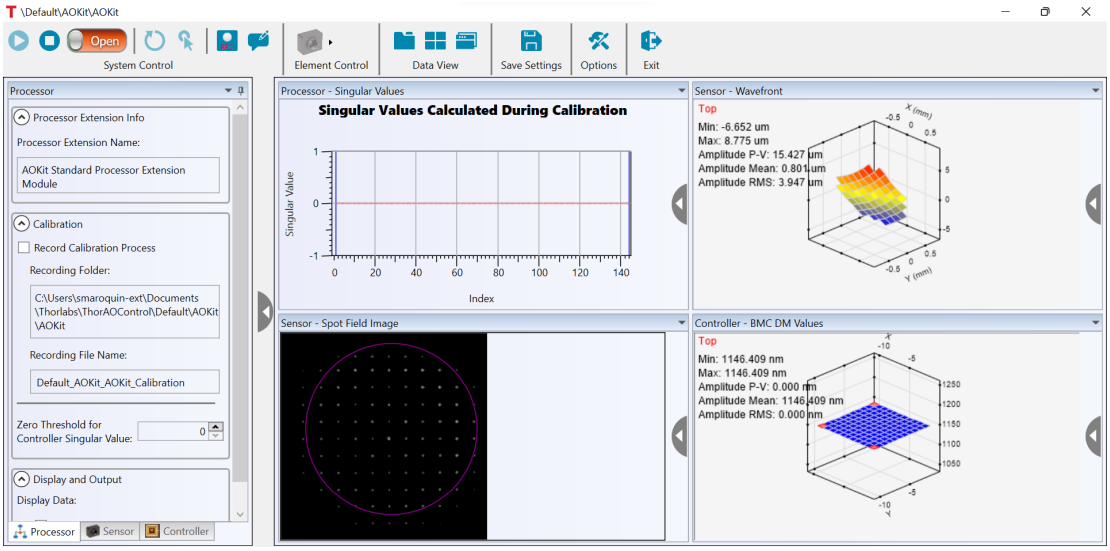

Figure 5.9: GUI platform of Thorlabs.

5.3 Graphical user interfaces for the hardware components

To measure the WFS, Thorlabs' Graphical User Interface (GUI) will be used that comes with the HW components. The program allows to see the spotfield image of the camera, as well as the aberrations measured, actuator's movement and the singular values computed from the calibration process as seen in Figure 5.9. In the section of the left size of the image, the calibration process can be recorded and saved in the Processor tab in the lower left corner. In the Sensor and Controller tab, the WFS and DM properties can be filled in and adjusted, respectively (Thorlabs, 2020a). Once the AO system is installed, the GUI allows to compute the interaction matrix using the same method as stated in Section 5.2. The actuator movement during the calibration process is shown in Figure 5.10. Here, wavefront aberrations caused by an actuator movement are shown on the left-hand side, while actuator grid is shown on the right-hand side. Number two was moved as an example, which is seen on the right-hand side with a dark grey peak. This caused the aberration peak close to the edge as seen on the left-hand side, which is expected as actuator number two is placed on the top edge of the actuator grid. Each individual actuator movement is paired with a single intense wavefront aberration peak similar to this one.

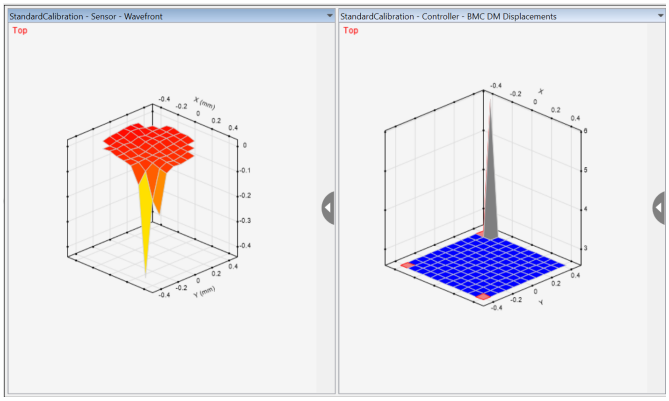

Figure 5.10: Wavefront measured (left) when actuators of DM are moved with a stroke of 0.8 (right).

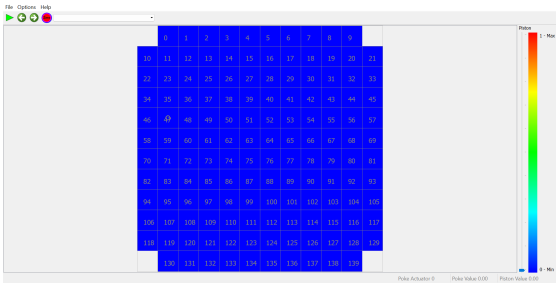

Figure 5.11: DM Shape display

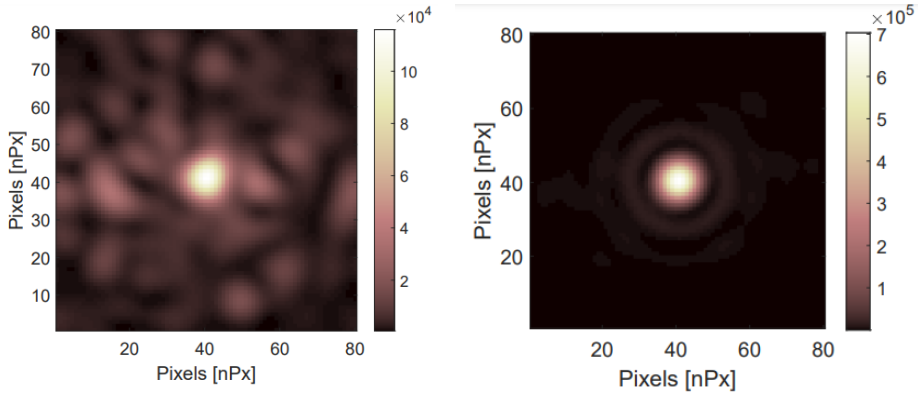

(a) Image quality for a source wavelength of 550 nm

(b) Image quality for a source wavelength of 1550 nm

Figure 5.12: Image quality depending on the wavelength of the source

Furthermore, the actuators could be controlled individually using another SW platform from Boston Micromachines called “DM Shapes”. As seen in Figure 5.11, the actuators are depicted individually. By clicking on the chosen actuators, the actuator movement can be changed individually and the effect can then be seen in the spotfield image constructed by the WFS in the lower left image of Figure 5.9 (BostonMicromachines, 2020).

5.4 Software verification

Since no documentation was found on the verification tests, the OOMAO platform was verified as well. All objects explained in Section 5.2 were verified with literature to check all the formulas and methods implemented. Moreover, separate tests were performed to check the effects of each object on the AO system for system verification purposes. These tests are listed in Table 5.9. The letters P/F stand for pass/fail.

Test **SW-2.1** can be visualised as shown in Figure 5.12, where a wavelength of 550 nm is used in Figure 5.12(a) and a wavelength of 1550 nm is used in Figure 5.12(b). The image retrieved by the camera is depicted. Here, it is seen that changing the source to a smaller wavelength while keeping all the other parameters the same results in a blurred image, and the airy disk pattern that is seen in Figure 5.12(b) is lost. Subsequently, testing **SW-4.3** resulted in the same images, but with more than 80 by 80 pixels.

Testing **SW-5.1** resulted in the plot seen in Figure 5.13. Here the residual error of the aberrations are plotted for different number of actuators against the error caused by aberrations when no control is implemented. As seen, the residual error decreases with increasing

Table 5.9: System verification of the AO system in OOMAO.

ID	Test	P/F
1	***Atmosphere***	
SW-1.1	Increasing the Fried parameter in the atmosphere class, should result in more aberrations, which is seen in the residual error of the corrected wavefront and the decrease of the Strehl ratio.	P
SW-1.2	Increasing the wind speed in the atmosphere class, should result in more aberrations, which is seen in the residual error of the corrected wavefront and the decrease of the Strehl ratio.	P
SW-1.3	Increasing the wind direction in the atmosphere class, should not result in more aberrations, which is seen in the residual error of the corrected wavefront and the decrease of the Strehl ratio.	P
2	***Source***	
SW-2.1	Choosing a smaller wavelength for the source of the science camera, should result in a more aberrated image thus, a lower Strehl ratio.	P
3	***Telescope***	
SW-3.1	Decreasing the diameter of the telescope object should result in to less aberrations, so a bigger Strehl ratio and a smaller residual error.	P
SW-3.2	Increasing the sampling time of the telescope object should result in less aberrations, so a bigger Strehl ratio and a smaller residual error.	P
4	***WFS***	
SW-4.1	The reconstructed slopes is equal to twice the number of lenslets.	
SW-4.2	Increasing the number of lenslets should result into more slopes.	
SW-4.3	Increasing the resolution should result into an image with more pixels.	P
5	***DM***	
SW-5.1	Increasing the number of actuators should result in a lower residual error.	P
SW-5.2	Increasing the actuator stroke should result in a lower residual error.	P
6	***Calibration***	
SW6.1	Increasing the actuator stroke should result in a better wavefront correction	P

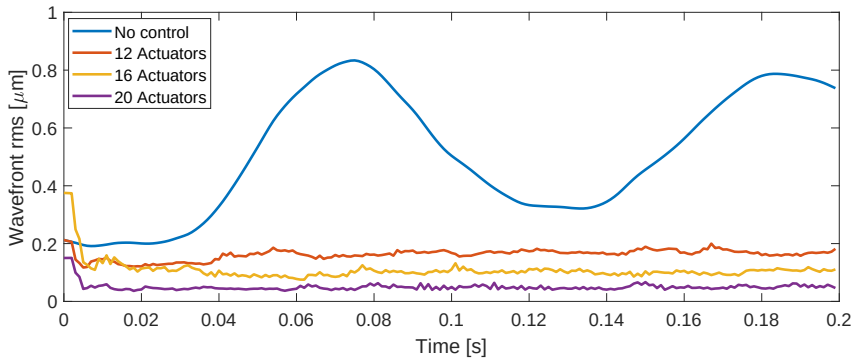

Figure 5.13: The effect of the number of actuators on the residual rms.

actuators. This means that a better correction can be achieved when a DM is used with more actuators, because a better correction accuracy can be achieved. A similar plot was created for **SW-5.2**, where the same could be seen, but for an increasing actuator stroke. Thus, a larger actuator stroke enables to correct better for the aberrations introduced.

CHAPTER

6 Calibration of test set-up

Once the experimental set-up has been installed in IAC's laboratories, the system has to be calibrated. This is a crucial step, as the incident wavefront should be as planar and parallel as possible to the plane of the lenslets, to assure each reference spot is centred behind the lens. The calibration process is explained in Section 6.1. Then, the process to retrieve the command matrix is described in Section 6.2. Finally, the sensitivity analysis performed for the experimental test set-up is discussed in Section 6.3.

6.1 Calibration process

The calibration process depends on many factors. Therefore, the set-up has been divided into three parts to explain the calibration steps, as seen in Figure 6.1. First, the laser part will be discussed, followed by the mirror part and relay part. Note that, during the calibration process, the atmospheric turbulence simulator is not used.

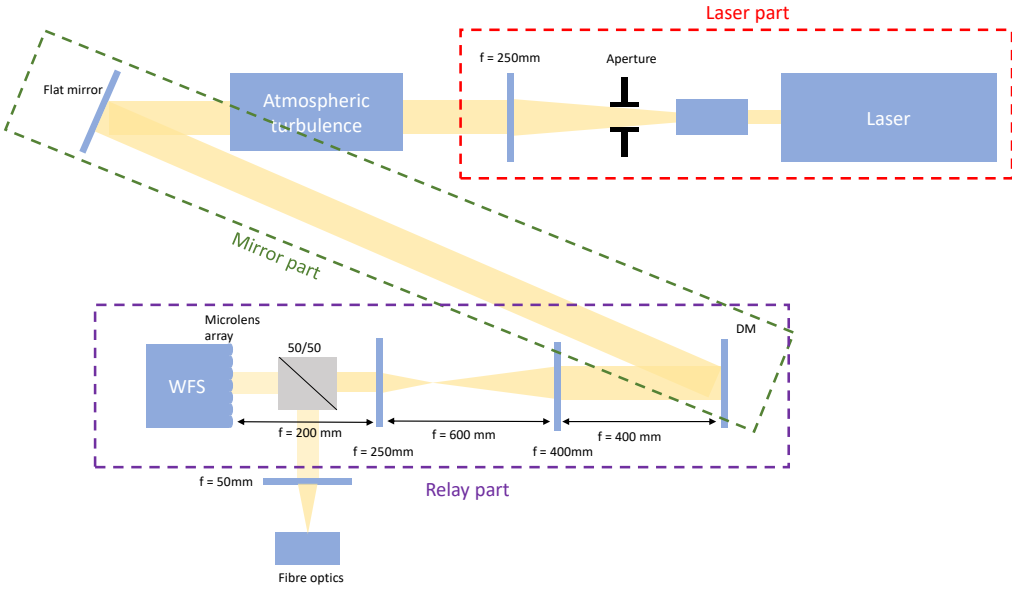

Figure 6.1: Set-up split in parts for the calibration process.

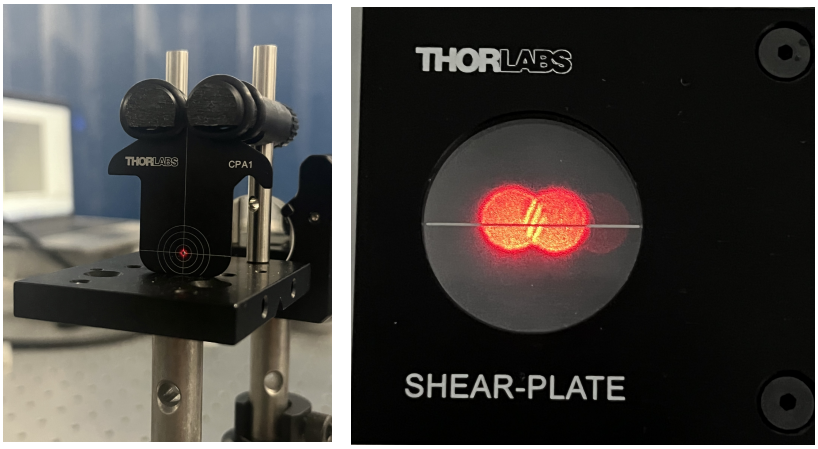

(a) Focaliser used to align the laser (b) Shear interferometer to check laser collimation

Figure 6.2: Calibration tools

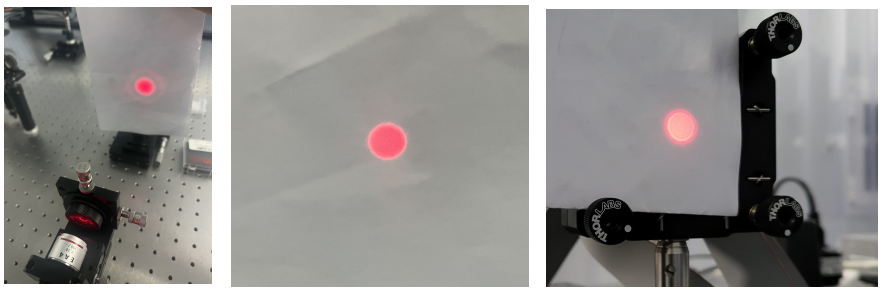

(a) Spatial filter (b) Amplified laser source (c) Laser source before arriving to the DM

Figure 6.3: Point source beam coming from the laser at different stages of the calibration process.

Calibration steps of the laser part

First, the laser had to be aligned properly. This was checked using a point of reference, called a focaliser, that is adjusted to the height of the laser at the beginning of the optical path. The laser should maintain the same height and direction along the entire optical path. Therefore, the focaliser is placed as far away as possible from the laser. If the laser then passes through the centre, as seen in Figure 6.2(a), the laser is properly aligned.

Moreover, the laser should uniformly illuminate the objects throughout the entire optical path. The laser source is expanded to spatially filter the centre, as seen in Figure 6.3(a). This results in a uniformly illuminated point source shown in Figure 6.3(b). This point source continues as such until it arrives at the DM, where airy disks seem to show up as seen in Figure 6.3(c). The reason why this phenomenon takes place remains to be unknown. Therefore, the effects will have to be taken into account in the final results.

Finally, it is crucial to verify whether the laser is collimated along the entire optical path. This can be checked using two methods. First, the point source should not diverge nor converge along the optical path, which can be checked by placing a white paper in front of the laser and varying its distance to the laser. Second, using a shear interferometer, the collimation of the laser can be fine tuned. The interferometer is placed after the collimation lens. The resulting image is given in Figure 6.2(b). As seen, the point source is split into lines.

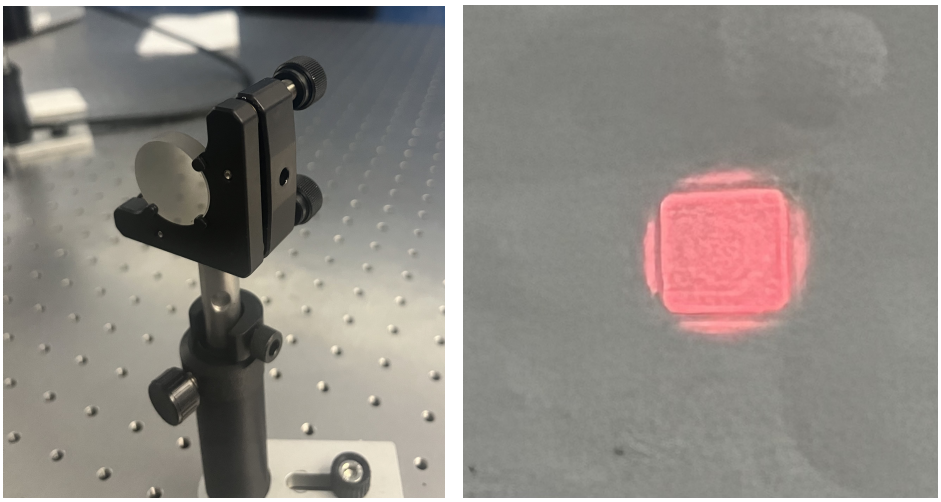

(a) Flat mirror on the optical mount (b) Illuminated surface of the DM

Figure 6.4: Calibration steps to calibrate the mirror part.

When these lines are horizontal and parallel to the black reference line in the middle, the point source is collimated.

Calibration of the mirror part

Once the laser is aligned and collimated, the source travels to the flat mirror, which then reflects the light to the DM. Again, the point source has to be aligned properly along the entire optical path. Note that the alignment of the optical path has to be performed with the smallest beam width, which is adjusted with an aperture placed on top of the f250 lens that collimates the laser. Therefore, the light source has to hit the middle of the mirror, which is visually checked by using a white paper. Then, the focaliser seen in Figure 6.2(a) that has the height of the optical path, is placed in front of the DM. The point source should pass exactly through this point. Therefore, the height of the mirror is adjusted using the pins on the optical mount of the mirror, shown in Figure 6.4(a). Finally, the light has to be centred into the DM, such that the entire DM structure is illuminated, as seen in Figure 6.4(b).

Calibration of the relay part

The final step is to calibrate the relay part. To do this, the calibration is split up into four phases:

1. Alignment of the system without relay and without the beam splitter
2. Alignment of the system with one lens of the relay and without the beam splitter
3. Alignment of the system with the entire relay and without the beam splitter
4. Alignment of the system with the entire relay and with the beam splitter

The calibration of the system without relay implies the alignment of the optical path from the DM to the WFS without both lenses in the middle. The focaliser seen in Figure 6.2(a) is used again to align the optical path. Moreover, the spotfield image from the WFS is retrieved to ensure the centering of the optical path seen in Figure 6.5(a).

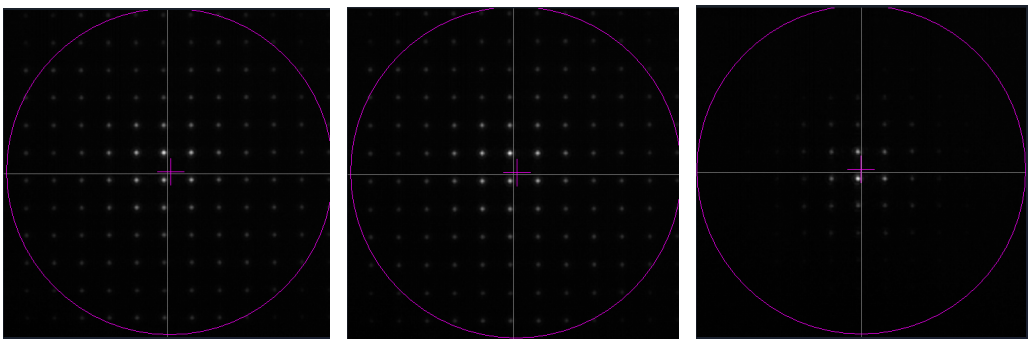

(a) Alignment without relay (b) Alignment with 1 lens (c) Alignment with 2 lenses

Figure 6.5: The spotfield images during the alignment process of the relay system.

Then, the same thing is performed, but for one lens only of the relay system, which should result in the spotfield seen in Figure 6.5(b).

Next, the entire relay system is calibrated, which gives the spotfield image depicted in Figure 6.5(c). The final alignment procedure was to align the entire relay system including the beam splitter, which should not affect the last spotfield image. Note that the alignment is carried out with the smallest beam width possible, which is why there are few spots in the spotfield images.

The second verification step that had to be carried out, is checking whether the optical path was still collimated after passing the relay system using the interferometer in Figure 6.2(b). To do this, the set-up was slightly adjusted as seen in Figure 6.6. This was done to exclude any effect the DM might have on the collimation process, as the mirror does not have an ideal smooth surface.

Furthermore, the actuator movement of the DM was verified. This was done using the GUI of Boston Micromachine described in Section 5.3, which allows to move the actuators one by one. The ideal result would follow if the system meets the Fried configuration, where each actuator is placed in the intersection of the microlens arrays as seen in Figure 5.6.

To obtain the Fried configuration, the relay is used to scale the actuator pitch to the microlens array pitch. The relay part was set-up, such that it followed the theory explained in Section 5.1. This resulted in the following actuator movement for an actuator stroke of 0.8 shown in Figure 6.7. As seen, the actuator movement results in a significantly big black hole, instead of the movement of the spots in the four surrounding lenslets. Strokes of 0.2, 0.4, and 0.5 were later tried. The only stroke that did not result in the image to be broken down, is a stroke of 0.2. However, this stroke value did not result in the movement of the spots in the four lenslets, but only reduced the intensity of the four surrounding spots.

To fix that, several distances of the relay to the DM and the WFS were tested. In Figure 6.8(a), the spotfield image for an actuator stroke of 0.8 is shown when the relay is placed 2.5 cm closer to de DM, equal to a distance of 375 mm. As seen, the stroke remains too strong and still creates a black hole in the image, this time smaller than at a distance of 400 mm. The relay was then placed 2.5 cm closer than before, making the distance between the DM and the relay now 350 mm. The corresponding spotfield image is depicted in Figure 6.8(b). An important feature is that the black hole seems to have disappeared. The last set-up included placing the relay at a distance of 325 mm to the DM, and its spotfield image is shown in Figure 6.8(c). When moving the actuators at this distance, the spots in the spot field image result to be broken down into rings surrounding them, which is a feature when the image is distorted or coma is present. Therefore, a final distance of 350 mm to the relay was chosen as

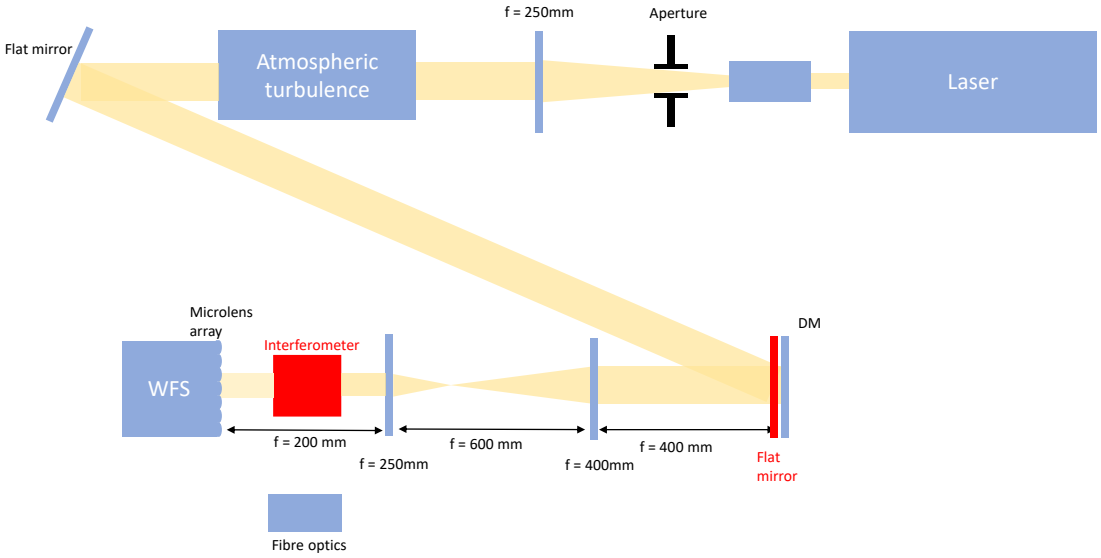

Figure 6.6: set-up to check the collimation of the relay system.

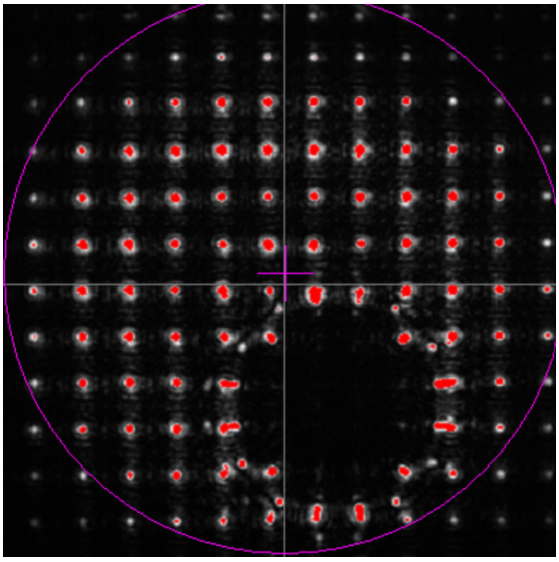

Figure 6.7: Actuation results with DM and WFS placed in pupil when the actuator stroke equals 0.8.

final configuration to proceed with the command-matrix reconstruction. After adjusting the distance of the relay to the DM, the calibration image is taken, which is seen in Figure 6.9(a). Using image processing, the centroids for the spots in the spotfield image are calculated and plotted on top of the image to check whether the location of the centroids matches the location of the spots in Figure 6.9(b).

Then, a check was performed to verify whether the centroids slightly moved compared to the calibration centroids when an aberration was introduced. Plotting the new centroids on top of the calibration centroids is shown in Figure 6.10(a). As seen, there is not much difference between the centroids, which corresponds to what is expected as the slopes induce an extremely small change. Moreover, the calibration centroids were compared to an ideal equidistant 12x12 grid, which is plotted in Figure 6.10(b). As seen, the distance between the calibration centroids seems to be smaller than the pitch of the ideal grid in both the horizontal and vertical direction. Moreover, the distance between the centroids seem to

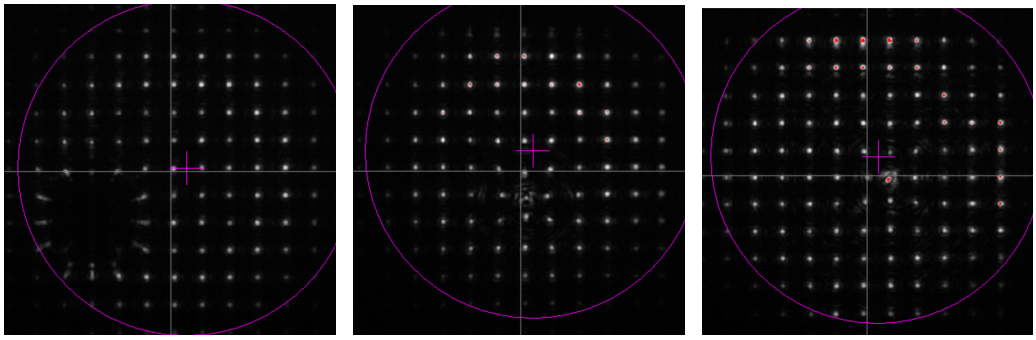

(a) Actuator movement for relay at d=375 mm to the DM (b) Actuator movement for relay at d=350 mm to the DM (c) Actuator movement for relay at d=325 mm to the DM

Figure 6.8: The spotfield images when actuator 74 is moved with a stroke of 0.8 at different distances between the relay and the DM.

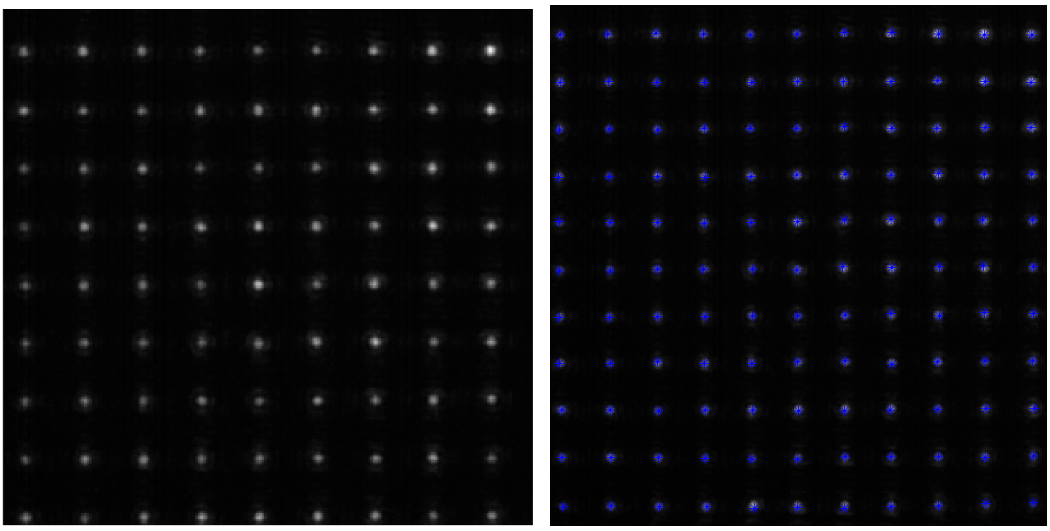

(a) Calibration image (b) Calibration image with centroids

Figure 6.9: Retrieved spotfield image for the calibration used to calculate the reference centroids.

decrease to the edges of the image, which is a feature when the image is negatively distorted (barrel shape). This can be solved by adjusting the distance between the relay and the DM. However, this is precision work and requires a relay specially manufactured for this particular DM and WFS. Thus, it was decided to continue with this calibration configuration.

Summary of verification tests of the set-up

A summary of all the tests that were performed to check whether all HW components worked as expected is given in Table 6.1. Here, all the separate tests per components, deemed relevant for the calibration, but also for the rest of the set-up, are listed along with the extra tools or specific method required to perform the tests. Note that these tests also include the tests performed using the given GUIs described in Chapter 5. Again, P/F stands for pass/fail.

As seen, verification test **HW-2.2** did get a fail. This is because the flat mode provided by the manufacturer did not results in a flat surface for the mirror. Instead, all actuators with a stroke set to zero resulted in the flattest wavefront image. Thus the zero mode was used

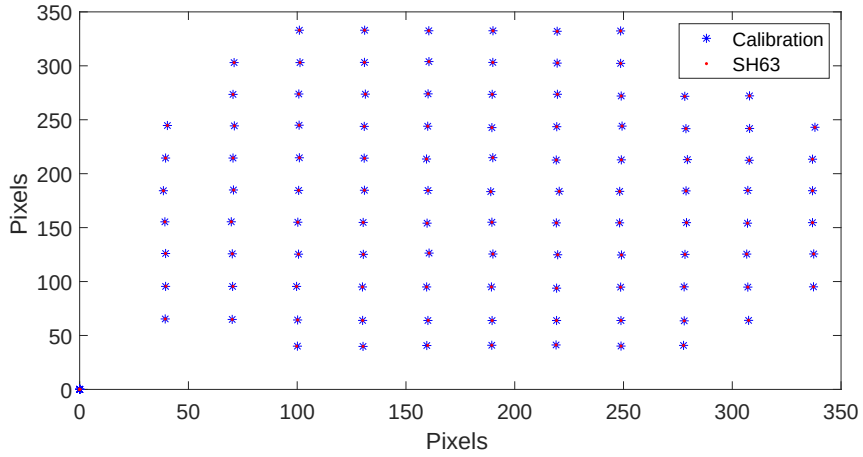

(a) Aberration centroids compared to calibration centroids

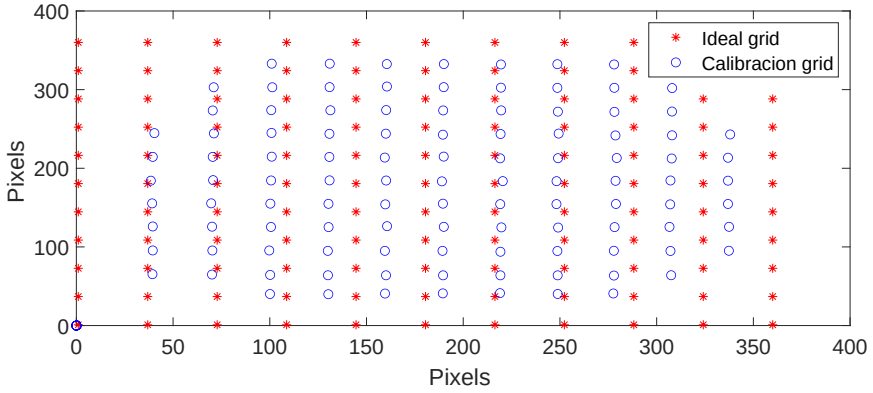

(b) Calibration centroids compared to an ideal grid.

Figure 6.10: Verification steps for the calibration centroids.

during the calibration process. Moreover, test **HW-4.2** was deemed a fail, because only 5% of the maximum polarised light was retrieved with the MMF. This was due to a small accident that happened in a previous experimental set-up by colleagues at IAC that used the same MMF, where the MMF cable got damaged (burned). Nevertheless, since it is a ratio between the initial and post CL simulation results of retrieved light, it should not affect the study of the controller performance.

Table 6.1: Verification tests of set-up

ID	Test	Tools/Method	P/F
1. Laser Part			
HW-1.1	The power of the laser is equal to 4 mW.	SW enables to check the power.	P
HW-1.2	The laser intensity should be illuminated uniformly after passing the spatial filter.	Visually check with a piece of paper that reflects laser.	P

Table 6.1: Verification tests of set-up

ID	Test	Tools/Method	P/F
HW-1.3	The laser should be collimated after passing the f250 lens.	Use a shear interferometer and visually check if the beam lines are aligned with the reference line.	P
HW-1.4	The laser should be aligned with the rest of the components in its optical path.	A focaliser is placed in front of the laser and then at the end of the table. The laser should pass both times through the centre. If not, it is not aligned.	P
2. Mirror Part			
HW-2.1	The actuators should move when a stroke is given.	The stroke input is given using the GUI of the DM. When the stroke is changed, an intensity difference of light should occur where the actuator is moved with a stroke value, which can be visually checked with piece of paper.	P
HW-2.2	The DM should reflect the light uniformly when the flat mode is introduced.	Input flat mode file in GUI and check visually with a piece of paper if the light is equally reflected.	F
HW-2.3	The actuators should induce a surface deflection when moved.	Visually check if the surface membrane induces a 'peak' where the actuator is moved.	P

Table 6.1: Verification tests of set-up

ID	Test	Tools/Method	P/F
HW-2.4	The DM should be aligned with its optical path.	A focaliser is placed in front of the DM and then at the end of the table. The laser should pass both times through the centre. If not, it is not aligned.	P
3. Relay Part			
HW-3.1	The spots should be illuminated uniformly	Check the spotfield visually obtained from the GUI.	P
HW-3.2	The alignment should be centred with no relay present.	Check the spotfield visually obtained from the GUI.	P
HW-3.3	The alignment should be centred with one lens of the relay.	Check the spotfield visually obtained from the GUI.	P
HW-3.4	The alignment should be centred with two lenses of the relay.	Check the spotfield visually obtained from the GUI.	P
HW-3.5	The light source should be collimated after passing the relay.	Use a shear interferometer and visually check if the beam lines are aligned with the reference line.	P
HW-3.6	The WFS measurements should not become saturated.	Check the spotfield visually obtained from the GUI. Adjust the exposure time.	P
HW-3.7	The WFS, including the lens and camera, should be aligned with its optical path.	A focaliser is placed in front of the WFS and then at the end of the table. The laser should pass both times through the centre.	P
4. Fibre Optics Coupling			

Table 6.1: Verification tests of set-up

ID	Test	Tools/Method	P/F
HW-4.1	The MMF should be aligned with its optical path.	A focaliser is placed in front of the MMF and then at the end of the table. The laser should pass both times through the centre.	P
HW-4.2	The MMF, should measure at least 10% of the maximum polarised light.	A power and energy meter is coupled to the MMF and the power is measured. This should equal 10% of the measured light by the polarimeter.	F

6.2 Command matrix

After the calibration has been performed, the command matrix can be computed. To do this, two methods will be used. First, Thorlabs' GUI offers to reconstruct the command matrix by automatically moving the actuators one by one with an actuator stroke of 0.8. The centroids' new position are saved in a file for each actuator movement, along with the induced aberrations, and the actuator voltages. Moreover, the program allows to import the reference centroids used. Finally, the GUI computes the pseudo inverse of the interaction matrix, which is the command matrix. This is a $n \times 2m$ matrix with n being the actuators and m being the number of lenslets in the microlens array. The command matrix is depicted in Figure 6.11. As seen, the GUI seems to not compute the command matrix correctly when compared to the command matrix from the simulations shown in Figure 5.7(b). Four clear slopes in the positive and negative direction, marked in green and blue, respectively, should be seen, which correspond to the displacement of the four spots when each actuator is moved. Instead, separate slopes are plotted for an interval of 20 actuators, each consisting of discretised "steps". This would mean that the spots of the same lenslets would move every time an actuator is moved, and only for one out of every twenty actuators. Thus, in between, no spot displacements would occur, which is not what should happen if the system follows a configuration similar to the Fried configuration. Moreover, there should be a clear separation between the slope displacement in the x-direction and the y-direction, which is not present.

The second method is to reconstruct the interaction matrix first by using the Application Programming Interface (API) and Thorlabs and Boston Micromachines with Matlab. This code saves the spotfield image each time a new actuator is moved with a predefined stroke value. Thus, a total of 140 images will be saved, as the four actuators in the corner are assumed to not function by the GUI itself. Then, using image processing, the retrieved spots in the spotfield image are dilated and eroded to increase the contrast between the intensity of

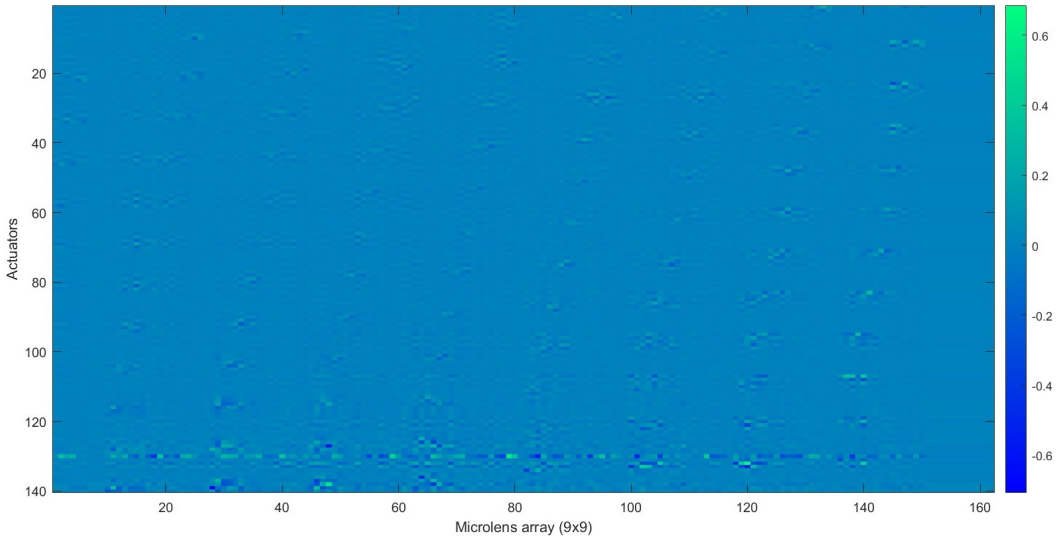

Figure 6.11: Command matrix retrieved from Thorlabs' GUI.

the spots and its background. The centroids for this new image are then computed for each of the 140 images. An example for actuator 80 is given. The original image is seen in Figure 6.12(a). First, the image is dilated, which amplifies the size of the spots by adding pixels of white colour to its surrounding, as seen in Figure 6.12(b). To avoid these white spots from merging with each other, the system is erroded, which removes some of the pixels with white colour to separate the spots properly, as shown in Figure 6.12(c). Finally, the centroids for these image regions are calculated and plotted in Figure 6.12(d).

However, for a stroke actuation of 0.8, these image regions are sometimes miscalculated, as seen in Figure 6.13, due to the actuator stroke being too strong and creating aberrations to the surrounding of the spot displacement. Therefore, a stroke actuation of 0.5 will be used for the calibration process. Nevertheless, some actuators still cause an erroneous centroid. Thus, all the images were checked and, if such an incorrect centroid was detected, it was taken out by hand.

Next, the centroids are sorted such that it follows the order from the lenslets in the array going from the top row to the bottom row, and from left to right. After retrieving all the centroids, a $2m$ interaction matrix can be constructed with m lenslets and n actuators. Here, the x- and y-coordinate for the slope in each lenslet is placed beneath each other for each of the 140 actuators, which is depicted in Figure 6.14. As seen, the slopes are not completely clean. That is because, during the calibration process, the system is not an ideal system anymore as in the simulations in OOMAO. Instead, measurement errors are present, causing outliers. This results in the horizontal lines seen in the image, and the vertical line for actuator 46. Finally, using the singular value decomposition method, the command matrix is computed from the interaction matrix. The corresponding eigen values and chosen threshold for the singular value decomposition method is depicted in Figure 6.15, along with the command matrix in Figure 6.16. From Figure 6.15, it is seen that the eigenvalues larger than 12 are not included. This is done to avoid the influence of outliers when computing the command matrix. These outliers are what causes the horizontal lines in the interaction matrix shown in Figure 6.14, which are not so clear anymore when depicting the command matrix in Figure 6.16. These outliers are paired with high eigen values. Again, Figure 6.16 shows the four slopes paired with the movement of the spots in the four surrounding lenslets every time an actuator is moved. Furthermore, the clear separation between the movements in the x-

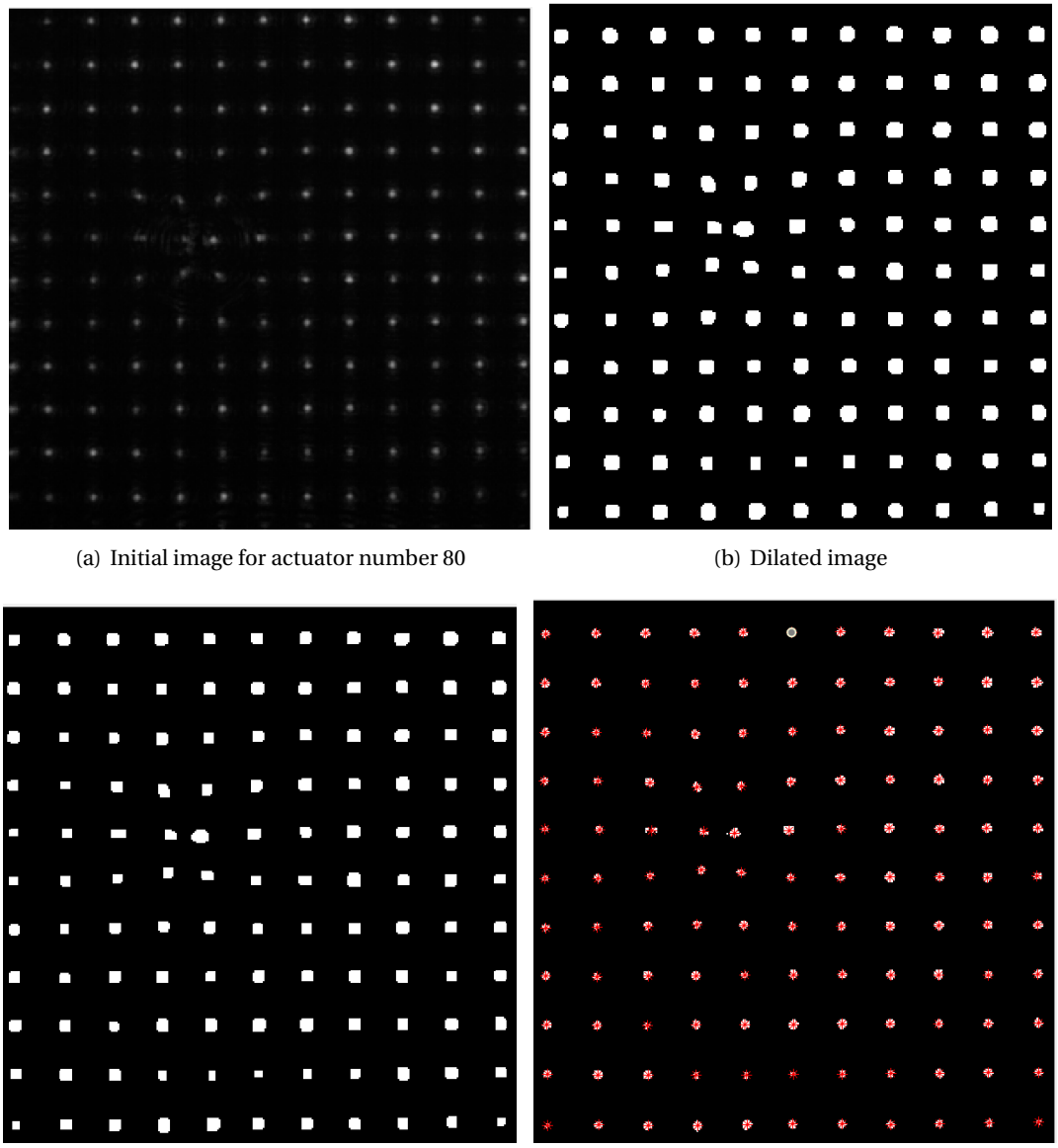

(a) Initial image for actuator number 80

(b) Dilated image

(c) Eroded image

(d) Centroids for the processed image

Figure 6.12: Image processing steps to reconstruct the command matrix.

direction and the y-direction is seen.

As a check, the slopes for one actuator movement, actuator 74, are compared to the slopes simulated in OOMAO to see whether it shows the same behaviour. The slopes for actuator 74 retrieved from OOMAO are plotted in Figure 6.17(a) together with the overlap of the x- and y-coordinates Figure 6.17(b). The same is plotted for actuator 74 from the interaction matrix reconstruction through image processing in Figures 6.18(a) and 6.18(b), respectively. As seen, the slopes for OOMAO show slope values in only a specific amount of lenslets of the microlens array, which is correct, as only the spots in the surrounding four lenslets of the actuator should move. Hence, the four peak in the x-direction and in the y-direction. Moreover, the x- and y-coordinates overlap, meaning there is a consistency of spot deviations in both directions. Note that this an ideal case where the reference points equal zero, the system meets the Fried configuration, and no measurement noise are present.

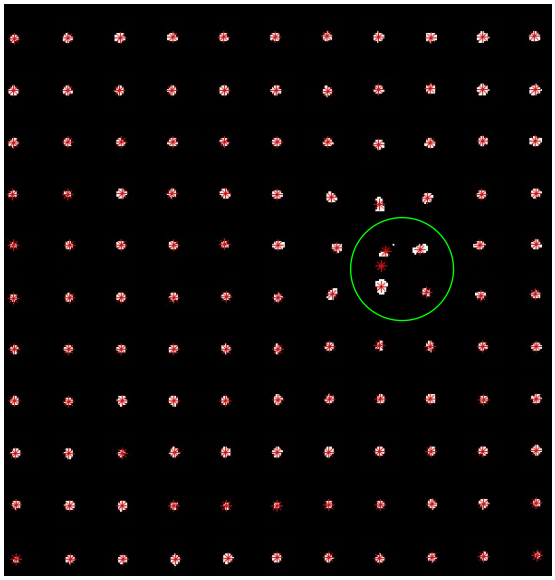

Figure 6.13: Erroneous centroid retrieval from image processing for an actuator stroke of 0.8.

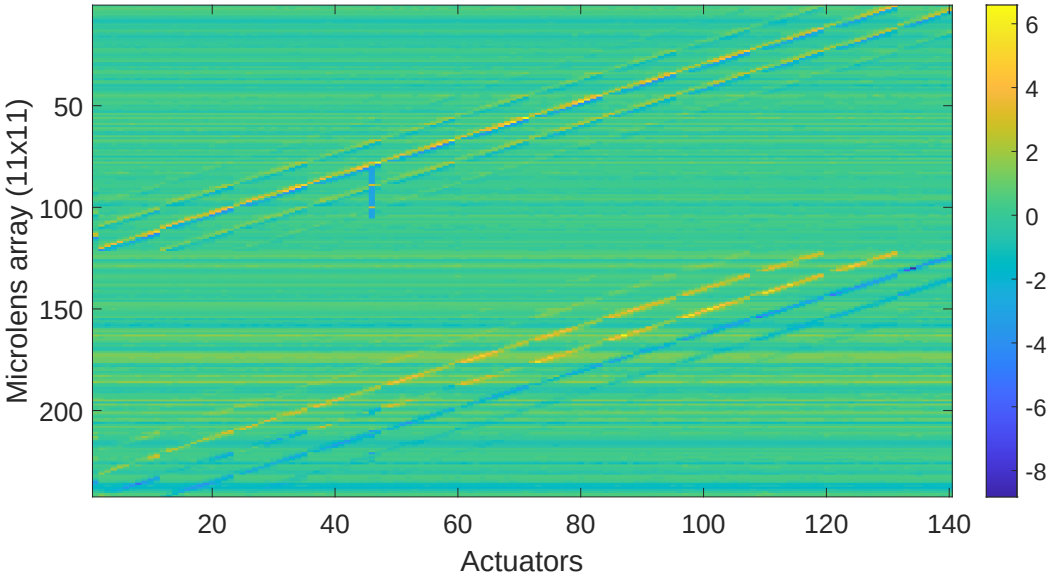

Figure 6.14: Interaction matrix through image processing

On the other hand, the slopes retrieved during the reconstruction of the interaction matrix in the lab show different results. There seem to be much more noise when retrieving the slopes, hence, the large number of spikes. This is believed to be due to the fact that the HW components are not manufactured to be used together in one system. Thus, alignment errors as well as measurement errors can cause this phenomenon, causing the system to not follow the Fried configuration exactly. Nevertheless, the x- and y-coordinates do overlap meaning that each spot movement in the x-direction is paired with a movement in the y-direction. The most extreme movements are due to the actuator movements, which stand out from the displacements caused by noise. Another difference is the magnitude of the slopes computed in OOMAO and during the image reconstruction process. OOMAO shows to have slopes in the order of 10^6. This is simply due to the application of a scaling factor,

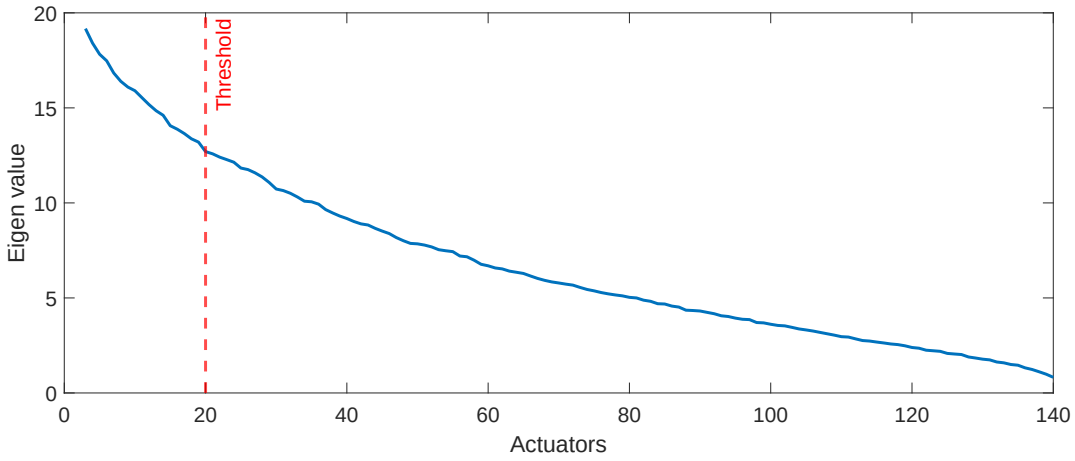

Figure 6.15: Eigen values of the interaction matrix computation through image processing.

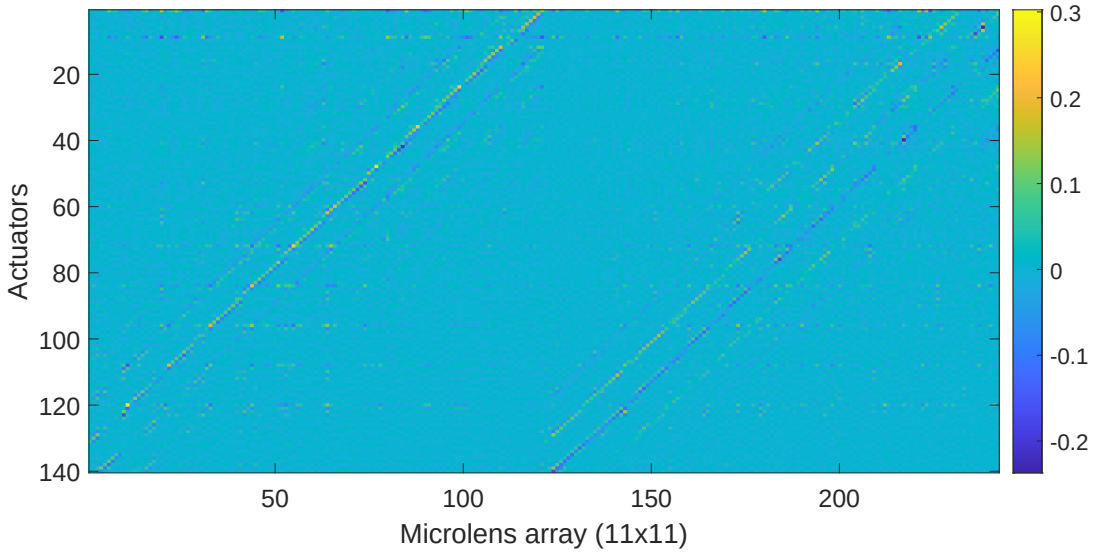

Figure 6.16: Command matrix through image processing.

which is required when an actual telescope is used. Since no telescope was used in the experimental set-up, the scaling factor was not necessary.

The same checks were performed for the closed-loop system verification, where an aberration was introduced with the atmospheric turbulence simulator. Once the loop was closed and the controller sent the actuator commands to the DM, the slopes and coefficients were checked as explained above. The same observations were made.

6.3 Summary of sensitivity analysis during the calibration process

To conclude this chapter, a summary of steps performed for the sensitivity analysis of the experimental set-up is given in Table 6.2. Here, the change in the behaviour of the system when replacing certain HW components as well as changing distances has been evaluated. As seen, the types of tests performed were divided between the components. For each test, the exact change has been stated (left-hand side) along with the observations made for each change (right-hand side). The observations were used to chose the final set-up.

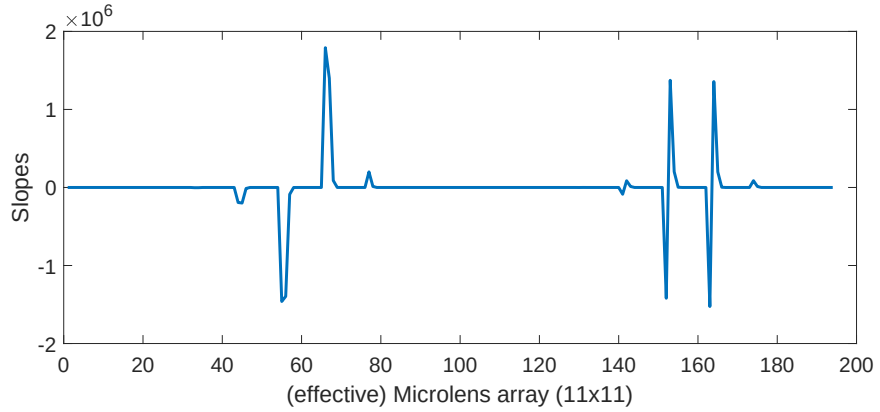

(a) Slopes for actuator 74 retrieved from OOMAO

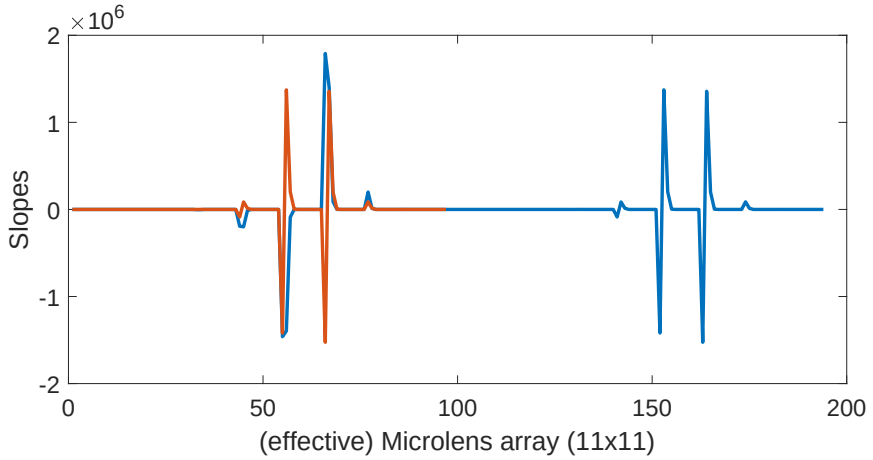

(b) Overlap of x- and y- coordinates for actuator 74 retrieved from OOMAO

Figure 6.17: Slope verification OOMAO

Table 6.2: Sensitivity tests performed throughout the calibration process.

Sensitivity test	**Observations**
Laser	
Two different lasers were used to observe properties of the light source for the same wavelength, e.i. The light intensity, the (uniform) illumination: - Omicron LDM633 150/150 -Thorlabs LDM633	Thorlabs LDM 633 results in a cleaner light source, and is more uniformly distributed.
Several amplifiers were used: - 40x amplifier with a 6 micron aperture -10x amplifier with an 8 micron aperture - 4x amplifier with a 10 micron aperture	The relation of a smaller amplifier and a larger aperture results in a better spatial filter for the laser.

Table 6.2: Sensitivity tests performed throughout the calibration process.

Sensitivity test	**Observations**
Several collimation lenses were used: -f75 -f150 -f250	The smaller the focal length, the smaller the collimated light source. The ideal light source should have a beam width smaller than the DM aperture, but large enough to illuminate the entire surface of the DM. Therefore, the lens of f250 was chosen.
Relay	
The distances from the DM to the relay were studied: -400 mm from the DM -375 mm from the DM -350 mm from the DM -325 mm from the DM	At 400 mm and 375 mm, the spotfield deviation did not show the right behaviour. Instead, the image is broken down and black holes appear, even when the actuator stroke is reduced. At 350 mm, it does work as expected. At 325 mm, the spots are splitted into two parts when an actuator stroke is introduced.
The distances from the WFS to the relay were studied: -125 mm from the DM -150 mm from the DM -175 mm from the DM -200 mm from the DM	At 125 mm and 150 mm,the spotfield deviation did not show the right behaviour. Instead, the image is broken down and black holes appear, even when the actuator stroke is reduced. At 170 mm, it does work as expected. At 200 mm, the spots are split into two parts when an actuator stroke is introduced.
WFS	
Several image sizes, corresponding to different microlens arrays, were tried: -1080x1080 px - 35x35 array -768x768 px - 23x23 array -512x512 px - 15x15 array -360x360 px - 11x11 array	The spot deviations are best seen for an image size of 360x360 px, corresponding to an 11x11 microlens array. This is as expected, as the Fried parameter requires an (n-1)x(n-1) microlens array, n being the number of actuators.
DM	
The actuator stroke is varied: -0.1 -0.5 -0.8 Note that, this can only be done when reconstructing the interaction matrix through image processing as, Thorlabs' GUI does not allow to change the actuator stroke when performing the calibration process.	A stroke of 0.1 is paired with really small spot deviations, almost indistinguishable from the calibration centroids. A stroke of 0.5 is best when retrieving the spots from the spotfield images through image processing. A stroke of 0.8 induces small aberrations around the deviated spots, which causes errors when the centroids are computed, because these aberrations are mistaken for spots.

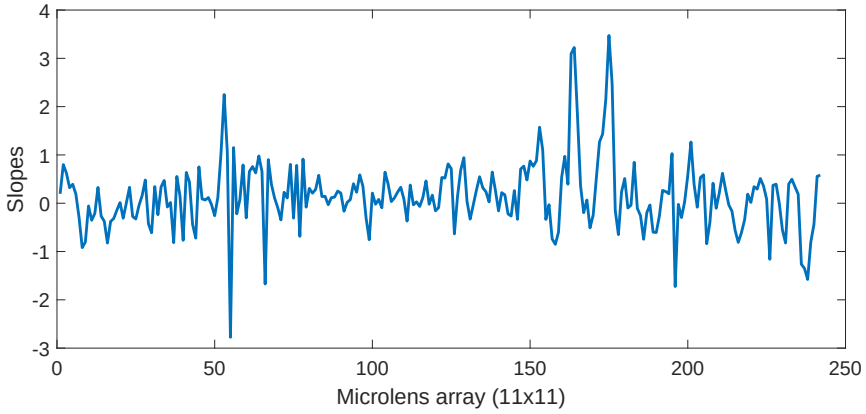

(a) Slopes for actuator 74 retrieved from IM reconstruction.

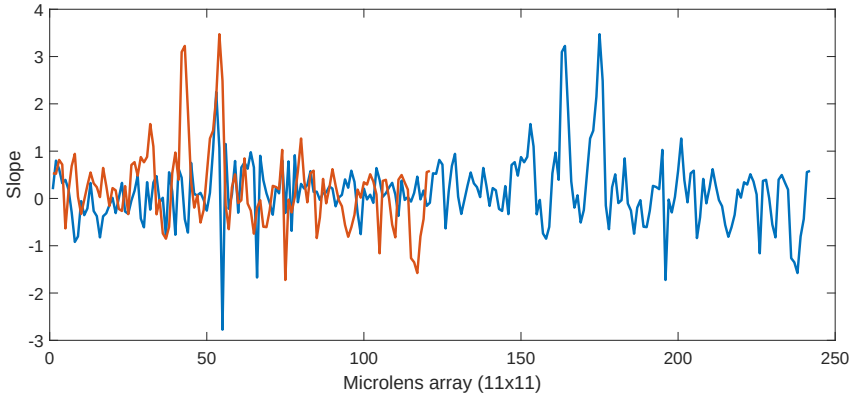

(b) Overlap of x- and y- coordinates for actuator 74 retrieved from IM reconstruction

Figure 6.18: Slope verification for IM reconstruction

CHAPTER

7 Controller design

In this chapter, the controller algorithms considered for the AO system will be discussed. Section 7.1 describes the current controller type used in the AO simulations, which is applied by IAC. Then, Section 7.2 will address the algorithms for a linear PID-controller and a non-linear INDI-controller considered to increase the AO system performance. Additionally, the gains of the designed controllers are tuned and defined in Section 7.3. Next, the frequency analysis method applied to study the behaviour of the controllers at a later stage is explained in Section 7.4. Moreover, the sensitivity analysis results for the initial I-controller and the PID-controller are compared in section 7.5, along with the optimisation method used to achieve a better performance of the AO system with the PID-controller. The post processing of the retrieved data from the robust design is stated in Section 7.7. Subsequently, the sensitivity analysis performed on the INDI-controller is given in Section 7.6, where the controller is compared to the PID-controller. Finally, the verification tests carried out on the controllers are stated in Section 7.8.

7.1 Baseline I-controller

The current system makes use of an integral (I) controller that follows the Backward Euler method derived as follows [12]:

$$u(t) = K_i \int e(t)\,dt \tag{7.1}$$

where $u(t)$ is the control output, K_i is the integrator gain, t is the time and $e(t)$ is the error. Taking the derivative of Equation (7.1) results in

$$\dot{u} = K_i e(t)$$

Now, discretising this step gives:

$$\frac{u(k) - u(k-1)}{T} = K_i e(k)$$

where k is the step in time, T is the sampling time, $u(k-1)$ is the controller output one step in the past, $u(k)$ is the current controller output, and $e(k)$ is the current error. Isolating $u(k)$ results in the used controller:

$$u(k) = K_i e(k)\,T + u(k-1) \tag{7.2}$$

[12] https://math.libretexts.org/Bookshelves/Differential_Equations/Numerically_Solving_Ordinary_Differential_Equations_(Brorson)/01%3A_Chapters/1.03%3A_Backward_Euler_method, retrieved on 25-02-2023

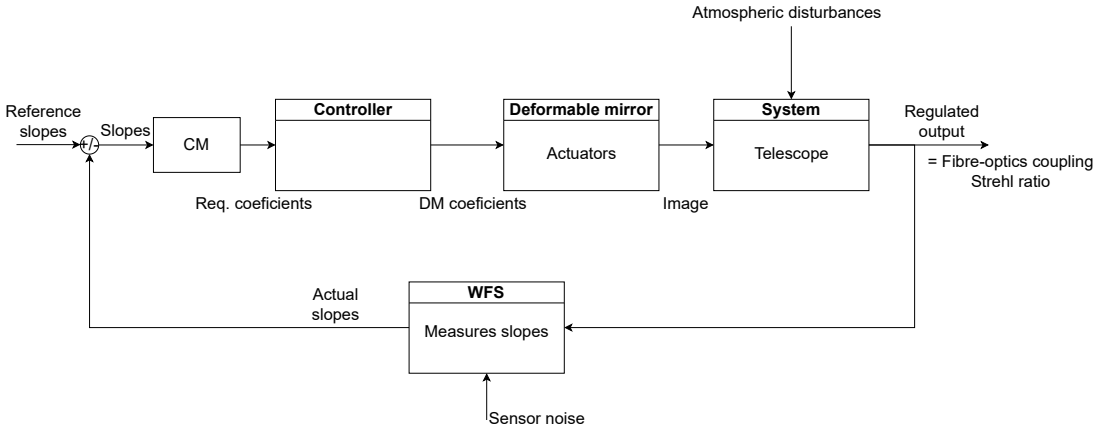

Figure 7.1: SW architecture for the controller when implemented in the AO system.

Applied to this specific problem, the output, $u(k)$, refers to the new actuator commands $\mathbf{c}$ computed to be sent to the deformable mirror, which is an $m \times 1$ vector with m being the number of actuators in the DM. The error of the system, $e(t)$, is the difference between the actual wavefront-aberration slopes measured by the WFS, $\mathbf{S}$ and the reference slopes, which are set to be equal to zero since that is the ideal case when no aberrations occur. In other words, the measured wavefront slopes are the errors and are defined as follows:

$$\mathbf{S} = \frac{\mathbf{S}_y}{\mathbf{S}_x} \tag{7.3}$$

However, before the slopes enter the controller, they are first multiplied by the Command Matrix (**CM**) to transform the slopes into commands, $\mathbf{c}$, that are the eventual outputs of the system. Thus, rewriting Equation (7.2) with these parameters gives:

$$\mathbf{c(k)} = \mathbf{K_i} \cdot T \cdot (\mathbf{CM} \cdot \mathbf{S})(\mathbf{k}) + \mathbf{c(k-1)} \tag{7.4}$$

7.2 Improved controller design

Two different controllers were designed and evaluated. First, the use of a simple PID-controller was considered. However, to opt for a more robust design, an INDI will be considered if enough time is left. The SW architecture of the control loop considered is again depicted in Figure 7.1.

PID-controller

The first controller that will be designed will be a PID-controller. The controller follows the form:

$$u(t) = K_p e(t) + K_i \int e(t)\,dt + K_d \frac{de(t)}{dt} \tag{7.5}$$

where K_p is the proportional gain, K_d is the derivative gain and all the other parameters are the same as for the I-controller explained above.

Note that Equation (7.5) refers to a continuous PID control. When applied, the formula requires to be discretised. To do this, the Backwards Euler method will again be used, where the derivative of the error is written as [12]:

$$\frac{de(t)}{dt} = \dot{e}(t) \approx \frac{e(k) - e(k-1)}{T} \tag{7.6}$$

where T refers to the sampling time.

To approach the definite integral of a function, it can be represented as the area of the region bounded by its graph of the given function between two points in the line, meaning:

$$\int e(t)dt = \sum e(t)\Delta t = (e(k) + e(k-1))\,T \tag{7.7}$$

Substituting Equation (7.6) for the derivative term, and Equation (7.7) for the integral term into Equation (7.5) gives:

$$u(k) = K_p e(k) + K_i\,(e(k) + e(k-1))\,T + K_d \frac{e(k) - e(k-1)}{T} \tag{7.8}$$

Rewriting Equation (7.8) for this specific application as done for the I-controller above, gives the final controller equation:

$$\mathbf{c(k)} = \mathbf{K_p}(\mathbf{S}\cdot\mathbf{CM})(\mathbf{k}) + \mathbf{K_i}((\mathbf{S}\cdot\mathbf{CM})(\mathbf{k}) + (\mathbf{S}\cdot\mathbf{CM})(\mathbf{k-1}))\,T + \mathbf{K_d}\frac{((\mathbf{S}\cdot\mathbf{CM})(\mathbf{k}) - (\mathbf{S}\cdot\mathbf{CM})(\mathbf{k-1}))}{T} \tag{7.9}$$

INDI

The Incremental Nonlinear Dynamic Inversion (INDI) method, is a method that reduces the uncertainties included in the NDI principle by decreasing its dependency on the onboard model, using either an actuator output or acceleration measurement feedback. This model has the advantage that it is inherently implicit, meaning that the desired closed-loop dynamics do not depend anymore on some explicit model to be pursued, but result when the feedback loops are closed. Thus, this model allows for a more robust system, while reducing the model uncertainties that would otherwise emerge from a conventional NDI-based controller. This controller might be an extremely useful option for the AO system if the results show that a PID-controller does not fulfill the requirements or a more robust is desired. But more important, this controller might be ideal for the system, because the deformable mirror does not have a model of its dynamics since, the mirror is represented as a linear Multi-Input-Multi-Output (MIMO) object. Thus, no states can be retrieved from the system.

Thus, system does not follow a state tracker as there are no states that represent the system dynamics. Instead, it follows an output tracking that remains constant, which refers to the reference slopes being zero. Therefore, the INDI will be modelled using the steps explained by Mooij (2023).

The fundamental concept of INDI is formulated as follows. Let us assume a non-linear system. Its system equations of motion can be described as:

$$\dot{\mathbf{x}} = \mathbf{f(x)} + \mathbf{G(x)u} \tag{7.10}$$

where $\mathbf{f(x)}$ represents the system dynamics, $\mathbf{G(x)}$ is the state-dependent control matrix of dimension $n \times m$, and $\mathbf{u}$ is the $m \times 1$ control vector. To get the approximated dynamics in its incremental form, the first-order Taylor-series expansion of $\dot{\mathbf{x}}$, evaluated around $[\mathbf{x_0}, \mathbf{u_0}]$ is

$$\dot{\mathbf{x}} = \dot{\mathbf{x}}_\mathbf{0} + \underbrace{\frac{\partial}{\partial \mathbf{x}}[\mathbf{f(x)} + \mathbf{G(x)u}]\Big|_{\substack{\mathbf{x}=\mathbf{x_0}\\ \mathbf{u}=\mathbf{u_0}}}}_{\mathbf{F(x_0,u_0)=F_0}}(\mathbf{x}-\mathbf{x_0}) + \underbrace{\frac{\partial}{\partial \mathbf{u}}[\mathbf{G(x)u}]_{\substack{\mathbf{x}=\mathbf{x_0}\\ \mathbf{u}=\mathbf{u_0}}}}_{\mathbf{G(x_0)=G_0}}(\mathbf{u}-\mathbf{u_0}) \tag{7.11}$$

For a sufficiently fast control update, related to a small time increment, $\mathbf{x}$ approaches $\mathbf{x_0}$, so $\mathbf{F_0}\,(\mathbf{x}-\mathbf{x_0}) << \mathbf{G}_0\,(\mathbf{u}-\mathbf{u}_0)$. This means this term can be ignored. The linearised system $\boldsymbol{\nu} = \dot{\mathbf{x}}$ is rewritten as

$$\nu = \dot{\mathbf{x}}_0 + \mathbf{G}_0\delta\mathbf{u} \tag{7.12}$$

where the control increment $\delta\mathbf{u} = \mathbf{u} - \mathbf{u_0}$ has been introduced. This increment is obtained by inverting Eq. (7.12), and is to be added to the nominal (or reference) control $\mathbf{u_0}$ to obtain the control $\mathbf{u}$, input to the non-linear system. So

$$\mathbf{u} = \mathbf{u}_0 + \delta\mathbf{u} = \mathbf{u}_0 + \mathbf{G}_0^{-1}\left[\boldsymbol{\nu} - \dot{\mathbf{x}}_\mathbf{0}\right] \tag{7.13}$$

In this case, the reference slopes are tracked. However, these slopes remain constant meaning $\dot{\mathbf{S}} = 0$ and the control is given by $\Delta\mathbf{c}$.

As explained before, the tracking is based on a constant zero reference value for the slopes. Thus, Equation (7.12) can be rewritten, as explained by Mooij (2023). such that the law is not incremental anymore, but a form of non-linear dynamics inversion:

$$\boldsymbol{\nu} = \mathbf{B}^* \delta\mathbf{u} \tag{7.14}$$

where $\mathbf{B}^*$ is a state-independent control matrix.

The control-law will be designed based on outer-loop control of the slopes, $\Delta\mathbf{y} = \mathbf{S_{ref}} - \mathbf{S} = 0 - \mathbf{S} = -\mathbf{S}$, and an inner loop of its first derivative, $\Delta\dot{\mathbf{y}} = -\dot{\mathbf{S}}$. So for the outer loop:

$$\mathbf{y_{out}} = \Delta\mathbf{y} = -\mathbf{S} \tag{7.15}$$

with the generic formulation for its derivative is given by

$$\dot{\mathbf{y}}_\mathbf{out} = \boldsymbol{\nu}_{\boldsymbol{out}} = \Delta\dot{\mathbf{y}} = -\dot{\mathbf{S}} \tag{7.16}$$

The desired slope rates, $\dot{\mathbf{S}}_\mathbf{des}$ are obtained from the equation above with:

$$\dot{\mathbf{S}}_\mathbf{des} = \boldsymbol{\nu}_{\boldsymbol{out}} + \dot{\mathbf{S}} \tag{7.17}$$

with

$$\begin{aligned} \boldsymbol{\nu}_{\boldsymbol{out}} &= \mathbf{K}_{\mathbf{p,out}}\Delta\mathbf{y} + \mathbf{K}_{\mathbf{i,out}}\Delta\mathbf{y}\cdot t \\ \boldsymbol{\nu}_{\boldsymbol{out}} &= -\mathbf{K}_{\mathbf{p,out}}\mathbf{S} - \mathbf{K}_{\mathbf{i,out}}\mathbf{S}\cdot T \end{aligned} \tag{7.18}$$

which may be obtained from a simple PI(D) control law. In the current application, a PI-control is taken.

To design the inner-loop control, the inner-loop vector is defined as:

$$\mathbf{y_{in}} = \Delta\dot{\mathbf{y}} = -\dot{\mathbf{S}} \tag{7.19}$$

with its derivative $\Delta\ddot{\mathbf{y}}$, referring to the slope acceleration, assumed to be available. Furthermore, $\dot{\mathbf{y}}_\mathbf{in} = \Delta\ddot{\mathbf{y}} = \boldsymbol{\nu}_{\boldsymbol{in}}$. The virtual control parameter $\boldsymbol{\nu}_{\boldsymbol{in}}$ could again be obtained with a P(ID) controller:

$$\boldsymbol{\nu}_{\boldsymbol{in}} = \mathbf{K}_{\mathbf{p,in}}\Delta\dot{\mathbf{y}} + \mathbf{K}_{\mathbf{i,in}}\Delta\dot{\mathbf{y}}\cdot t = \mathbf{K}_{\mathbf{p,in}}\boldsymbol{\nu}_{\boldsymbol{out}} + \mathbf{K}_{\mathbf{i,in}}\boldsymbol{\nu}_{\boldsymbol{out}}\cdot T \tag{7.20}$$

with $\Delta\dot{\mathbf{y}}$ following from the outer-loop control. Substituting $\boldsymbol{\nu}_{\boldsymbol{in}}$ into Equation (7.12) results in the deformable mirror actuator commands, $\mathbf{c}$:

$$\delta\mathbf{c} = \mathbf{c} = (\mathbf{B}^*)^{-1}\left[\boldsymbol{\nu}_{in} - \ddot{\mathbf{y}}\right] = \mathbf{CM}\left[\boldsymbol{\nu}_{in} - \ddot{\mathbf{S}}\right] \tag{7.21}$$

where $\ddot{\mathbf{y}}$ follows from the backward Euler method:

$$\ddot{\mathbf{S}} = \frac{\mathbf{S(k)} + 2\mathbf{S(k-1)} - \mathbf{S(k-2)}}{T} \tag{7.22}$$

Note that since the order of the second derivative is significantly larger than the order of the first derivative, $\ddot{\mathbf{S}}$ in Equation (7.21) needs to be scaled with a proportional gain. Moreover, the outer loop controlling this second derivative can be transformed such that is becomes a PI(D) control. Thus, Equation (7.21) becomes:

$$\mathbf{c} = \mathbf{CM}\left[\boldsymbol{\nu}_{in} - \mathbf{K_p}\ddot{\mathbf{S}}\right] + \mathbf{K_i}\mathbf{CM}\left[\boldsymbol{\nu}_{in} - \mathbf{K_p}\ddot{\mathbf{S}}\right]T \tag{7.23}$$

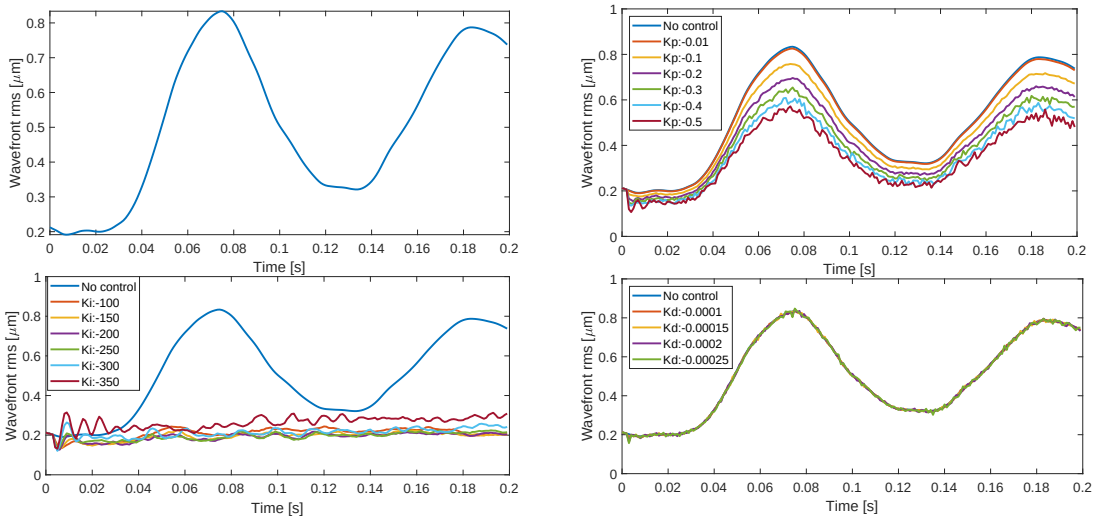

Figure 7.2: The effect of changing the individual gains on the residual error of the aberrations.

7.3 Gain tuning

Similar approaches where performed for the gain tuning process of the PID-controller and INDI-controller. Note that this process was initially done for the worst-case scenario with an atmospheric aberrations of r_0 = 3 cm and a wind speed of 15 m/s as mentioned in the requirements **TOGS-PR-05** and **TOGS-PR-06**, respectively. It was quickly observed that these conditions were too severe for the chosen HW components due to the restricted properties, irregardless of the gains chosen. The performance requirements stated to achieve at least both a fibre-optics coupling performance and Strehl of at least 40%. However, a maximum fibre-optics coupling of 33.0% was obtained along with a Strehl ratio 0f 29.1%. After careful considerations, requirement **TOGS-PR-05** was adjusted to a Fried parameter range of 6-20 cm.

In Figure 7.2, the effect of changing the gains individually on the residual aberrations are shown for the PID-controller. Similar observations were done for the INDI-controller. For the proportional gain in the top right corner, K_p, it is seen that the residual aberrations decrease, but the noise increases with decreasing K_p. Furthermore, the residual aberrations still follow the shape of the open loop aberrations seen in the top left corner. Changing the integral gain, K_i, decreases and flattens the residual aberrations significantly to an average of 0.2 μm. However, the overshoot and noise augments with decreasing K_i as seen for K_i = -350. Moreover, it is seen in the bottom right corner that decreasing the derivative gain, K_d, does not decrease the residual aberrations on its own, but only increases the noise.

Next, the gains will be analysed by combining K_p, K_i and K_d, which is shown in Figure 7.3. On the top, the effect of changing K_i while keeping K_p constant is seen. With K_p = -0.2 and K_i = -250 and K_i = -350, the residual aberrations are significantly decreased and remain small over the entire time period with relatively low noise. However, when decreasing K_i to -450, the residual aberrations start to increase slightly. At K_i = -550, the system becomes unstable and the residual aberrations increase to infinity and oscillate. When decreasing K_p to -0.4, the noise on the residual aberrations increases. However, the residual errors do not increase to infinity with K_i = -550.

Then, in the two bottom plots, it is seen that decreasing K_d again increases the noise on the residual aberrations, and the noise increases with decreasing K_p.

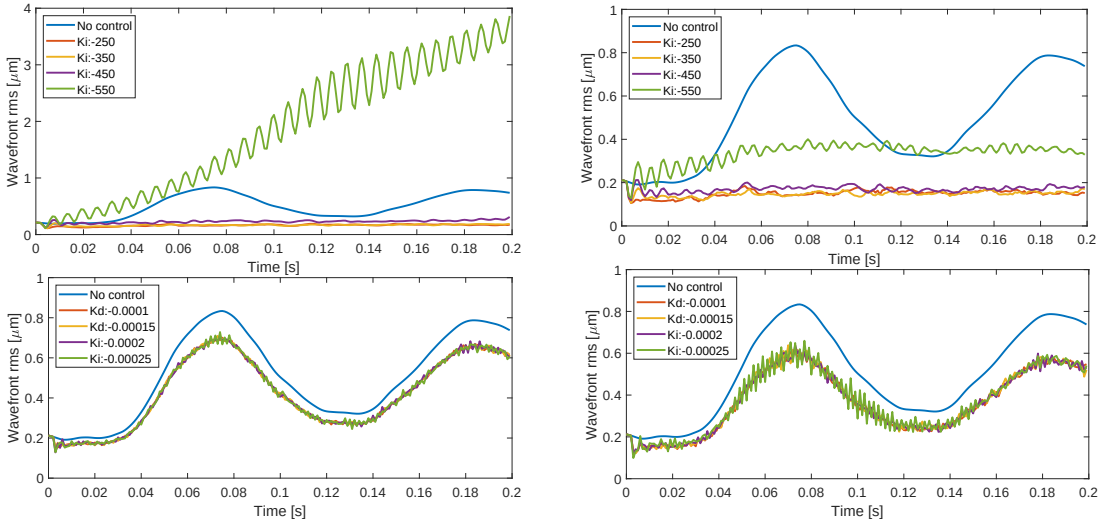

Figure 7.3: The effect of changing keeping a constant K_p and changing K_i and K_d on the residual rms error of the aberrations.

Finally, the combination of all three gains was observed and shown in Figure 7.4, where K_p and K_i are kept constant and K_d is varying. A slight overshoot is seen at the beginning. Moreover, the noise increases with decreasing K_d, and gets worse for K_p = -0.4.

After tuning the gains, the preliminary gains chosen are $K_p = -0.25$, $K_i = -300$ and $K_d = -0.0001$.

To set the nominal gains for the INDI, a factorial design method was used for four gains, namely the proportional and integral gain of the inner and outer loop; K_{pi}, K_{po}, K_{ii}, K_{io}. Factorial design is a design of experiments method that is applied when more than one variable is altered. This factorial design consisted of three levels, meaning that each gain has a minimum, a nominal, and a maximum value assigned. Since four gains are varied, there are a total of $3^4 = 81$ simulations. The gains of the outer loop controlling the second derivative of the error were fixed to $K_p = 0.0002$ and $K_i = 400$.

After running all simulations, the gains that resulted in the minimum integrated state deviation were selected, as well as the ones causing the minimum integrated control effort within the acceptable range. These conditions are crucial as the minimum state deviation will result in the most accurate system performance. However, the integrated control effort that is paired with these results, which defines the energy used by the system, may be significant. Therefore, both properties should be considered, as the results for the minimum integrated control effort might still meet the requirements, while also allowing the system to save energy.

The integrated state deviation, SD, and the integrated control effort, CE, are obtained by calculating the area below the curves of the residual error, $\mathbf{e}$, and the actuator coefficients, $\mathbf{c}$, respectively. This process is depicted in Figure 7.5. Here, the area below the curve for a certain time interval dt, is calculated for each data point of the function $f(x)$, which is depicted by the orange beams. The absolute sum of these beams results in the total area of the function, also known as the total error of the system. The relations for the integrated state deviation and control effort are given by Equations (7.24) and (7.25). The state deviation and the control effort per batch is shown in Figures 7.6(a) and 7.6(b), respectively. Here, it is can be seen that after run number 28, the standard deviation and the control effort become significantly large. Therefore, only the gains of the run numbers before number 28 can be

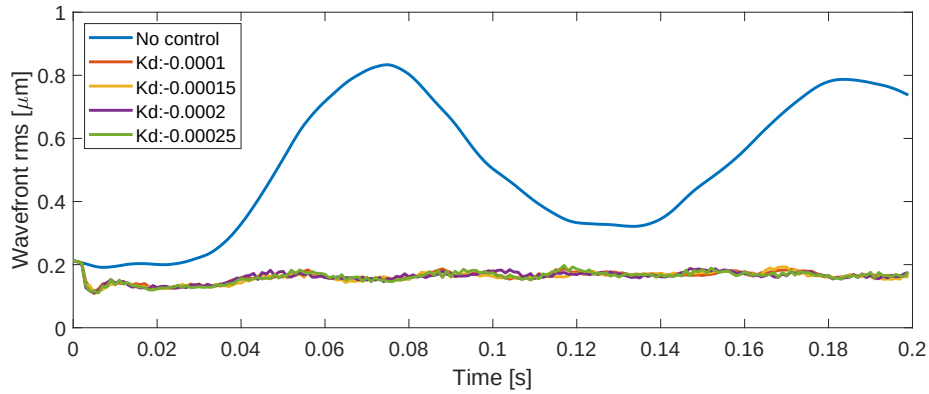

(a) Changing K_d with K_p=-0.2 and K_i=-250

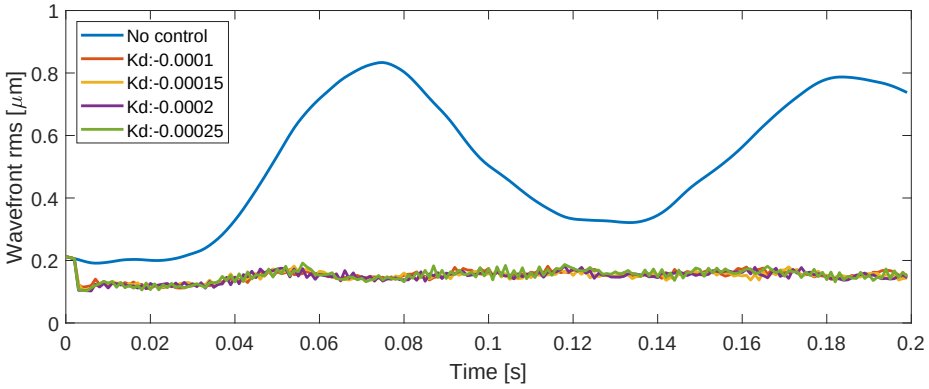

(b) Changing K_d with K_p=-0.4 and K_i=-250

Figure 7.4: The effect of changing K_d while keeping K_p and K_i constant

considered relevant. From these batches, the corresponding nominal gains for both cases were selected and are given in Table 7.1. Note that the gains for both the PID and the INDI are actually vectors, as they are applied to all actuators of the DM. However, since the value of the gain is kept the same for each actuator, the gain value is written as a scalar.

Comparing the results from the INDI-controller to the PID-controller, shown in Figures 7.7(a) and 7.7(b), several differences can be observed. First, it is seen that the state deviation for a PID-controller, shown in Figure 7.7(a), has an average of 0.035 μm. For the batches below number 28 for the INDI-controller, it is seen that the state deviation can be even lower than 0.02 μm, as stated in Table 7.1. For the PID-controller, the minimum state deviation equals 0.029 μm with K_p = -0.4, K_i = -250 and K_d = -0.00015. Furthermore, the control effort are in the same order, but are lower than $0.2{\cdot}10^{-7}\mu$ms for the batches of the INDI-controller. For the PID-controller, the minimum control effort only equals $0.25{\cdot}10^{-7}\mu$ms with K_p = -0.4, K_i = -250 and K_d = -0.0002. Moreover, it is seen that for the PID-controller, both the state deviation and control effort do not reach a certain batch where the results become significantly inaccurate, as was seen for the INDI-controller. Nevertheless, it can be concluded from these plots that with an INDI-controller, the system does reach lower state deviation and a lower control effort values. Thus, a better system performance is reached with an INDI-controller.

$$SD = \left|\left(\sum \mathbf{e}\right) T\right| \tag{7.24}$$

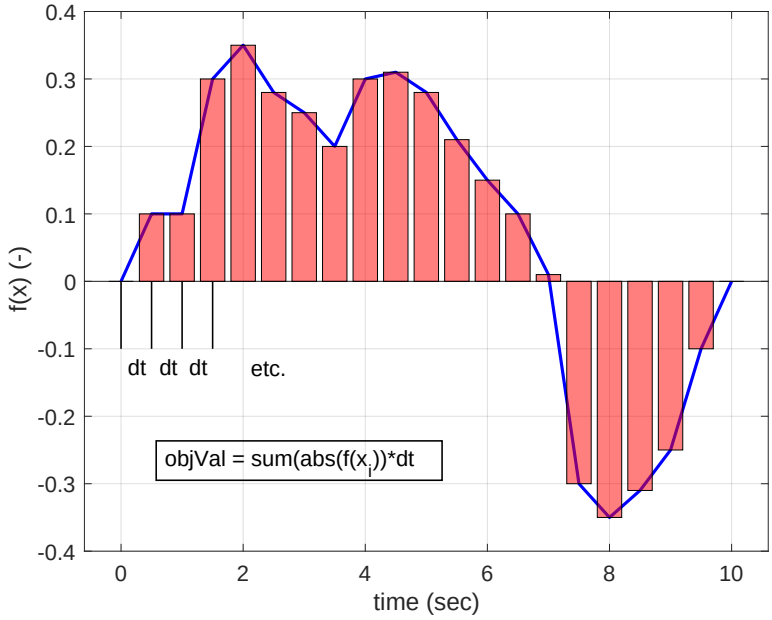

Figure 7.5: Calculating the area below a curve.

Table 7.1: Nominal gains for the INDI for a minimum state deviation and minimum control effort.

	min. state deviation	**min. control effort**
K_{pi}	-0.75	-0.75
K_{po}	-0.75	-0.5
K_{ii}	-12.5	-12.5
K_{ii}	-300	-300
state deviation	0.0129	0.0148
control effort	$2.3228 \cdot 10^{-8}$	$1.7439 \cdot 10^{-8}$

where T is the sampling time.

$$CE = \left| \sqrt{\left(\sum \mathbf{c} \cdot \mathbf{c} \right) T} \right| \tag{7.25}$$

where $\mathbf{c}$ is are he DM coefficients and T is again the sampling time.

7.4 Frequency analysis of controllers

In the frequency domain method, a controller is connected to the process, which allows to study the behaviour of the PID-controller and INDI-controller.

The transfer function gives a good characterisation of the linear behaviour of a system. Typically, $H_{OL} + H_{CL} = 1$, where H_{OL} and H_{CL} are the transfer functions of an open-loop and closed-loop, respectively. To provide specifications, it is desirable to capture the characteristic properties of a system with a few parameters. Common features of frequency responses are resonant peak, peak frequency and bandwidth. A resonant peak is a maximum of the gain, and the peak frequency is the corresponding frequency. Furthermore, the bandwidth is defined as the frequency range where the closed loop gain is $1/\sqrt{2}$ of the low-frequency

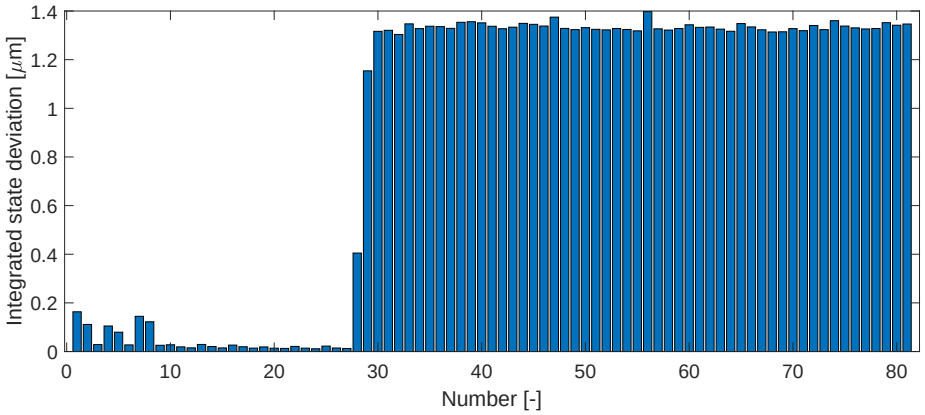

(a) The state deviation for each batch where the gains for the INDI-controller are varied.

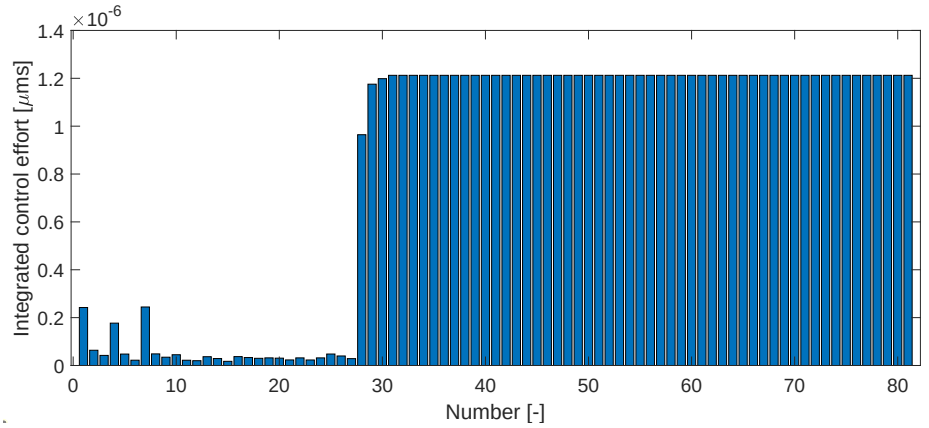

(b) The control effort for each batch where the gains for the INDI-controller are varied.

Figure 7.6: The standard deviation and control effort for the varying gains of the INDI-controller during the gain tuning process.

gain (low-pass), mid-frequency gain (band-pass) or high-frequency gain (high-pass). An example of a frequency response of a CL system is given in Figure 7.8.

A simple criterion for disturbance attenuation is to compare the output of the closed-loop system with the output of the corresponding open-loop system. If the disturbances for the open-loop and closed-loop systems are identical, the output of the closed loop system is then obtained simply by passing the open loop output through a system with the transfer function H_s, also known as the sensitivity function:

$$H_s = \frac{1}{1+PC} \tag{7.26}$$

where P denotes the process and C is the controller. The sensitivity function tells how the variations in the output are influenced by feedback. Disturbances with frequencies such that $|H_s| < 1$, are attenuated, while disturbances with frequencies such that $|H_s| > 1$ are amplified by feedback. The maximum sensitivity, M_s, is thus a measure of the largest amplification of the disturbances. The maximum magnitude of $1/(1+PC)$ is also the minimum of $|1+PC|$, which is known as the stability margin, s_m, so that $Ms = 1/s_m$. The stability margin is the shortest distance from the Nyquist curve to the critical point, as depicted in Figure 7.9. Here, all points inside the dashed circle have sensitivities greater than 1. Therefore, the maximum sensitivity is a robustness measure for a control system. A typical value to ensure the system

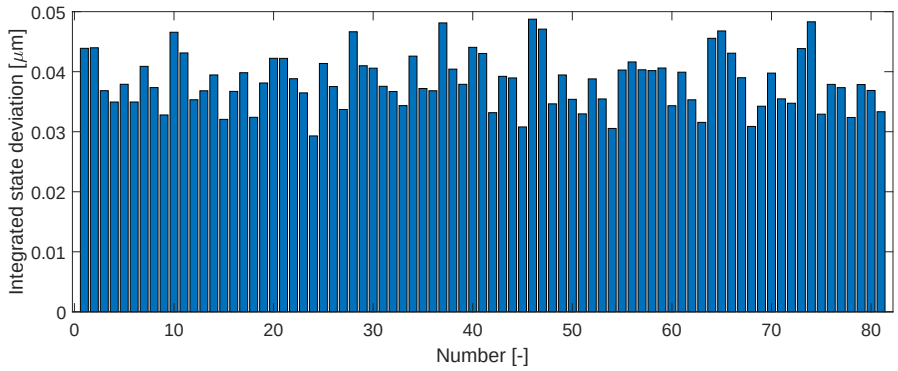

(a) The state deviation for each batch where the gains for the PID-controller are varied.

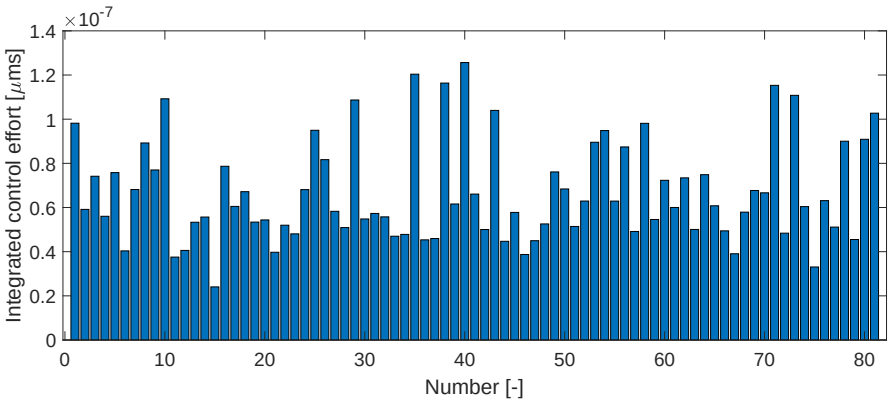

(b) The control effort for each batch where the gains for the PID-controller are varied.

Figure 7.7: The standard deviation and control effort for the varying gains of the INDI-controller during the gain tuning process.

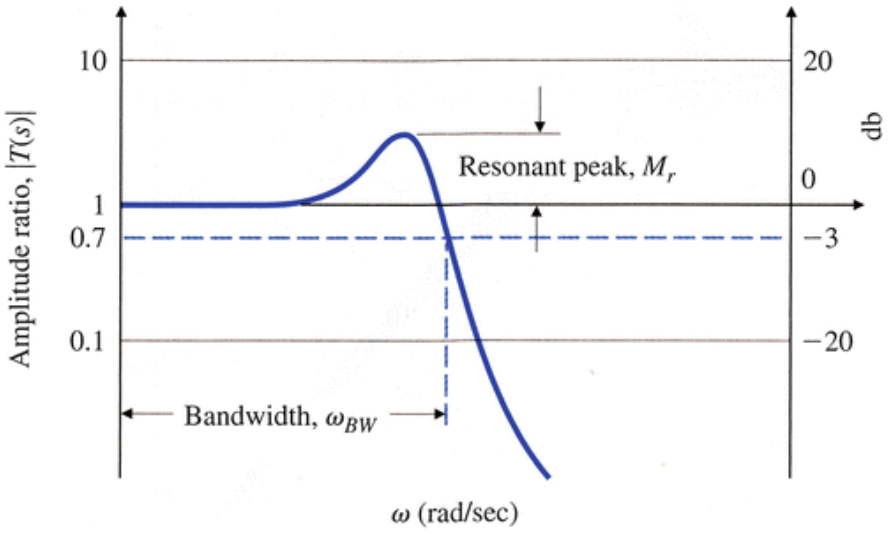

Figure 7.8: Typical frequency response for a CL system (Emami-Naeini and Powell, 2019).

is robust is when the peak meets $|H_s| < 2$ (Johan et al., 2008). The Power Spectral Density (PSD) is a measure of the distribution of power over the frequency range. Abundant processing capabilities of modern computers make it possible to obtain the PSD by means of the

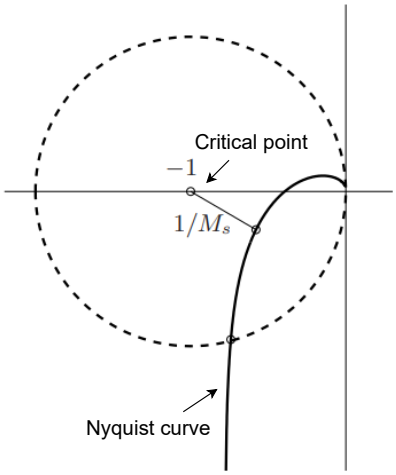

Figure 7.9: Nyquist curve of loop transfer function showing graphical interpretation of maximum sensitivity.

Fourier transform, commonly using a Fast Fourier Transform (FFT) algorithm. The caveat is that a typical random process, as it is theoretically defined, is not periodic and extends to infinity in the time domain, meaning that the following first-type boundary condition, also known as the Dirichlet condition, is not fulfilled:

$$\int_{\infty}^{\infty} |x(t)| dt < \infty \tag{7.27}$$

The formal theoretical definition of the PSD, employing the Fourier transform, is then based on the autocorrelation function $R_{xx}(\tau)$, which implicitly contains the frequency content of the function $x(t)$ while also satisfying the condition from Equation (7.27), at least for the case of zero-mean processes. Since the autocorrelation function and the PSD are a Fourier transform pair, the following relations, known as the Wiener–Khinchin relations, can be written for the random processes $x(t)$ and $y(t)$:

$$S_{xx}(f) = FR_{xx}(\tau) \quad S_{yy}(f) = FR_{yy}(\tau) \quad S_{xy}(f) = FR_{xy}(\tau) \tag{7.28}$$

The PSDs $S_{xx}(f)$ and $S_{yy}(f)$ (also called autospectral densities) are even, real-valued, and positive functions. The cross-spectral density $S_{xy}(f)$ is in general a complex-valued function (Slavic et al., 2020).

To analyse the behaviour of the designed PID-controller and INDI-controller, a focus will be placed on the autospectral density $S_{xx}(f)$. This will be computed using FFT Welch's method. This method first divides a time series into overlapping subsequences by applying a window to each subsequence, and then averaging the periodogram of each subsequence (Solomon Jr, 1991).

From a control point of view, the feedback variable are the slopes given by the WFS. There are two parts of each slope in every lenslet of the microlens array: an x- and a y-coordinate.

If the system is modelled as a MIMO system between the DM actuators and the WFS, there will not only be one rejection function, but one for each x- and y-coordinate for each lenslet.

The PSD for an open-loop and closed-loop simulation with a PID-controller are shown in Figure 7.10 and Figure 7.11, respectively. Several aspects can be observed. First, it attenuates at low frequencies. As seen in the open-loop PSD before 100 Hz, the gains vary in the order

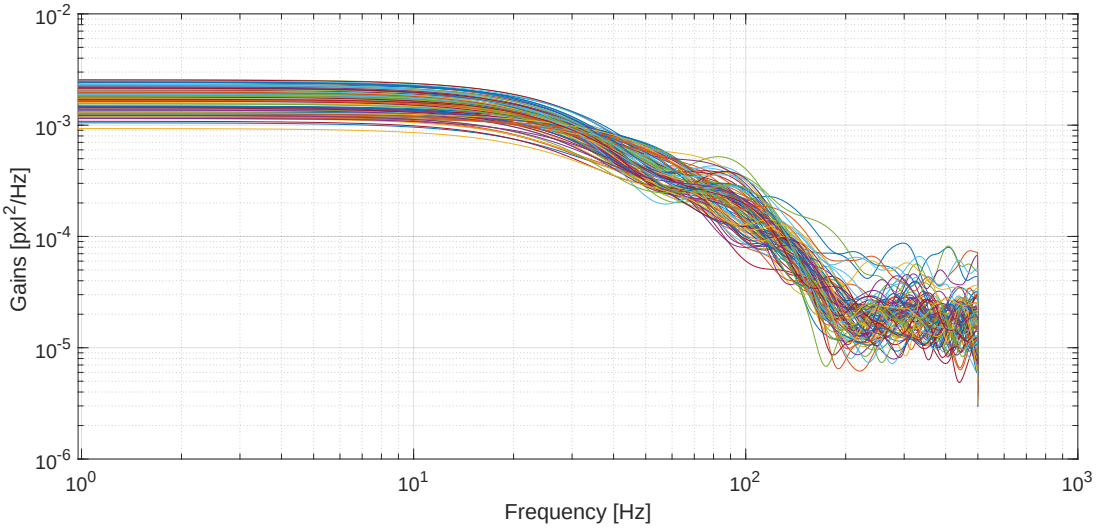

Figure 7.10: PSD of the open-loop simulations.

between 10^{-2} and 10^{-3}, and this is lowered in the closed-loop PSD to 10^{-3} and 10^{-4}, meaning that the aberrations are corrected for at low frequencies. This is as expected, as the low-order Zernike polynomials mainly represent the global contour of a pattern, while the higher-order terms describe the detail. Thus, if the PSD of those Zernike polynomials were taken, a higher activity would be present at low frequencies. (Xiang, 2012).

Then, as seen in Figure 7.11, it amplifies between 100-200 Hz where resonant peak is reached at a peak frequency of 140 Hz. Moreover, the bandwidth is approximately 200 Hz.

Finally, both plots attenuate past 200 Hz, at higher frequencies. This is related to the data sampling according to the predefined resolution of the measurements. Since the plots are logarithmically scaled, there will be more samples present at higher frequencies and, thus, more noise. This can be fixed by adding a stronger filter, which in turn reduces the number of samples. Similar results were observed for the INDI-controller.

The rejection function shown in Figure 7.12, depicts the ratio between the CL and OL PSD measurements. At low frequencies, the rejection function has low values, which means that most of the aberrations in OL are corrected for. Then, it amplifies between 100-200 Hz and reduces again. As mentioned before, the resonant peak of the curve is a measure of robustness for a control system. Since the criterion for a robust system is $|H_s| < 2$ this controller meets the criterion, as the values of the peaks are all around 1. The frequency analysis was performed for the INDI-controller as well, and the same criterion was met for the INDI-controller.

7.5 Robust design method (PID)

To analyse the behaviour of the original I-controller and the controllers with the preliminary gains, Monte Carlo (MC) simulations will be used. This method is relatively simple to implement, as it is a matter of varying the input, run the simulations, and store the output. However, since many data are generated, it may be complex to decide what to do as data analysis, when used for a larger number of simulations. Moreover, it might be time consuming, as there may be many blank spots in the design space when sampling it, which would indicate an excessive number of simulations. The parameters that were varied are stated in Table 7.3. The limits are based on the requirements set for the TOGS, which correspond

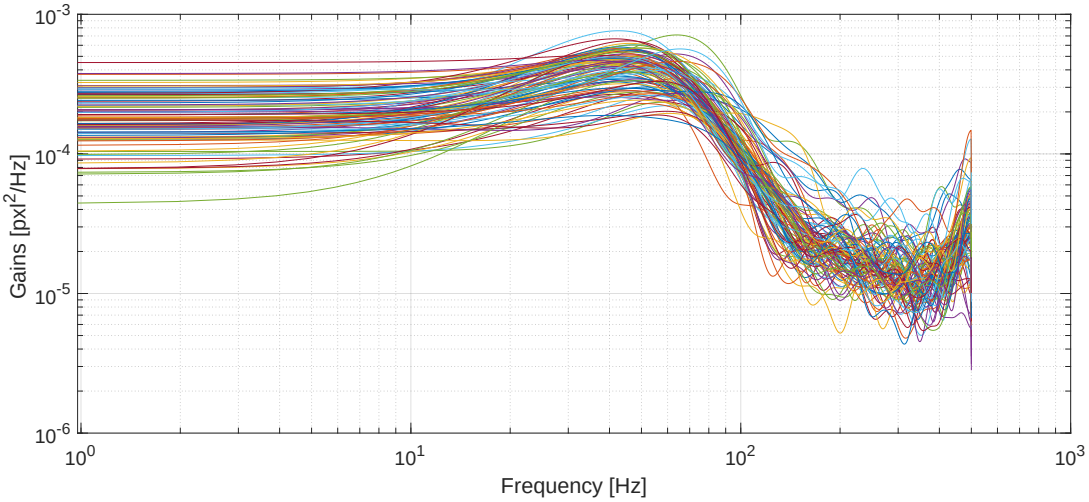

Figure 7.11: PSD of the closed-loop simulations with a PID-controller.

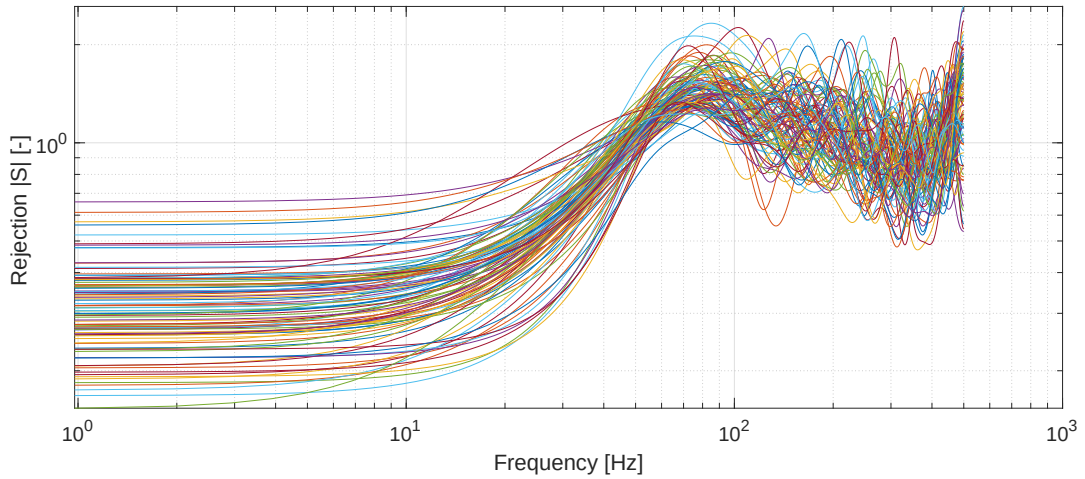

Figure 7.12: Rejection function

to the conditions experienced in the observatory of “el Teide”, and the design constraints. Since six parameters are varied, a simulation with 300 iterations is performed, which gives 50 variations per parameter. This was deemed a reasonable number, considering the Central Processing Unit (CPU) time is limited.

The fibre-optics performance using an I-controller is depicted in Figure 7.13. As seen, around 40% is below a 40% fibre-optics coupling performance. Therefore, the I-controller does not meet the requirements and, hence, is not suitable for this system. However, the maximum Strehl ratio achieved is 75%, which meets the requirement stating a minimum Strehl of 40% must be achieved.

Then, the fibre-optics coupling performance with a PID-controller with the preliminary gains is given in Figure 7.14. Here, a coupling performance of at least 84% is obtained, which satisfies the requirements. A mean of 91.7% is attained. Moreover, all the values within a standard deviation of ±1 STD, marked with the dashed lines, meet the requirements. This means that the system already reaches a better performance with a PID-controller.

Next, to find the optimal gains for the PID-controller, a robust design using factorial design is implemented as explained in Section 7.3. This method is used when the system is

unknown and one needs to establish the factors of influence. The factorial design includes an orthogonal matrix, which suggest that for any pair of columns, all combination of factor levels occur an equal amount of times. Here, it is assumed that there are no interactions between the design parameters, which means that a factor can be assigned to each column. This application requires many simulations, which suggest a large CPU load. Nevertheless, it enables to understand the system better than when using Monte Carlo simulations.

Robust design is an engineering methodology to improve the quality of the product by minimising the effect of the use of variation without eliminating the causes. Here, the robust design will be based on the work of Mooij (2012) and consists of an inner and an outer loop to vary the parameters. The inner loop will represent the perturbations and vary them, whereas the outer loop will vary the control parameters. The inner loop will make use of MC simulations that will vary all accounted parameters randomly. However, a fixed seed will be set at the start of each batch so the same combination of perturbations are analysed in each outer loop.

Then, the outer loop will use factorial design. Three levels for each gain are implemented namely, a minimum, a nominal and a maximum value, meaning the outer loop will consist of $3^3 = 27$ iterations. The three levels for each gain is decided during the tuning of the gain as explained in Section 7.3, and are stated in Table 7.2. Moreover, the parameters to be varied in the inner loop with the MC method with its corresponding limits are the same as during

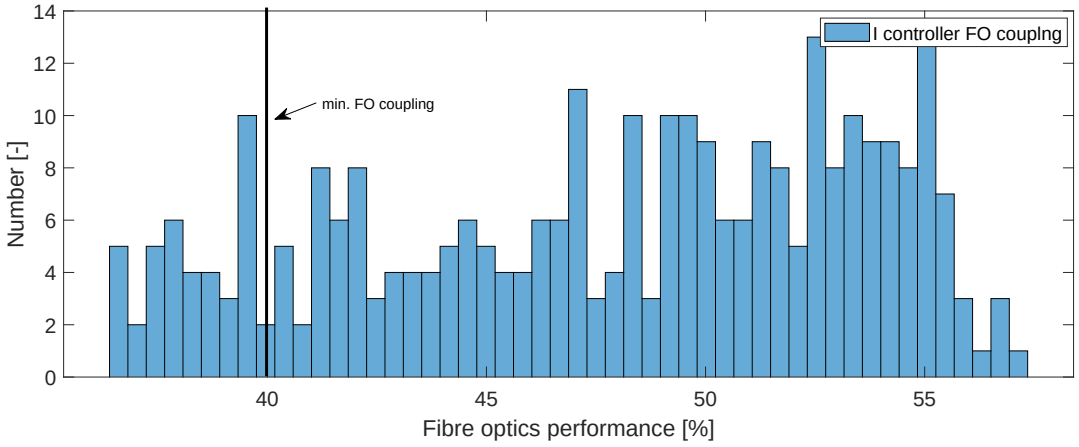

Figure 7.13: MC results of the fibre-optics performance with the nominal I-controller.

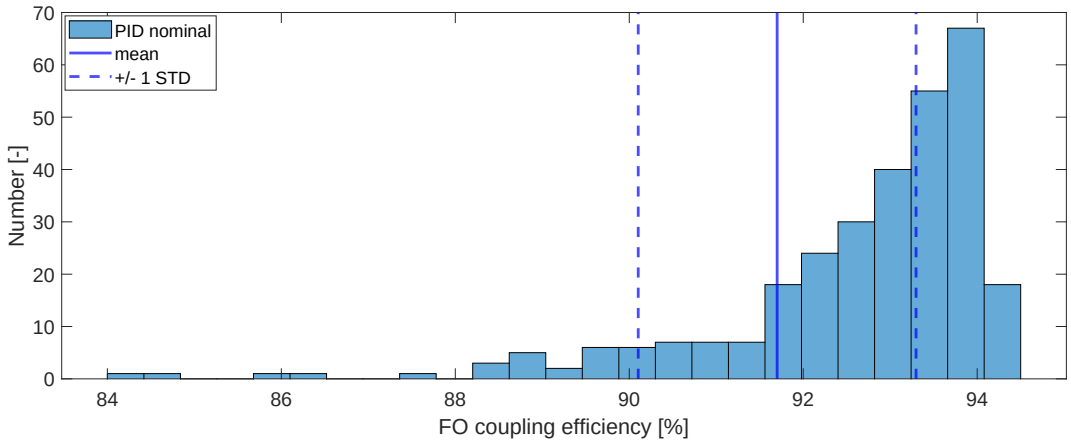

Figure 7.14: Fibre coupling percentage for the PID-controller with the predefined nominal gains.

Table 7.2: The values for the three levels decided for the gain to perform the factorial design.

Parameter	**Limits**
K_p	[-0.1, -0.2, -0.4]
K_i	[-150, -250, -350]
K_d	[-0.0001, -0.00015, -0.0002]

Table 7.3: System parameters varied in the sensitivity analysis.

Parameters	**Range**
Turbulence (r0)	6-20 cm
Wind speed (w0)	1-15
Diameter (D)	0.68-0.72
Readout noise	0.0-3.0
Quantum efficiency	0.5-0.9
Photon noise	0.0-1.0

the sensitivity analysis of the nominal gains and are stated in Table 7.3.

7.6 Post processing data (PID)

After running the sensitivity analysis, the mean as well as the Standard Deviation (STD) is calculated for the fibre-optics coupling performance and the Strehl ratio for each of the 27 designs. The data obtained for the fibre-optics coupling is shown in Figure 7.15. With the mean and the STD, the Signal to Noise Ratio (SNR), for each simulation can be calculated with:

$$SNR = \log\left(\frac{\mu^2}{\sigma^2}\right) \tag{7.29}$$

. Here, the mean is plotted in the upper left side, followed by the STD in the upper right side and the SNR on the bottom. It is seen that the mean does not vary much, but remains rather constant. However, the STD does change for each batch. This means that the SNR is mainly defined by the variations of the data points, also called the outliers. Note that the same behaviour was observed for the system's Strehl ratio.

The corresponding gains will then be decided based on the simulation with the largest SNR ratio. This is coupled to a large mean and a small STD, meaning that the variability of the data points is small. Subsequently, a large SNR means that the data points will not vary much from the high mean value, thus the batch results in the most accurate system performance with the least outliers. As seen, the largest SNR peaks in the histogram are paired with the lowest peaks of STD. The corresponding gains to the largest peaks are stated in Table 7.4. Note that all these peaks have a K_p of -0.4. From the residual aberrations seen during the gain tuning in Section 7.3, it was observed that higher gains are paired with higher noise values on the signal. Since it is seen that the means of the fibre-optics performance all meet the minimum fibre-optics performance requirement (40%) in Figure 7.15, it was decided to select a lower SNR peak, paired with a slightly higher standard deviation, to reduce the noise on the received signal. Therefore, batch number 12 was selected. This batch corresponds to a Strehl ratio with a mean of 94% and a mean fibre-optics coupling of 96%, which meets the requirements. The corresponding gains are $K_p = -0.2$, $K_i = -250$ and $K_d = -0.00015$, which will be the final gains used for the CL simulations with the PID-controller.

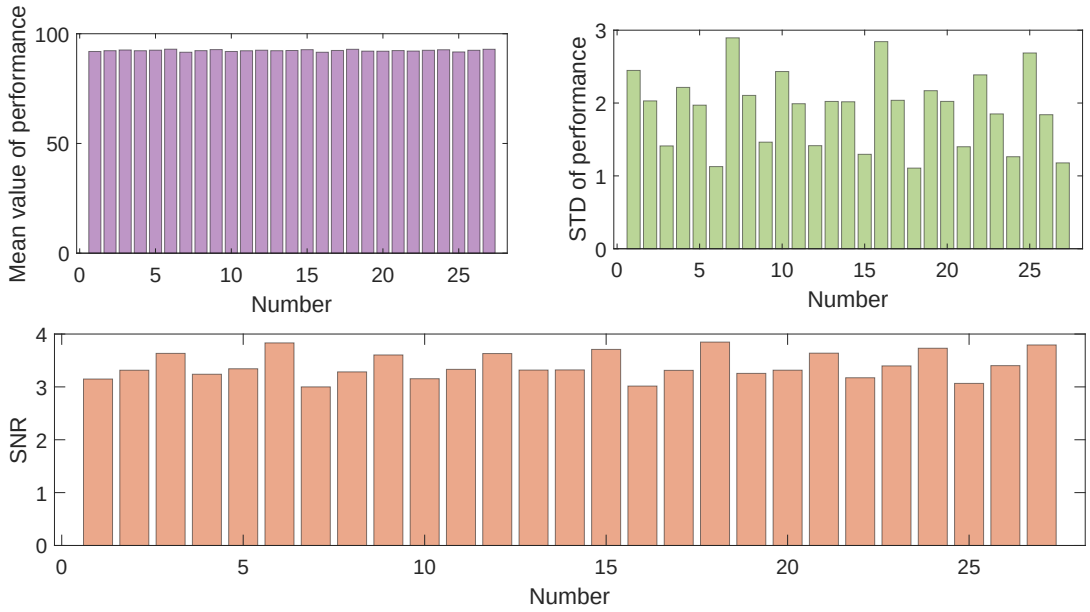

Figure 7.15: Robust design post processing results for fibre-optics coupling performance.

Table 7.4: Corresponding gains of the highest SN ratio peaks.

Iteration	**Gains**
3	[-0.4, -250, -0.0001]
6	[-0.4, -350, -0.0001]
9	[-0.4, -150, -0.0001]
12	[-0.4, -250, -0.00015]
15	[-0.4, -350, -0.00015]
18	[-0.4, -150, -0.00015]
21	[-0.4, -250, -0.0002]
24	[-0.4, -350, -0.0002]
27	[-0.4, -150, -0.0002]

Finally, a sensitivity analysis has been performed using the new gains for the PID-controller. The histogram for the fibre-optics coupling is given in Figure 7.16. The overall mean of the performance has increased to 93% and all values within ±1 STD meet the requirement.

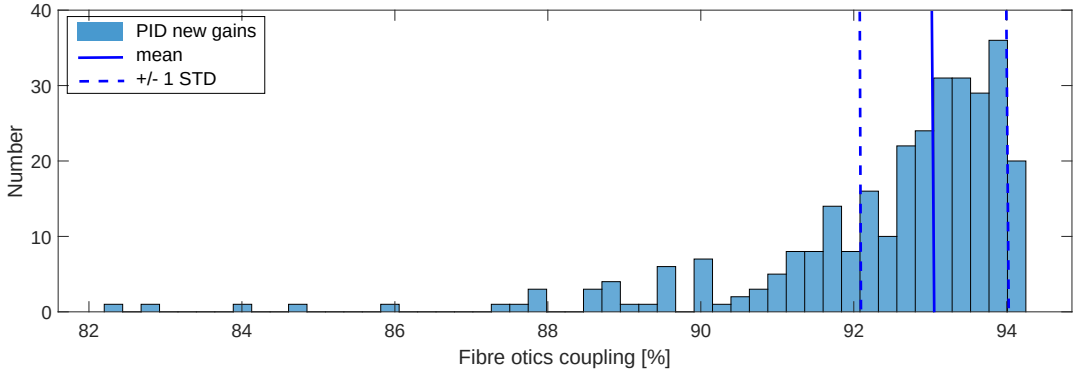

Figure 7.16: MC results of the fibre-optics performance with a PID-controller using the gains from batch 12.

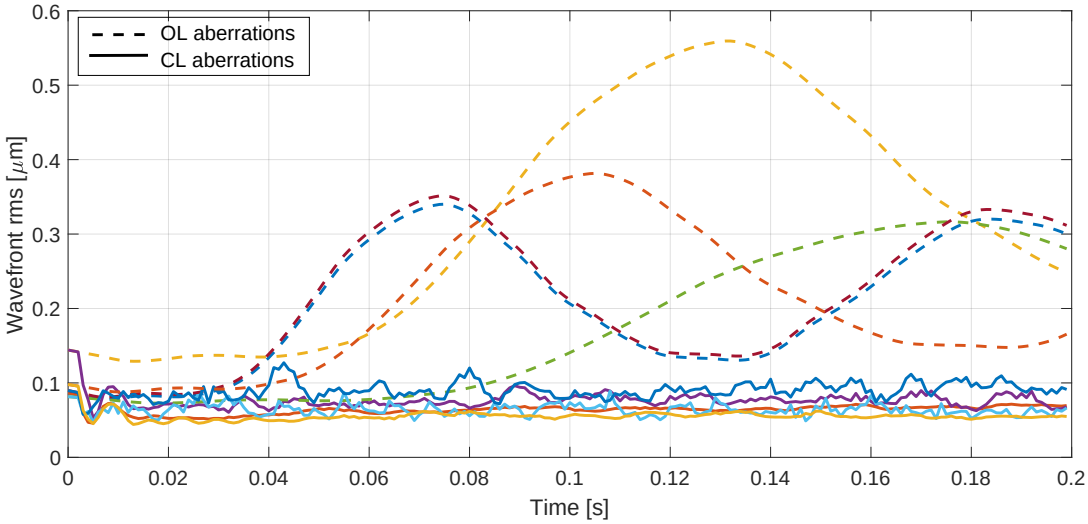

Figure 7.17: Residual aberrations for the PID-controller with the initial gains.

Finally, some of the residual errors from aberrations after the correction through a PID-controller are plotted in Figure 7.17, where the aberrations before correction are plotted with thick lines, and the corrected aberrations are the thin lines. As shown, all corrected aberrations are are less than the uncorrected aberrations and remain small over the entire time period. However, all include a slight overshoot at the beginning and some include an increase of noise in the corrected residual aberrations.

Due to time constraints, the robust design has only been applied to the PID-controller and not for the INDI-controller.

7.7 Comparison of the PID and the INDI

Next a sensitivity analysis was performed as described in Section 7.5 for the INDI-controller, which is then compared to the results from the sensitivity analysis of the PID-controller.

The fibre-coupling performance when using an INDI-controller is given in Figure 7.18 where the two cases previously mentioned in Section 7.3 are plotted. In blue, the gains corresponding to the minimum state deviation is presented, whereas the gains for the minimum control effort are stated in orange. As seen, both cases result in a minimum above 90%, which is higher than the achieved minimum coupling performance with a PID-controller. Furthermore, it is seen that the mean for the case of minimum control effort is lower than the mean for the case of minimum state deviation, which is as expected as a minimum state deviation results in a better coupling performance. This is clearly depicted by the blue bars being remarkably higher than the orange bar at larger values for the fibre-optics coupling. Again, all the values within a standard deviation of ± 1 STD for both cases meet the requirement.

Moreover, Figure 7.19 and Figure 7.20 show the state deviation obtained with the PID-controller with the gains selected from the robust design and the INDI-controller, respectively. Here, it is seen that for the PID-controller results in higher integrated state errors up to 0.03 μms, whereas the INDI-controller attains state deviations up until 0.018 μms only. Additionally, the control effort for both the PID and INDI were studied and plotted in Figure 7.21 and Figure 7.22. Overall, the control effort is within the same range for both cases. However, the mean of the control effort for the INDI is approximately twice as low as for the PID. Thus, the INDI-controller proves to be more energy-effective than the PID-controller,

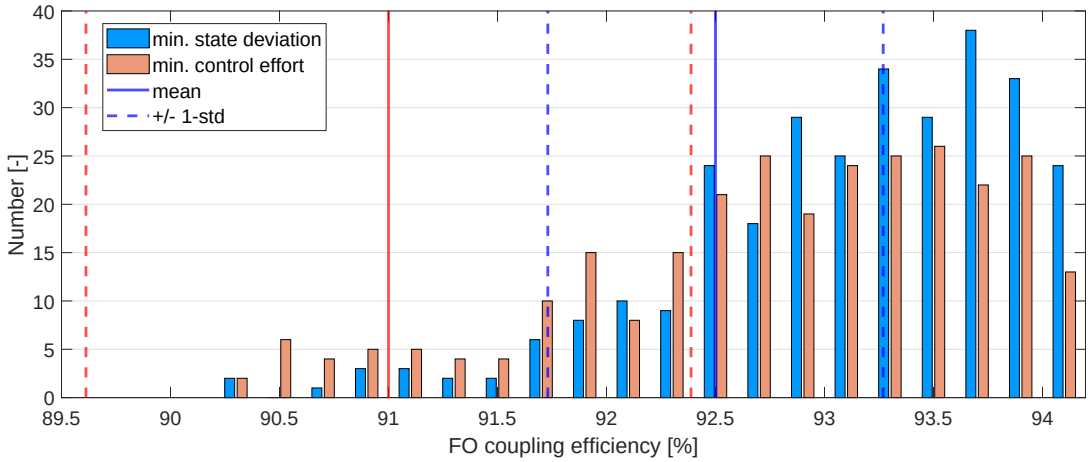

Figure 7.18: Fibre coupling percentage for the INDI-controller with gains corresponding to the minimum state deviation and minimum control effort.

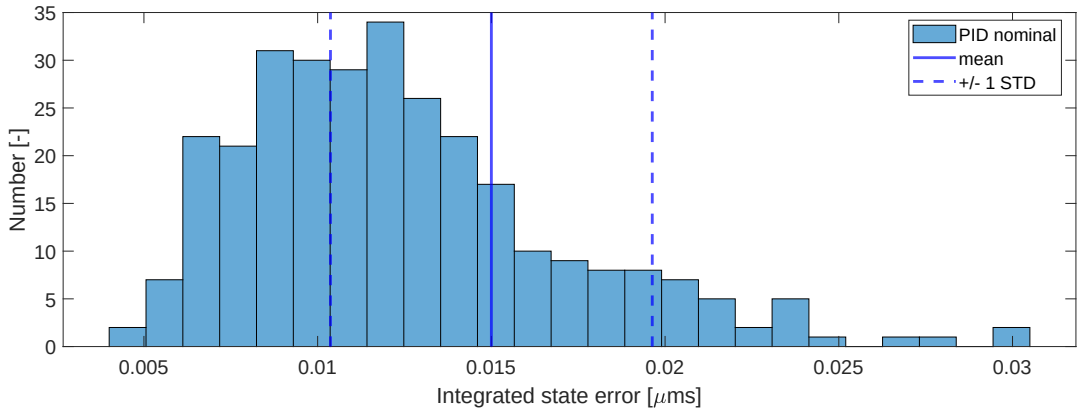

Figure 7.19: State deviation for the PID-controller with the predefined nominal gains.

while also achieving a better fibre-optics coupling. Also, the standard deviation of the control effort is twice as large than the standard deviation of the state deviation, meaning the data points of the state deviation tend to be closer to the corresponding mean. In other words, the variability of the data points is less for the state deviation than for the control effort, meaning the data for the standard deviation is more accurate.

7.8 Verification of the PID-controller

Since, the controller was made from scratch, verification tests were performed on the PID-controller. The tests are listed in Table 7.5. P/F stands for pass/fail. As seen, all the tests passed. Note that no specific verification tests were performed on the IND-controller due to time constraints.

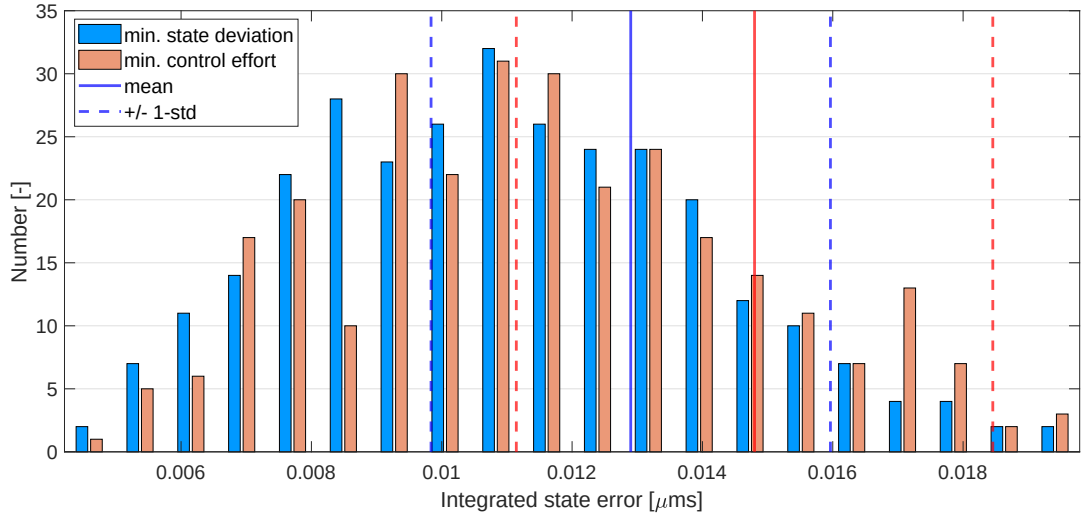

Figure 7.20: State deviation for the INDI-controller with gains corresponding to the minimum state deviation and minimum control effort.

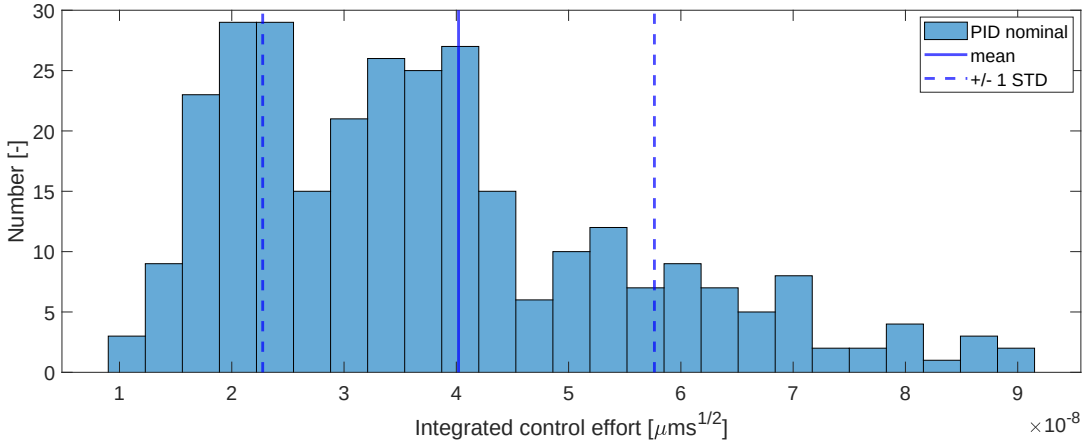

Figure 7.21: Control effort for the PID-controller with the predefined nominal gains.

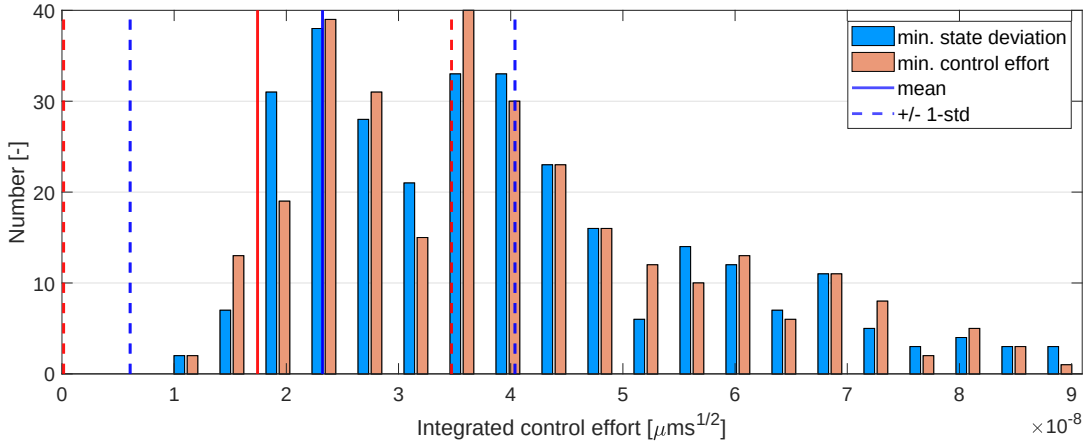

Figure 7.22: Control effort for the INDI-controller with gains corresponding to the minimum state deviation and minimum control effort.

Table 7.5: Unit tests of the PID controller

ID	Test	P/F
C-1.1	The PID-controller should get the same results as the I-controller with K_p and K_d equal to 0.	P
C-1.2	Introducing delays in the system should result in oscillations at the beginning.	P
C-1.3	Increasing K_p should reduce the oscillations.	P
C-1.4	Increasing the gains should result in more noise in the system.	P
C-1.5	Increasing K_i should reduce the residual error.	P
C-1.6	Increasing the controller gains should result in a better performance	P
C-1.7	The derivation of the PID equations should be the same as when derived by hand.	P
C-1.8	The Strehl without a controller (open-loop) should be equal to 1.	P
C-1.9	Increasing K_d should result in more noise (when no filter is applied).	P
C-2.0	When setting the gains to 0 the corrected aberrations should equal the uncorrected aberrations	P
C-2.1	When the simulations are performed with all gains being 0, the sensitivity function should equal exactly 1 over the entire duration of the simulations.	P

CHAPTER

8 Results

In this chapter, the results of the AO system performance with the designed controllers are discussed. In Section 8.1, the simulation results obtained with OOMAO will be described. Then, the experimental results from the test set-up are stated in Section 8.2. Finally, Section 8.3 will elaborate upon the differences between the simulations and the experimental results, including the causes of these observed differences.

8.1 OOMAO simulation results

After performing the sensitivity analysis in Chapter 7, an open-loop and closed-loop simulation were performed in OOMAO with the parameters given in Chapter 5 and the gains stated in Table 8.1. The closed-loop simulations using a PID-controller and an INDI-controller resulted in the residual errors shown in Figure 8.1. As seen, a small overshoot takes place at the beginning but quickly stabilises to a constant residual error that is significantly less that the aberrations present in a open-loop simulation. Also, the residual error is less when using an INDI-controller instead of a PID-controller, meaning the INDI-controller corrects better for the incoming aberrations. Moreover, noise seem to be present in both cases, which prevents the residual aberrations from being a smooth, constant line.

Additionally, the fibre-optics coupling performance was analysed. In Figures 8.2(a) and 8.2(b), the initial light source retrieval with fibre optics and ideal light source retrieval by the entire telescope are shown when using a PID-controller. Here, an intensity peak is seen in the

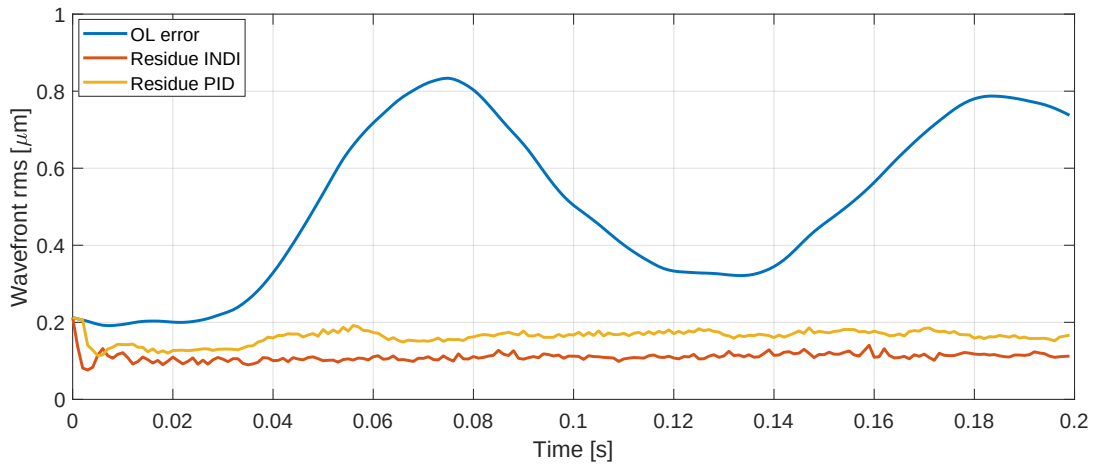

Figure 8.1: Residual errors after closed-loop simulations with a PID-controller (yellow) and INDI-controller (red).

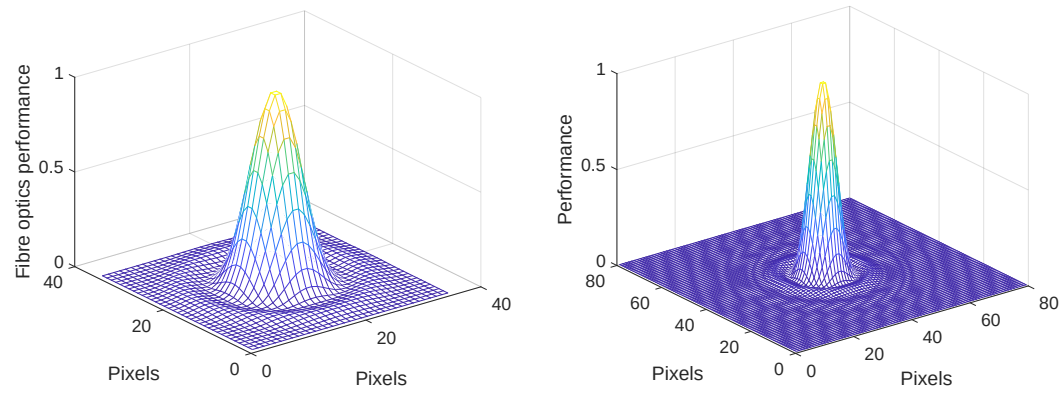

(a) Initial light source retrieval when fibre-optics coupling is installed

(b) Ideal light source retrieval measured by the telescope.

Figure 8.2: Initial measurements when the fibre-optics coupling is installed.

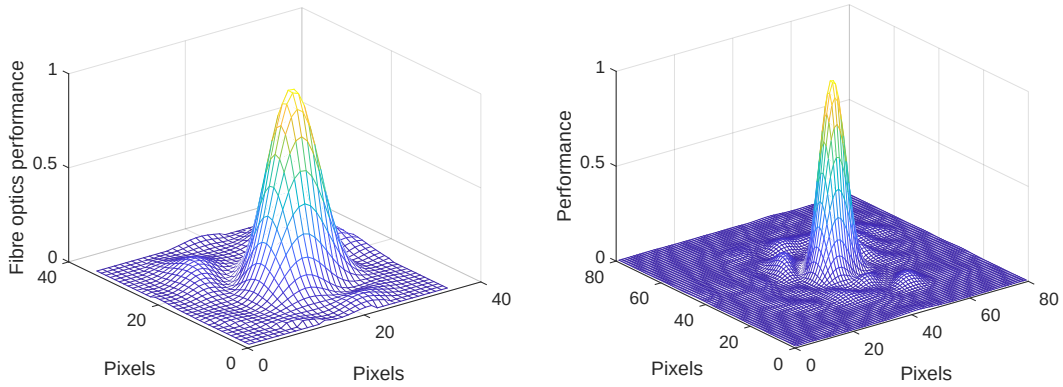

(a) Fibre-optics performance after adding the atmosphere in an OL simulation.

(b) Telescope system performance after adding the atmosphere in an OL simulation.

Figure 8.3: Fibre-optics coupling performance with the presence of the atmosphere in an OL simulation.

middle of the nPx by nPx camera frame. Only one intensity peak occurs, as the source measured is a point source. The maximum peak value is normalised to be the ideal, maximum value measured by the camera. This serves as the reference to compute the ratio between the incoming light and the maximum amount of light the system can measure. Moreover, the reference image corresponds to an ideal diffraction limited image. Then, the fibre-optics coupling and the entire telescope system is studied when the atmospheric aberrations are added, which equals to the result of an open-loop simulation, when no controller is present. These are depicted in Figures 8.3(a) and 8.3(b), respectively. As seen in both, the light is not diffraction limited anymore, but fluctuates around the centred, maximum peak of light, which is due to the presence of atmospheric aberrations. Note that these meshes do not depend on the controller used, but on the properties of the atmospheric aberrations. The fluctuations are coupled to a loss in quality in information retrieval. The ratio between the value of this new intensity peak and the ideal intensity peak decides the fibre-optics coupling when no controller is implemented. Finally, the coupling and the telescope performance for the closed-loop simulation using a PID-controller is given in Figures 8.4(a) and 8.4(b), respectively. Comparing Figure 8.4 to Figure 8.3, the fluctuations around the largest peak are

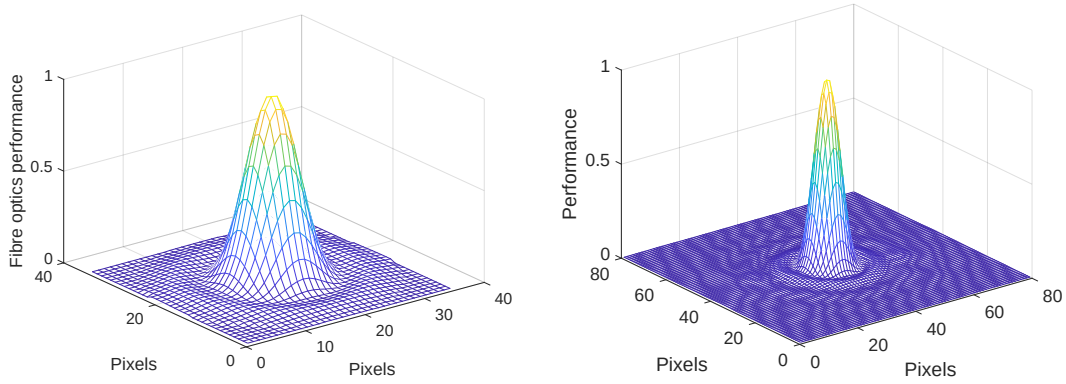

(a) Fibre-optics coupling in a CL system with a PID-controller.

(b) Telescope system performance in a CL system with a PID-controller.

Figure 8.4: Fibre-optics coupling after CL simulation with a PID-controller.

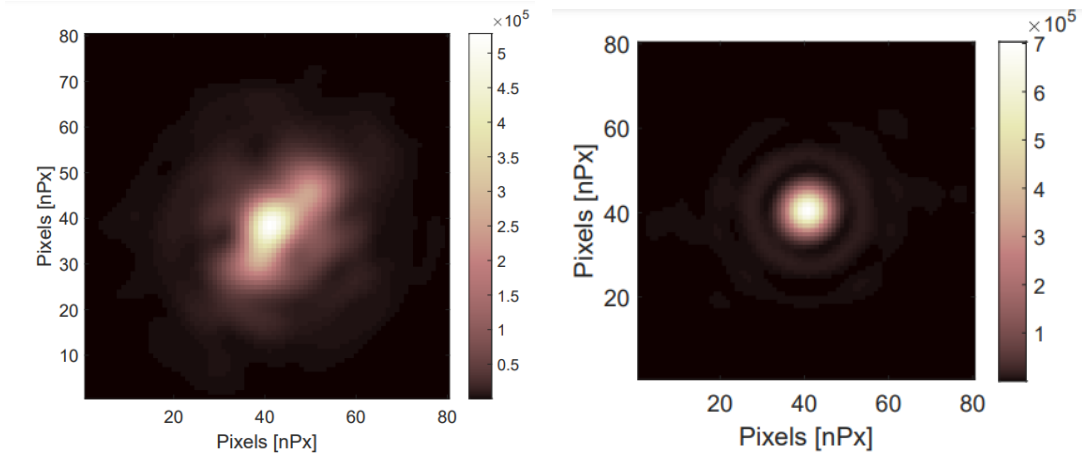

(a) Image retrieved by the camera during an open-loop simulation.

(b) Image by the camera during an closed-loop simulation with a PID-controller.

Figure 8.5: Comparing the image retrieved during an OL and CL simulation with a PID-controller.

no longer present. This shows that the controller in the closed-loop simulations successfully corrects for the aberrations induced by the atmospheric turbulence.

Furthermore, the image quality was analysed for an OL simulation in Figure 8.5(a) and a CL simulation in Figure 8.5(b) to visualise the correction. The quality of an image is paired with the Strehl ratio. As seen, the image quality is significantly improved when applying a PID-controller, and the image obtained for the CL simulation is diffraction limited again. Similar images were obtained for the INDI-controller.

In Table 8.1, the performance results for an OL and CL simulation are stated for several values of atmospheric aberrations. A seen, for the worst case scenario represented by r_0 = 6 cm, the CL simulation using a PID-controller resulted in a coupling of 82.7%, which satisfies the requirement of having at least a coupling of 40%. Moreover, the Strehl ratio equals 67.75%, meaning that also this requirement is satisfied. Additionally, the fibre-optics coupling performances for other Fried parameters have been studied, namely r_0 = 7.8 cm, r_0 = 15.5 cm, and r_0 = 23.3 cm, respectively. These values were chosen such that it coincides with the Fried parameters of the available phase plates in the laboratory, as explained later in Sec-

tion 8.2. As seen, r_0 = 15.5 cm results in a better performance than for r_0 = 7.8 cm. This is expected as it coincides with a lower atmospheric perturbation. However, when r_0 = 23.3 cm, the atmospheric aberrations are so low that it reaches a certain minimum, causing the AO system to saturate. Therefore, the coupling achieved in CL simulations (90.7%) becomes less than the fibre-optics coupling performance in OL (92.7%).

For the INDI-controller, an even better fibre-optics coupling was obtained compared to the PID-controller. For r_0 = 6 cm, a coupling of 89.3% was retrieved. Increasing the r_0 to 7.8 cm and 15.5 cm, resulted in a coupling of 90.8% and 92.6%, respectively. Finally, similar to the PID-controller, the AO system becomes saturated for r_0 = 23.3 cm, which causes the CL coupling (90.9%) to be lower than the initial OL coupling (92.7%). Nevertheless, the INDI-controller showed to achieve a better fibre-optics coupling and a better image quality than the PID-controller for the same conditions.

8.2 Experimental set-up (PID)

The closed-loop simulations with the experimental set-up have been carried out for three atmospheric conditions: Phase plates with r_0 = 1 mm, r_0 = 2 mm , and r_0 = 3 mm have been used, respectively. Again, a higher r_0 corresponds to weaker atmospheric perturbations. However, the aberrations have to be scaled according the diameter of the WFS aperture used in the laboratory, and the desired telescope diameter. The scaling of the atmospheric aberrations to know what the TOGS would experience is given in Table 8.2. Note, that tests were performed with the PID-controller only, due to the availability of the hardware.

In this section, the results for all three cases will be described individually.

Phase plate r_0: 1mm

For a phase plate with r_0 = 1 mm, the aberrated image retrieved is shown in Figure 8.6(a), which is the image retrieved for an OL simulation. This image is processed as depicted in Figure 8.7(a), and is similar to the calibration image process explained in Chapter 6. The aberrations cause the fibre-optics coupling to reduce to 50.5%, which was measured with the previously explained PM400 in Chapter 4. As seen, not all points are detected, which is due to the aberrations present. Therefore, “artificial” centroids had to be added manually for the missing points, as if an aberration is introduced, as seen in Figure 8.7(b).

The centroids computed for the aberrated image were plotted on top of the eroded image together with the calibration centroids, as shown in Figure 8.8, to check for possible displacements. Note that this will be done for all three cases. After calculating the slopes plotted in Figure 8.9(a), the corresponding actuator coefficients to correct the errors were obtained and plotted in Figure 8.9(b). An observation was made about the coefficients, which is the fact that at the start, there seems to be an overshoot that has to be corrected for. This is expected as the system has sample delays between the WFS and the DM. The retrieved CL simulation image is given in Figure 8.6(b). As seen, still not all spots are detected by the WFS. This is due to the fact that the aberrations will never be completely corrected for. In fact, from the fibre-optics coupling performance, a coupling of 70% was retrieved. This still meets the initial requirements of attaining at least a fibre coupling of 40%. The end results for the fibre-optics coupling performance are summarised in Table 8.3.

Table 8.1: OOMAO performance results of the AO system with a PID-controller

Gains input	**Value PID**	**Value INDI**
K_p	-0.2	out= -0.75, in= -0.75
K_i	-250	out= -300, in= -12.5
K_d	-0.00015	-
Property	**Value PID**	**Value INDI**
$\mathbf{r_0}$= ***6 cm***		
Performance OL with fibre coupling, without atmosphere	94.4%	94.4%
Performance OL with fibre coupling, with atmosphere	79.6%	79.6%
Performance CL with fibre coupling, with atmosphere	82.7%	89.3%
Strehl ratio after CL	67.8%	72.5%
$\mathbf{r_0}$ = ***7.8 cm***		
Performance OL with fibre coupling, without atmosphere	94.4%	94.4%
Performance OL with fibre coupling, with atmosphere	77.3%	77.3%
Performance CL with fibre coupling, with atmosphere	84.52%	90.8%
Strehl ratio after CL	77.8%	85.2%
$\mathbf{r_0}$ = ***15.5 cm***		
Performance OL with fibre coupling, without atmosphere	94.4%	94.4%
Performance OL with fibre coupling, with atmosphere	89.9%	92.6%
Performance CL with fibre coupling, with atmosphere	91.0%	92.6%
Strehl ratio after CL	91.9%	95.1%
$\mathbf{r_0}$ = ***23.3 cm***		
Performance OL with fibre coupling, without atmosphere	92.7%	92.2%
Performance OL with fibre coupling, with atmosphere	92.7%	92.7%
Performance CL with fibre coupling, with atmosphere	90.7%	90.9%
Strehl ratio after CL	67.8%	70.7%

Table 8.2: Scaling of the atmospheric aberrations for the TOGS.

Property	**Lab environment**	**TOGS environment**
Diameter	9 mm (WFS aperture)	700 mm
Phase plate 1	r_0 = 1 mm	r_0 = 7.8 cm
Phase plate 2	r_0 = 2 mm	r_0 = 15.5 cm
Phase plate 3	r_0 = 3 mm	r_0 = 23.3 cm

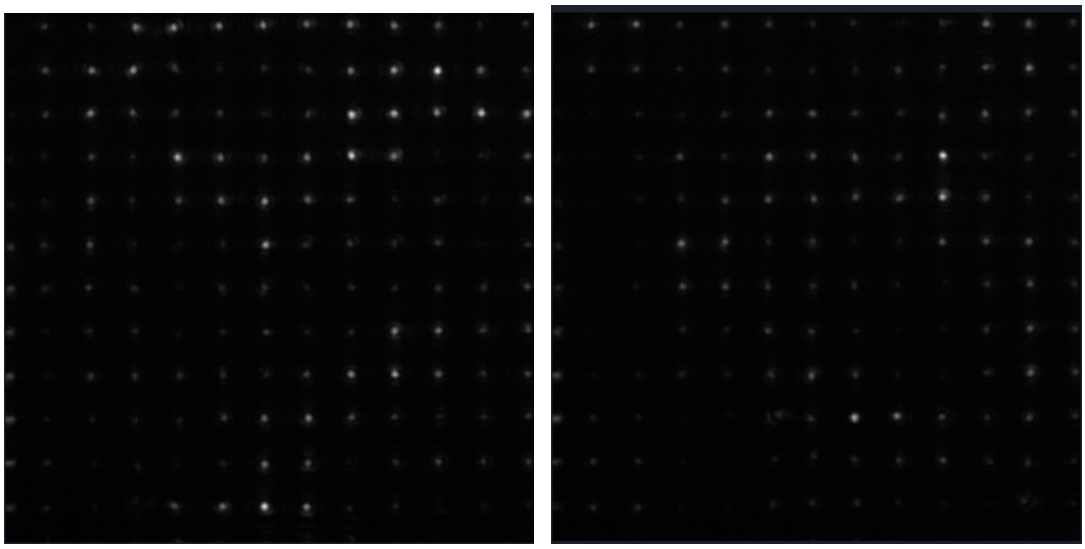

(a) OL aberrated image for r_0: 1mm (b) CL image for r_0: 1mm

Figure 8.6: Atmospheric simulations with an r_0: 1mm phase plate

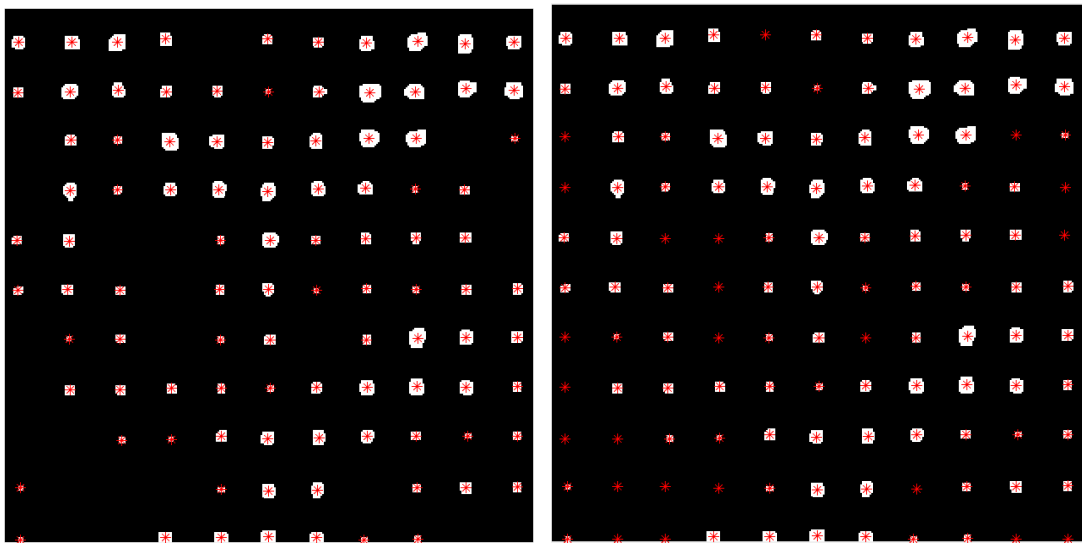

(a) Centroids obtained through image processing. (b) Added centroids to the aberrated image.

Figure 8.7: Image processing for r_0: 1mm

Table 8.3: fibre-optics coupling for aberrations with r_0: 1mm

Situation	**Measured light**	**fibre-optics coupling**
No aberrations	29.42 nW	100%
OL simulation	14.87 nW	50.5%
CL simulation	20.60 nW	70.0%

Phase plate r_0: 2mm

For a phase plate with r_0 = 2 mm, the aberrated OL simulation image retrieved is shown in Figure 8.10(a). Again, the processed image has been depicted in Figure 8.11(a). Note that

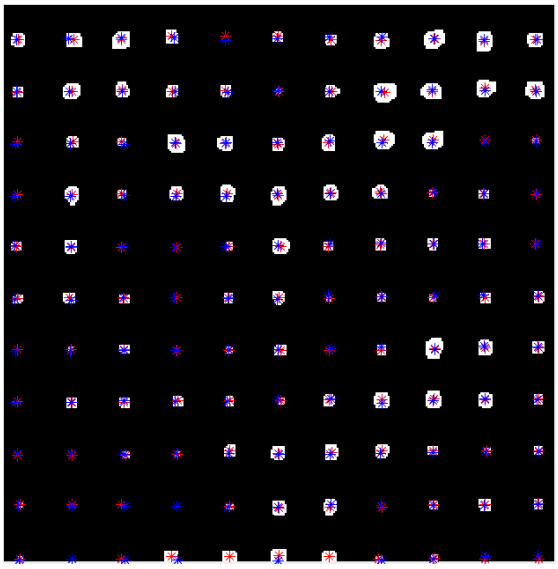

Figure 8.8: Comparison of the aberrated centroids with the calibration centroids.

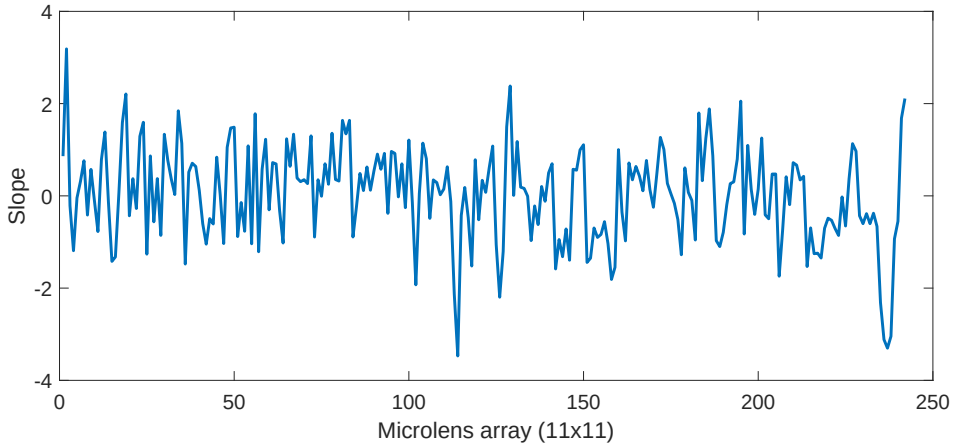

(a) Slopes measured by the WFS phase plate of r_0: 1mm

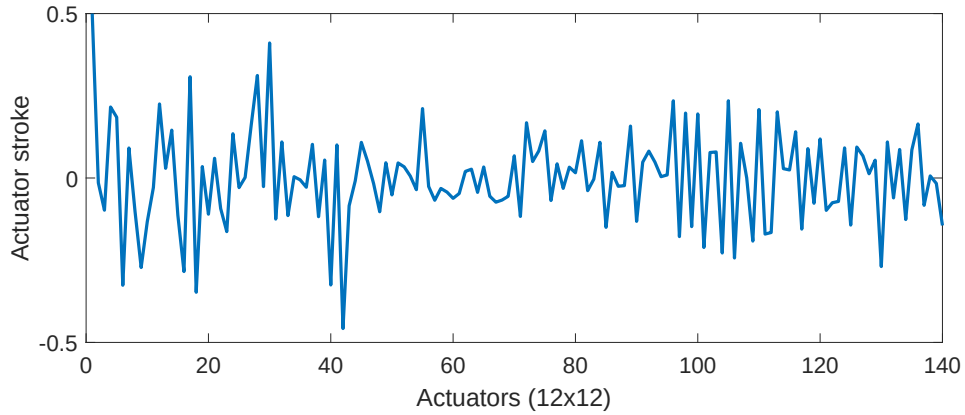

(b) Actuator coefficients to the DM for a phase plate of r_0: 1mm

Figure 8.9: Results of slopes and coefficients for r_0: 1mm.

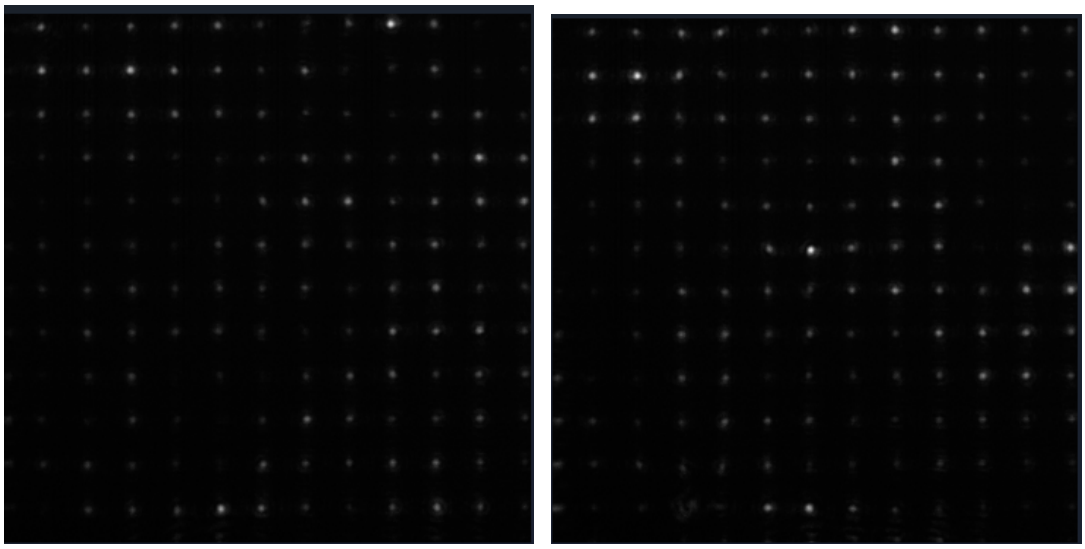

(a) Aberrated image for r_0: 2mm (b) Closed-loop image for r_0: 2mm

Figure 8.10: Atmospheric simulations with an r_0: 2mm phase plate

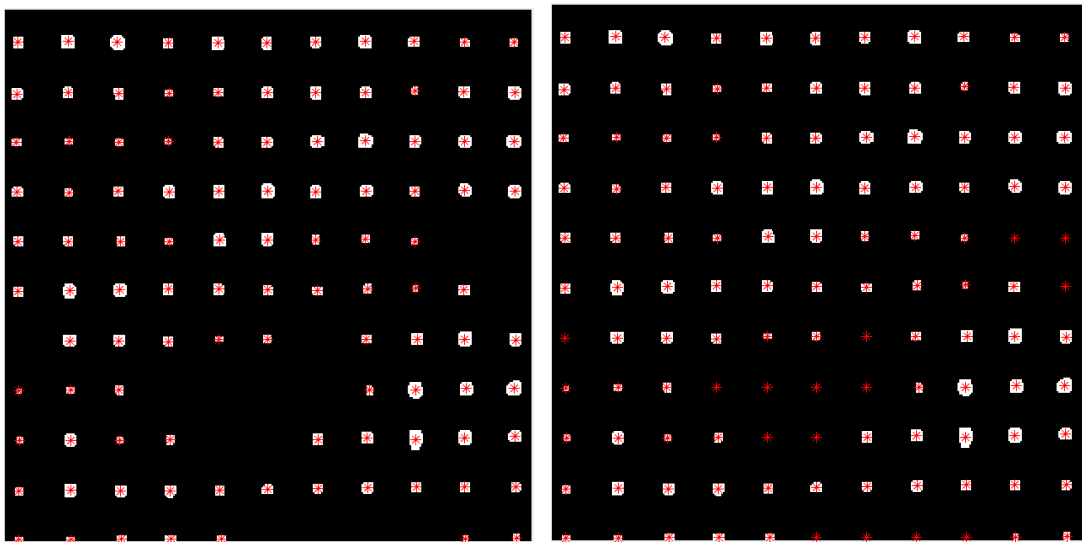

(a) Centroids obtained through image processing. (b) Added centroids to the aberrated image.

Figure 8.11: Image processing for r_0: 2mm

more spots have been detected than for the case of r_0 = 1 mm. This is related to the fact that fewer aberrations are introduced in this case. The aberrations cause the fibre-optics coupling to reduce to 55.2%, which is more than the achieved OL coupling with r_0 = 1 mm. Centroids were added manually for the points missing to simulate an aberration, as is seen in Figure 8.11(b).

The retrieved CL simulation image is given in Figure 8.10(b), which corresponds to a fibre-optics coupling performance of 85% was retrieved. As seen, the lower the aberrations present, the better the optical performance of the system. The end results for the fibre-optics coupling performance are summarised in Table 8.4.

Table 8.4: Fibre-optics coupling for aberrations with r_0: 2mm

Situation	Measured light	fibre-optics coupling
No aberrations	26.33 nW	100%
OL simulation	14.54 nW,	55.2%
CL simulation	22.37 nW	85.0%

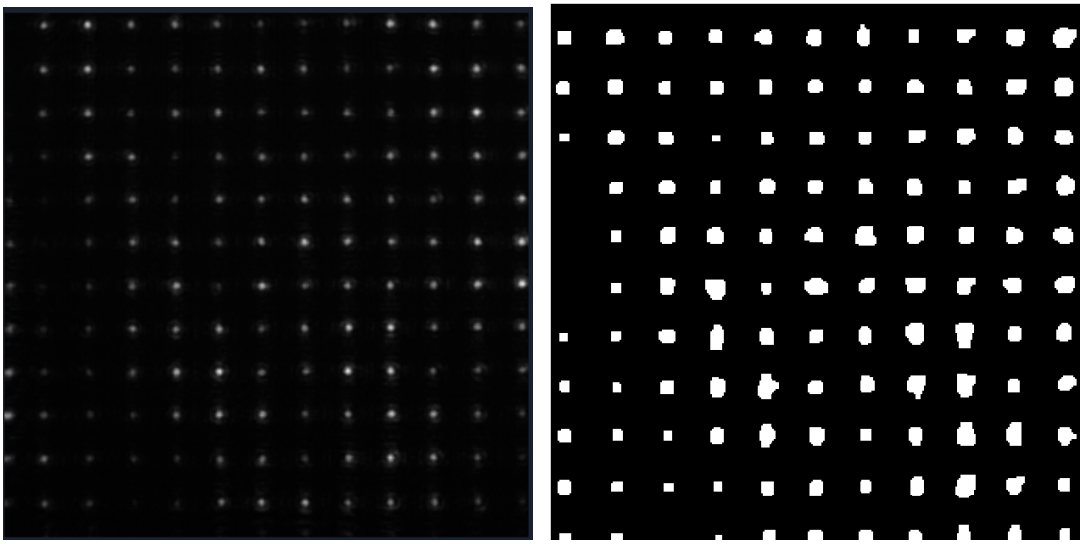

(a) Aberrated image for r_0: 3mm (b) Eroded image for r_0: 3mm

Figure 8.12: Atmospheric simulations with an r_0: 3mm phase plate

Phase plate r_0: 3mm

Experimental simulations were performed with a phase plate with r_0 = 3 mm, even if the r_0 for the atmospheric perturbations does not fall within the required range for the TOGS. The open-loop simulation image is given in Figure 8.12(a). From the processed eroded image seen in Figure 8.12(b), almost all points were detected, which is most likely due to the extremely low aberrations introduced. The image was processed and centroids were added manually in the same way as for the previous cases. The corresponding fibre-optics coupling performance with aberrations is equal to 60.6%, which is the highest coupling achieved when no corrections are introduced by the controller so far. After calculating the slopes plotted in Figure 8.13, the corresponding actuator coefficients to correct the errors were obtained and plotted in Figure 8.14(a). However, the closed-loop image corresponding to a maximum actuator stroke of 0.5 resulted in a severely low fibre-optics coupling performance equal to 14.4%. This is lower than the coupling achieved when no controller is introduced. Thus, the maximum actuator stroke was adjusted to 0.2, which resulted in the CL image seen in Figure 8.15(b) and a coupling of 57.1%. This is still lower than the coupling achieved in OL. Finally, the maximum actuator stroke was restricted to 0.1, resulting in the CL image depicted in Figure 8.15(c) and a final coupling performance of 74.7%. As seen, since the aberrations introduced were remarkably low, the initial actuator stroke coefficients were too high, which caused the spots in the spotfield image to break down as seen in Figure 8.15(a). This was solved by lowering the maximum actuator stroke. However, this would confirm that the relation between the slopes and the actuator stroke coefficients is not linear anymore.

Once more, an overshoot is present that had to be corrected for to account for the sample

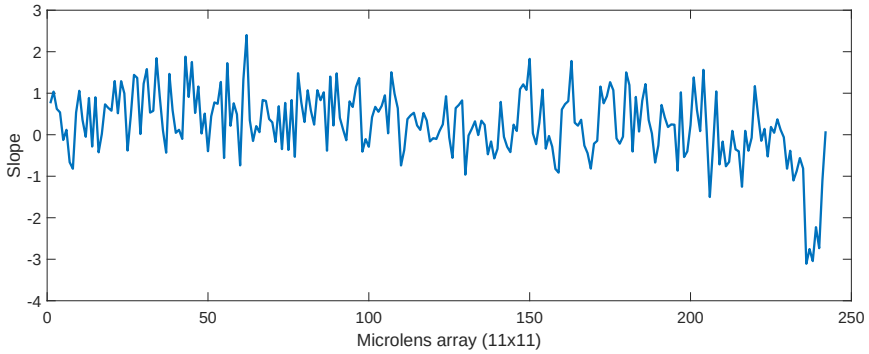

Figure 8.13: Results of slopes for r_0: 3mm.

Table 8.5: fibre-optics coupling for aberrations with r_0: 3mm

Situation	**Measured light**	**fibre-optics coupling**
No aberrations	26.88 nW	100%
OL simulation	16.28 nW	60.6%
CL simulation	max. actuator stroke of 0.5: 3.87 nW, max. actuator stroke of 0.2: 15.36 nW, max. actuator stroke of 0.1: 20.08 nW	14.4%, 57.1%, 74.7%

delays between the WFS and the DM. The DM coefficients are plotted for all three cases in Figures 8.14(a), 8.14(b), and 8.14(b), respectively. As seen, when the aberrations reach a minimum level, the optical performance degrades. The end results for the fibre-optics coupling performance are summarised in Table 8.5.

8.3 Differences between simulations and experimental results

The simulations conducted included the input parameters specifically defined for the HW components used for the TOGS, which are the same as the ones placed in the experimental set-up. Several differences were observed.

First, when comparing the shape of slopes obtained from the simulation results, as shown in Figure 6.17(a), with the shape of the ones from the experimental set-up shown in Figure 8.9(a), it is seen that much more noise is introduced in the measurements results. The presence of noise is already noticed when computing the interaction matrix and, subsequently, retrieving the command matrix as seen in Figure 6.14 and Figure 6.16, respectively. The noise remains along the entire CL simulation process, which results in noise in the final actuator coefficients.

Since there was no scientific camera installed in the experimental test set-up, the retrieved Strehl ratio from the simulations could not be compared against the ones that would result from the experimental test setup. However, the results from the fibre-optics coupling performance could be compared. From the simulations with r_0 = 7.8 cm, a fibre-optics coupling of 84.52% was achieved, which is 14.52% more than the one obtained in the experimental set-up. Subsequently, for r_0 = 15.5 cm and r_0 = 23.3 cm, the coupling was 4.9% and 18.3% more in the simulations, respectively. In real life, it is expected that the fibre-optics coupling performance is less than the one achieved in simulations, as more factors could influence the quality of the measurements. Note that an single-mode fibre will eventually be used in the TOGS, which is also what is modeled in the simulations. Now, the experimental

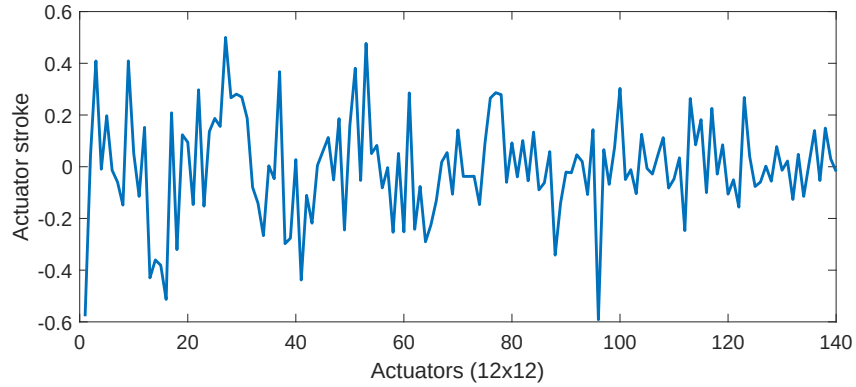

(a) Coefficients sent to the DM for phase plate of r_0: 3mm and a maximum stroke of 0.5.

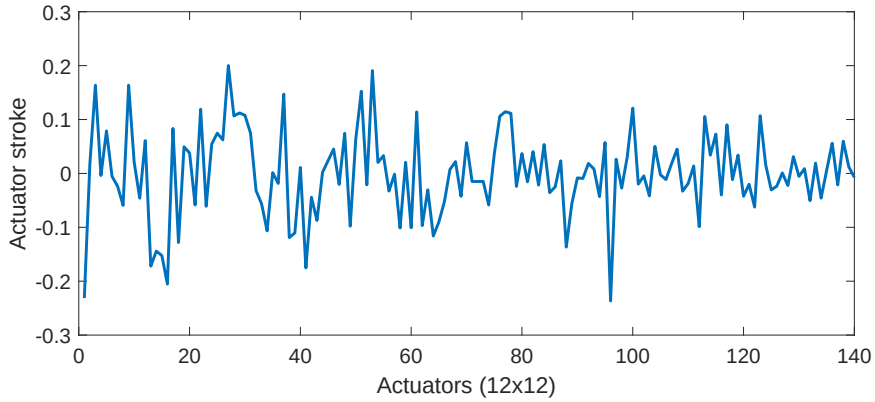

(b) Coefficients sent to the DM for phase plate of r_0: 3mm and a maximum stroke of 0.2.

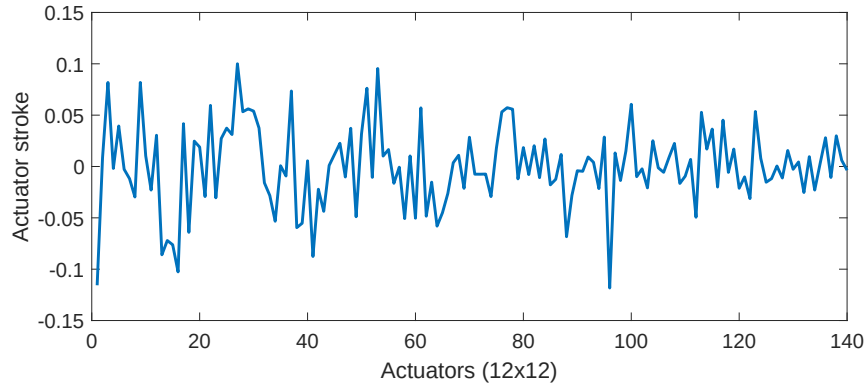

(c) Coefficients sent to the DM for phase plate of r_0: 3mm and a maximum stroke of 0.1.

Figure 8.14: Results of the coefficients for r_0: 3mm for all three actuation limits.

test set-up includes an multi-mode fibre because there was no SMF available. An MMF has a larger diameter than an SMF, which suggest that if the set-up would use an SMF instead of an MMF, the fibre-optics coupling would be reduced.

Reasons for the lowered fibre-optics coupling performance are listed below:

- The simulations assume an ideal Fried configuration, which suggest that the relation between the spot deviations and the actuator stroke is linear. As mentioned before, this is hard to achieve when the HW components are not manufactured, such that it

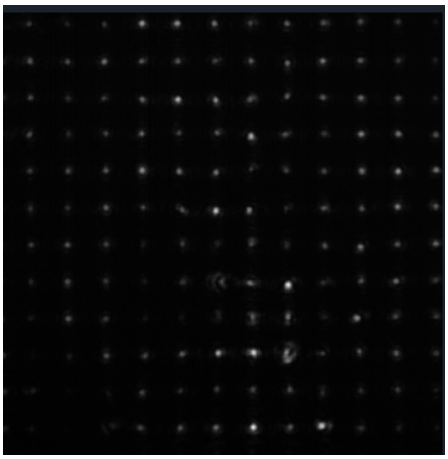

(a) Closed-loop image for r_0: 3mm and max. actuation of 0.5.

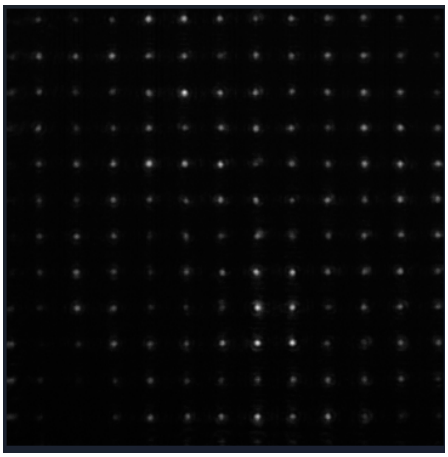

(b) Closed-loop image for r_0: 3mm and max. actuation of 0.2.

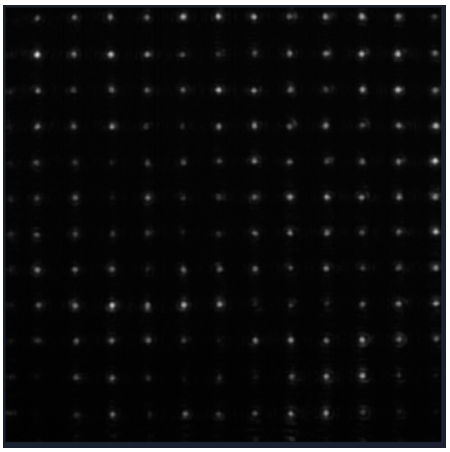

(c) Closed-loop image for r_0: 3mm and max. actuation of 0.1.

Figure 8.15: Closed-loop image for all three actuation limits with r_0: 3mm.

is intended to be used in the same set-up. Instead, the experimental set-up will show a non-linear relation between both, which is seen in the results. Moreover, this will cause alignment issues that can induce other types of aberrations, such as distortion and coma that was present in the images.

- Manufacturing errors, such as surface roughness of lenses, introduce aberrations in the image that are hard to correct for.
- Ideally, the spots should not disappear from the spotfield image when aberrations are introduced. Thus, the introduction of the missing centroids by hand cause inaccuracies in the slope-correction calculations.
- The HW errors introduced in the DM, such as settling time, could not be included in the OOMAO simulations. This results in additional noise that was not taken into account in the simulations.
- The simulations include the effect of the wind speed on the performance of the AO system. This is a factor that cannot be accounted for in the laboratory.

- The simulations assumed that the spots during calibration would fall exactly in the middle of each lenslet of the microlens array. During the calibration of the test set-up, it was proven that this was not the case due to a negative distortion present in the calibration image. Thus, when the actuation is too high, the spots could break and exit the lenslet, which serve as limits within the simulations. Therefore, only a maximum actuation stroke of 0.5 could be used during the CL simulations.

- Due to the system not being perfectly aligned and the distortion present as explained in Chapter 3, the incident wavefront is not planar and parallel to the plane of the lenslets. This is a property that the WFS does assume in the simulations and hen the depicting the spotfield image with Thorlabs' GUI.

- The MMF used in the experimental test set-up was previously (partially) burned by fellow colleagues in another test set-up, which reduced the quality of its performance.

Finally, both in the simulation results and in the experimental results, it was seen that when a high r_0 is applied, namely r_0 = 23.3 cm, the system reaches a saturation level and the correction provided by the control system results in a lower coupling performance than when no controller is used. The difference between the coupling performance in OL and CL is significantly smaller in the simulations than obtained with the experimental set-up.

When comparing the experimental test set-up to the final AO system used for the TOGS, several factors have to be taken into account, even if the same HW components placed in the experimental set-up will be used for the TOGS. First, the AO system in the laboratory is not connected to an actual telescope, which scales the incoming point source image. Moreover, the experimental set-up takes place within a controlled environment. In real life, the TOGS will experience uncontrolled atmospheric perturbations. Additionally, since the distance between the LGS and the WFS will significantly be increased, the incoming power of the laser will be altered. Also, other effects such as scintillation will take place, which is the variance in the irradiance from a beam caused by turbulence (Friedman and Miller, 2004). However, extrapolation of the data should result in similar results as the one obtained from the laboratory measurements. Nevertheless, the main difference between the experimental test-set-up and the TOGS, is that the results performed do not correspond to a real-time controller, which is what is eventually needed for the TOGS. This may affect the results remarkably.

CHAPTER

9 Conclusions and recommendations

The goal of this thesis was to design a controller for an Adaptive-Optics (AO) system that will be used for the new Transportable Optical Ground Station (TOGS) of IAC to enable inter-island quantum encrypted optical communication between the observatory of “el Teide” in Tenerife, and “el Roque de los Muchachos” observatory in la Palma. This thesis is supposed to answer the following research question:

What is the improvement of optical communication when decreasing the atmospheric aberrations with the use of adaptive optics?

This research question is what drives the thesis. To answer the above question, the research question is split into several sub-questions, which deal with the control of the instrument. These research questions are stated below and will be answered individually.

1. How can software implementations of the system help in predicting the controller performance of the deformable mirror within the adaptive-optics system?

To answer the first sub-question, software simulations were performed using the open source SW OOMAO. Here the AO system's components were simulated, such that it consisted of the same properties as the HW components used in the experimental set-up at a later stage. Starting from the most severe atmospheric turbulence, initially equal to a Fried parameter of r_0= 3 cm and a wind speed of 15 m/s, it was concluded from the simulations that the performance requirements would not be met under any circumstances due to the restrictions set by the properties of the HW components chosen for the AO system of the TOGS. More specifically, the performance requirements **TOGS-PR-07** and **TOGS-PR-04** stated to achieve at least a fibre-optics coupling performance as well as a Strehl of at least 40%. Nevertheless, a maximum fibre-optics coupling of 33.0% was obtained along with a Strehl ratio of 29.1% for these conditions. Hence, the atmospheric turbulence requirement was changed to a minimum Fried parameter of r_0 = 6 cm. After running the simulations with the adjusted parameters, it was observed that the system's performance increased with a decreasing atmospheric turbulence, meaning that the quality of the image defined with the Strehl ratio increased as well as the fibre-optics coupling performance. However, the quality of the corrections starts to deteriorate after reaching a certain maximum Fried parameter, where the atmospheric aberrations are almost zero. At this point, the retrieved fibre-optics coupling performance is less than the fibre-optics coupling performance achieved when atmospheric perturbations are present in an OL simulation, as was seen for the case where r_0 = 23.3 cm. This suggests

that the system becomes saturated below a certain minimum atmospheric turbulence.

2. What is the best way to steer a deformable mirror?

The second sub-question relates to possible control systems applied to steer the DM. The DM used during the experiments consisted of a mirror membrane supported by an underlying 12x12 actuator array. To correct for atmospheric aberrations, the actuators have to be controlled by computing the corresponding actuator strokes. The selected controller calculates the related actuator commands through the command matrix, which represents the relation between the measured WFS slopes (errors) and the DM actuator movements. In this thesis, the original controller, known as an I-controller, was first evaluated. From the sensitivity analysis, it was concluded that for the predefined atmospheric turbulence range and HW restrictions, the performance requirements were not met. Therefore, a PID-controller was designed and implemented. Once the sensitivity analysis was performed and a robust design was carried out to optimise the PID-controller performance, it was seen that the requirements were met. Moreover, the robust design concluded that the gains of K_p = -0.2, K_i = -250, K_d = -0.00015 resulted in the ideal performance where both the requirements were met, and the measurement noise was decreased. Furthermore, from the frequency analysis it was seen that the PID-controller corrected for the atmospheric aberrations, which is the frequency area of interest as the Zernike modes are dominant here. Additionally, it was proven that the designed PID-controller results in a robust system as the resonant peak of the rejection function does not exceed $|H_s|$<2.

3. To what extent can the controller performance be improved with the use of non-linear control techniques?

When comparing the results of the PID-controller with the INDI-controller for the same system, several aspects were observed. First, both controllers met the performance requirements, stating that a minimum of 40% fibre-optics coupling should be retrieved as well as a minimum Strehl ratio of 40%. However, after calculating the nominal gains for the INDI-controller and the PID-controller, the INDI-controller achieved a better coupling performance for all aberrations introduced. Second, when the minimum state deviation was plotted for both controllers, it was seen that the INDI-controller resulted in a smaller state deviation, suggesting that the error correction achieved is more precise with an INDI-controller than with a PID-controller. Third, after running the sensitivity analysis with the nominal gains, it was seen that the corresponding control effort for the INDI-controller is overall less than for the PID-controller. Finally, the frequency analysis performed on the INDI-controller resulted in similar results compared to the PID-controller, meaning that the INDI-controller also resulted in a robust system with the resonant peak of the rejection function being below $|H_s|$<2. Due to time constraints, no robust controller design was performed on the INDI-controller. Also, only the PID-controller was verified using the experimental set-up.

4. What kind of experimental set-up is needed to test the deformable mirror?

The next step answered the fourth sub-question, which corresponds to the experimental set-up to verify the performance of the designed PID-controller in a closed-loop simulation with the chosen HW components. The final test set-up is shown in Figure 9.1. As seen, it consisted of an LGS to simulate the point source, an atmospheric turbulence simulator, a DM, a WFS, and an MMF to retrieve the fibre-optics coupling performance. Once the system was properly calibrated, the CL simulations could be performed that resulted in the

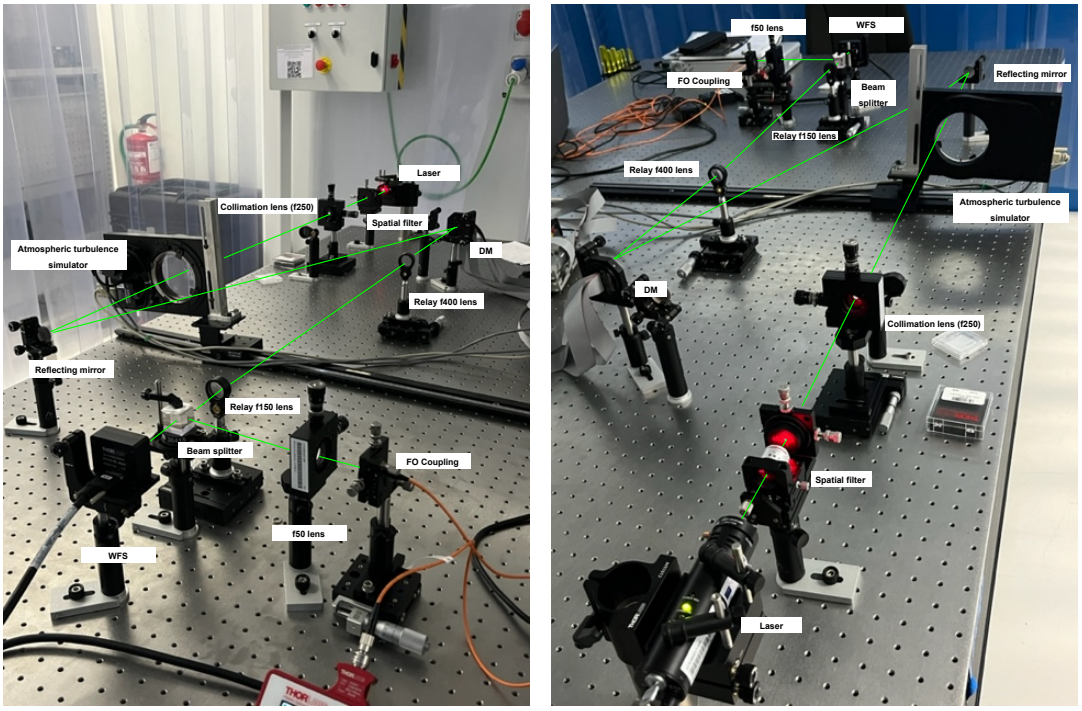

(a) Test set-up side view

(b) Test set-up front view

Figure 9.1: Final test set-up configuration.

following conclusions. The available phase plates allowed to test Fried parameters experienced by the TOGS equal to r_0 = 7.8 cm, r_0 = 15.5 cm, and r_0 = 23.3 cm. The results showed that, the fibre-optics coupling increased for r_0 = 15.5 cm (**85.0%**) compared to r_0 = 7.8 cm (**70.0%**), which is expected as the atmospheric aberrations are lowered. Moreover, for r_0 = 23.3 cm, the system reached a saturation level due to the atmospheric aberrations being almost non-existent, which caused the fibre-optics coupling (**14.4%**) to be below the initial OL fibre-optics coupling retrieved (**60.0%**) for a maximum actuator stroke of 0.5. The actuator stroke had to be limited to a maximum of 0.1 to increase the coupling to **74.4%**, suggesting that the behaviour of the system is not linear anymore. These results coincide with the observed behaviour of the AO system in the simulations carried out with OOMAO. However, the performance of the AO system within the experimental set-up is lower than the one obtained within the SW simulations, which is mostly due to the fact that the HW system was not perfectly aligned. This resulted in the system not meeting the assumed Fried configuration, nor the assumption of the incident wavefront being planar and parallel to the plane of the lenslets. Moreover, additional HW inaccuracies were not included in the simulations, which assumed an ideal system. Nevertheless, the retrieved fibre-optics coupling did meet the requirements.

5. Is the test set-up representative with respect to the transportable optical ground station?

The fifth and last sub-question refers to the compatibility of the experimental test set-up with the AO system used for the TOGS. As said before, the same HW components placed in the experimental set-up will be used for the TOGS. However, there are a view differences. First, the AO system in the laboratory is not connected to an actual telescope, which scales

the incoming point source image. Moreover, the the experimental set-up takes place within a controlled environment. In real life, the TOGS will experience uncontrolled atmospheric perturbation. Additionally, since the distance between the LGS and the WFS will significantly be increased, the incoming power of the laser will be altered, and other effects such as scintillation will take place. However, extrapolation of the data should result in similar results as the one obtained from the laboratory measurements. Finally, the biggest difference between the experimental test set-up and the TOGS, is that the results performed do not correspond to a real time controller, which is what is eventually needed for the TOGS.

Concerning making the controllers generic, the controllers are designed such that it could be applied to different AO systems with other HW components. The SW environment enables to change the properties of all the HW components previously mentioned, which allows to test the controllers in different systems. For example, properties that might change are the number of actuators, the maximum actuator stroke of the DM, the number of lenslets of the WFS, and the resolution. Thus, when another set-up is created in the laboratories, the controllers can be easily adapted to the changing conditions. However, the initial set-up considered included a plenoptics camera as WFS instead of a regular Shack-Hartmann. Since the object did not work correctly in the SW environment and the calibration of the component resulted to be extremely time consuming, it is not known whether these controllers would work with other types of WFS. Nevertheless, an attempt was made and the work performed is stated in Appendix A.

To conclude, the main research question can be answered as follows. The improvement of optical communication when decreasing the atmospheric aberrations with the use of AO, can be achieved by considering several factors. First, it was concluded from the simulations that the AO system increases the retrieved fibre-optics coupling performance as well as the image quality significantly compared to an OL simulation where AO is not used to correct for the aberrations. The improvements in the fibre-optics coupling performance was confirmed with an experimental test set-up that includes the same HW components intentionally chosen for the TOGS. However, the type of controller used to send the actuator commands to the DM, influences the performance of the AO-system. The designed INDI-controller resulted in the most improved performance compared to the initial I-controller and the designed PID-controller.

Future work recommendations

The designed controllers together with the other HW components resulted in preliminary results showing that the chosen AO-system meets the requirements of the TOGS. Nevertheless, there are several steps that have to be carried out further to make the system ready for the TOGS. After conducting the simulations and experimental tests, the following recommendations are suggested:

- Since OOMAO assumes a Fried configuration and an incident wavefront parallel and planar to the lenslets, the experimental test set-up should be adjusted such that, a relay specially manufactured for an AO system using Boston Micromachine's DM and Thorlabs' WFS20-5C is implemented to scale and align the system properly.

- Other configurations could be programmed into OOMAO and tested in an experimental test set-up, such as an AO system based on the Southwell geometry instead of the Fried configuration (Wang et al., 2017).

- In the simulations, the atmospheric perturbations are modeled based on the Kolmogrov theory. However, atmospheric perturbations are based on a random process. A method to optimise the atmospheric model would be to make a model predictive controller using a predictive model for the atmospheric perturbations based on neural networking.
- The CL system behaviour should be further studied for a step wise simulation, meaning that the phase plate is moved with a predefined time step using the Lexitec rotary stage, and a spotfield image is taken in every step. The controller should, subsequently, correct for the aberrations in every time step. To achieve this, the issue of the spots fading in the spotfield image when aberrations are introduced should be solved. Moreover, the computations of the centroids for each image should be ensured, such that no erroneous spots are detected and the displacements are corrected for automatically.
- Ideally, a plenoptics camera was intended to be used as WFS instead of a regular Shack-Hartmann. However, due to a malfunction in the model of the plenoptics camera when used in OOMAO that could not be solved, it was decided to change to a Shack-Hartmann WFS to ensure the retrieval of correct simulation results, which are crucial to have as a reference to compare the experimental results with. Nevertheless, the work performed using a plenoptics camera is documented in Appendix A.
- The INDI-controller showed to achieve better results than the PID-controller in the simulations performed. However, a non-linear controller on an actual AO system has never been tested before. The designed INDI-controller should be tested on the same experimental set-up used for the PID-controller to compare the results obtained and study its performance.
- The goal is to achieve a real-time controller that corrects for the aberrations in the TOGS continuously. Thus, the controller should be tested within the AO-system using a real-time controller. A SW platform that enables this option is the Durham Adaptive optics Real-time Controller (DARC) (Basden and Myers, 2012). However, this process is complex and time-consuming. Unfortunately, no time was left to apply a real-time controller to the system.
- The ultimate goal is to apply the entire real-time controller to the AO system of the actual TOGS that will be operated from the observatory of “el Teide”.

Bibliography

Basden, A. and Myers, R. (2012). "The Durham adaptive optics real-time controller: capability and Extremely Large Telescope suitability". *Monthly Notices of the Royal Astronomical Society* Vol. 424, No. 2, pp. 1483–1494.

Berkefeld, T., Soltau, D., Czichy, R., Fischer, E., Wandernoth, B., and Sodnik, Z. (2010). "Adaptive optics for satellite-to-ground laser communication at the 1m Telescope of the ESA Optical Ground Station, Tenerife, Spain". *SPIE Adaptive Optics Systems II*. 77364 C. San Diego, California, United States.

BostonMicromachines (2020). *Multi-D Deformable Mirror System User Manual, Rev. 5.2*. https://www.manualslib.com/manual/2755202/Boston-Multi-Dm.html.

Bunzli, J.-C. (2016). "Light Conversion: Lanthanide-Containing Systems". *Reference Module in Materials Science and Materials Engineering*. Elsevier.

Cameron, R. B. (1993). "Education Notes/Rubrique Pédagogique- Stellar Magnitudes and Photon Fluxes". *Journal of the Royal Astronomical Society of Canada* Vol. 87, No. 2, pp. 123–127.

Chen (2022). "Investigations of free space and deep space optical communication scenarios". *CEAS Space Journal* Vol. 14, pp. 357–364.

Chen, M., Liu, C., and Xian, H. (2015). "Experimental demonstration of single-mode fiber coupling over relatively strong turbulence with adaptive optics". *Applied optics* Vol. 54, No. 29, pp. 8722–8726.

Collins, L. (2013). "Chapter 19 - Optical Network Security". *Computer and Information Security Handbook*. Second Edition. Morgan Kaufmann, pp. 363–370.

Conan, R. and Correia, C. (2014). "Object-oriented Matlab adaptive optics toolbox". *Proc. SPIE 9148, Adaptive Optics Systems IV*. 91486C. Montreal, Quebec, Canada.

Emami-Naeini, A. and Powell, J. D. (2019). "Frequency-Response and Frequency-Domain Models". *Encyclopedia of Systems and Control*. Springer, pp. 1–9.

EoSens (2016). *High-Speed CMOS Camera*. https://mikrotron.de/en/mik-search.php.

Friedman, E. and Miller, J. L. (2004). "Photonics rules of thumb: optics, electro-optics, fiber optics, and lasers". McGraw-Hill Education.

Garcia-Talavera, M. R., Chueca, S., Alonso, A., Viera, T., and Sodnik, Z. (2002). "Analysis of the preliminary optical links between ARTEMIS and the Optical Ground Station". *Free-Space Laser Communication and Laser Imaging II*. Vol. 4821. SPIE proceedings. Seattle, WA, United States, pp. 33–43.

Guenther, B. and Steel, D. (2018). "Encyclopedia of Modern Optics". Elsevier Inc.

Irbah, A., Borgnino, J., Djafer, D., Damé, L., and Keckhut, P. (2016). "Solar seeing monitor MISOLFA: A new method for estimating atmospheric turbulence parameters". *Astronomy & Astrophysics* Vol. 591, A150.

Jiang, P., Xu, J., Liang, Y., and Mao, H. (2016). "Plenoptic camera wavefront sensing with extended sources". *Journal of Modern Optics* Vol. 63, No. 16, pp. 1573–1578.

Johan, K. et al. (2008). "Feedback systems". *An Introduction for Scientists and Engineers*. Second edition. Princeton University Press.

Kamp, A. (2007). "Space Instrumentation Engineering". TU Delft, The Netherlands.

Kraus, A. D. and Welty, J. (2001). "Appendix A: Gamma and Bessel functions". *Extended Surface Heat Transfer*. John Wiley & Sons inc.

Liu, J., Muruganandan, V. A., Clare, R., Trujillo, M. C. R., and Weddell, S. J. (2020). "A tip-tilt mirror control system for partial image correction at UC mount john observatory". *IEEE 35th International Conference on Image and Vision Computing New Zealand (IVCNZ)*. IVCN-20264176.

Majumdar, A. K. (2019). "Optical wireless communications for broadband global internet connectivity". *Fundamentals and potential applications*. Elsevier Inc.

Max, C. (2014). "Lecture 4: Atmospheric turbulence". *Course ASTR 289: Adaptive optics*. UC Santa Cruz.

Mooij, E. (2012). "Robust design methodology for a re-entry guidance system". *AIAA Guidance, Navigation, and Control Conference and Exhibit*. AIAA-2001-4049. Montreal, Canada.

Mooij, E. (2023). "Dynamic Inversion Heat-Flux Tracking for Hypersonic Entry". *AIAA SCITECH 2023 Forum*. AIAA 2023-2499. San Diego, CA, United States.

Negrin, J. S., Ramos, L. F. R., Torras, J., Montilla, I., Alonso, Á., Chaves, P. G. de, and Rey, N. M. (2022). "Transportable ground station for QKD using adaptive optics". *Proc. SPIE 11993, Free-Space Laser Communications XXXIV*. 119930V. San Francisco, CA, United States.

Niu, K. and Tian, C. (2022). "Zernike polynomials and their applications". *Journal of Optics* Vol. 24 123001, No. 12, pp. 1–54.

Nussbaum, A. (2005). "Geometrical Optics: Lenses and Mirrors". *Encyclopedia of Modern Optics*. Elsevier inc.

Ottevaere, H. and Thienpont, H. (2005). "Optical microlenses". *Encyclopedia of Modern Optics*.

Pirandola, S. (2021). "Limits and security of free-space quantum communications". *American Physical Society: Physical Review Research* Vol. 3, No. 1, pp. 1–33.

Rey, N. M. (2019). "Pioneering the use of a plenoptic adaptive optics system for free space optical communications". PhD thesis. Universidad de La Laguna.

Reyes, M., Comeron, A., Alonso, A., Rodriguez, A., Rubio, J. A., Dios, V. F., Chueca, S., and Sodnik, Z. (2005). "Ground-to-satellite bidirectional laser links for validation of atmospheric turbulence model". *Proc. SPIE 5160, Free-Space Laser Communication and Active Laser Illumination III*. SPIE-506738. San Diego, CA, United States.

Sanchez, F. (1985). "Astronomy in the Canary Islands". *Vistas in Astronomy* Vol. 28, No. 2, pp. 417–430.

Sawhil, A. S., Singhal, Y., and Bhardwaj, P. (2018). "An overview of free space optical communication". *International Journal of Engineering Trends and Technology (IJETT)* Vol. 55, No. 3, pp. 120–125.

Shen, S.-Y., Dai, M.-W., Zheng, X.-T., Sun, Q.-Y., Guo, G.-C., and Han, Z.-F. (2019). "Free-space continuous-variable quantum key distribution of unidimensional Gaussian modulation using polarized coherent states in an urban environment". *American Physical Society: Physical Review Research* Vol. 100, No. 1, pp. 1–8.

Sidhu, J. S., Joshi, S. K., Gündoğan, M., Brougham, T., Lowndes, D., Mazzarella, L., Krutzik, M., Mohapatra, S., Dequal, D., Vallone, G., et al. (2021). "Advances in space quantum communications". *IET Quantum Communication* Vol. 2, No. 4, pp. 182–217.

Slavic, J., Boltezar, M., Mrsnik, M., Cesnik, M., and Javh, J. (2020). "Vibration Fatigue by Spectral Methods: From Structural Dynamics to Fatigue Damage–Theory and Experiments". *From Structural Dynamics to Fatigue Damage - Theory and Experiments*. Elsevier inc.

Solomon Jr, O. M. (1991). "PSD computations using Welch's method". *NASA STI/Recon Technical Report*, SAND91–1533.

Spohn, T., Breuer, D., and Johnson, T. (2014). "Encyclopedia of the solar system". Elsevier inc.

Thorlabs (2020a). *Adaptive Optics Kit: Programmer's API Guide*. https://www.thorlabs.com/newgrouppage9.cfm?objectgroup_id=3208.

Thorlabs (2020b). *LDM series Laser Diode Modules: User Guide*. https://www.thorlabs.de/catalogpages/V21/1281.PDF.

Tyson, R. K. and Frazier, B. W. (2022). "Principles of adaptive optics". CRC press.

Uddin, M. and Chan, H. (2011). "8 - Adhesive technology for photonics". *Advanced Adhesives in Electronics*. Woodhead Publishing, pp. 214–258.

Wang, L., Lin, X., Liu, X., and Wei, P. (2017). "Adaptive optics system based on the Southwell geometry and Improvement on control stability". *Optics Communications* Vol. 390, No. 1, pp. 105–110.

Xiang, J. (2012). "Accurate compensation of the low-frequency components for the FFT-based turbulent phase screen". *Optics express* Vol. 20, No. 1, pp. 681–687.

Young, M. (2003). "Imaging optics". *Encyclopedia of Physical Science and Technology*. Elsevier inc.

APPENDIX

A Plenoptics camera as wavefront sensor

In the initial set-up for the TOGS, a plenoptics camera was considered as a WFS instead of a Shack-Hartmann. However, this option was later discarded because of a malfunction in the code that modelled the plenoptics camera within OOMAO and due to alignment issues in the laboratory. Due to time constraints, it was decided to switch to a Shack-Hartmann WFS. In this Appendix, the work performed with a plenoptics camera during the thesis is documented. In Section A.1, the plenoptics camera model initially used in OOMAO is explained. Then, Section A.2 describes the actual HW component used for the plenoptics camera in the experimental set-up. Finally, Section A.3 will discuss the calibration tests performed for the experimental test set-up with the plenoptics camera.

A.1 Plenoptics camera model

The plenoptics camera as WFS consists of a lenslet array placed in the focal plane of the telescope. Each lenslet re-images the aperture and forms a low-resolution image of the aperture. It is recommended to match the f-number of the lenslet to the telescope to obtain pupil images that do not overlap. Every pupil coordinate is imaged in the corresponding position on the detector, but through a different lenslet depending on the angle of arrival.

The image associated with every pupil point can then be reconstructed by post-processing the plenoptic image, selecting the value of the corresponding coordinate at every pupil image and building an image with all of them. This is a very important result because the recomposed sub-image of every single part of the aperture will allow to compute the local slope, and reconstruct the wavefront in the same way that a conventional Shack–Hartmann sensor would do.

The wavefront at the pupil can be extracted from the relative displacement of the recomposed sub-images from every pupil coordinate. This relative displacement can be calculated by correlating the recomposed sub-image to a reference image (Jiang et al., 2016):

$$C(u,v) = \sum_{i,j} I_m\left(x_i, y_j\right) I_r\left(x_i + u, y_j + v\right) \tag{A.1}$$

where $I_r\left(x_i + u, y_j + v\right)$ is the reference image, $I_m\left(x_i, y_j\right)$ is one of the recomposed sub-images and (u, v) is the shift between sub-image and the reference image. Equation (A.1) can also be calculated with the FFT. A simple way to select a reference image is to use one of the sub-images.

Sub-pixel precision can be achieved by fitting $C[u, v]$ to an analytic function and finding the location of its maximum value. For example, if $C[u_p, v_p]$ is the location of maximum

correlation, parabolic interpolation can be used to estimate relative displacement $[u_m, v_m]$ with sub-pixel precision,

$$u_m = u_p + \frac{1}{2}\frac{C(u_p+1, v_p) - C(u_p-1, v_p)}{C(u_p+1, v_p) + C(u_p-1, v_p) - 2C(u_p, v_p)} \tag{A.2}$$

A similar equation is also used to estimate v_m of the y-axis. As all the displacements of sub-images are measured relative to location of the reference image, it introduces a bias or global tilt to all the slope measurements.

To model the plenoptics camera, the object oriented model created by Rey (2019) will be used, which is explained below.

When a plenoptics image is taken, the image has to be reconstructed, as every part of the aperture has its equivalent in the plenoptic image. In Figure A.1, a typical aperture for a telescope is seen on the left side with an obscured zone due to the secondary mirror of the telescope. In the centre, a plenoptic image is presented with a certain number of microlenses and the pixels of the aperture that would correspond to each microlens. On the right, an example of the image reconstruction for this aperture is shown.

Figure A.2 shows how the architecture of the program works. Every microlens is divided with a mesh of points (green points in the figure) with the dimensions of $n_{subap} \times n_{subap}$, n_{subap} being the number of sub-apertures. The values of the pixels that fall within the points of the mesh are saved for each microlens. Once these values are retrieved, the pixels corresponding to the points of the mesh of all microlenses are grouped to form an image with the amount of pixels equal to the amount of microlenses. In total, there will be $n_{subap} \times n_{subap}$ images of these type that will form the final image.

A.2 Plenoptics camera in experimental test set-up

The camera used is Mikrotron GmbH EoSens GE Camera and its properties are listed in Table A.2. Placing a microlens array before the camera will enable to use the camera as a plenoptics sensor when a microlens is placed in front of the aperture (EoSens, 2016).

A.3 Calibration of AO system with plenoptics camera

During the calibration process, a different set up will be made seen in Figure A.3. Here, a

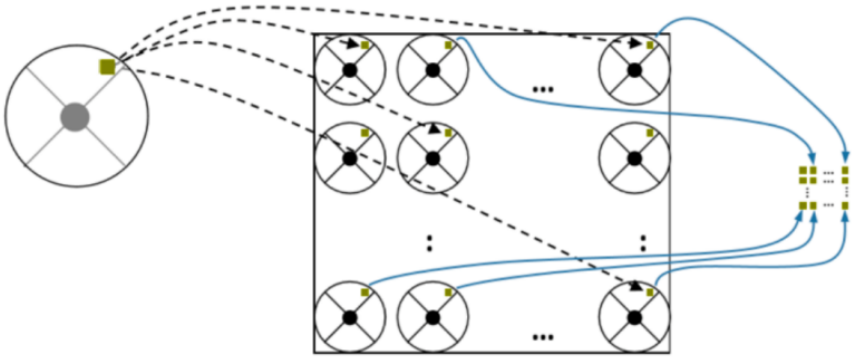

Figure A.1: Scheme of the plenoptic image reconstruction (Rey, 2019)

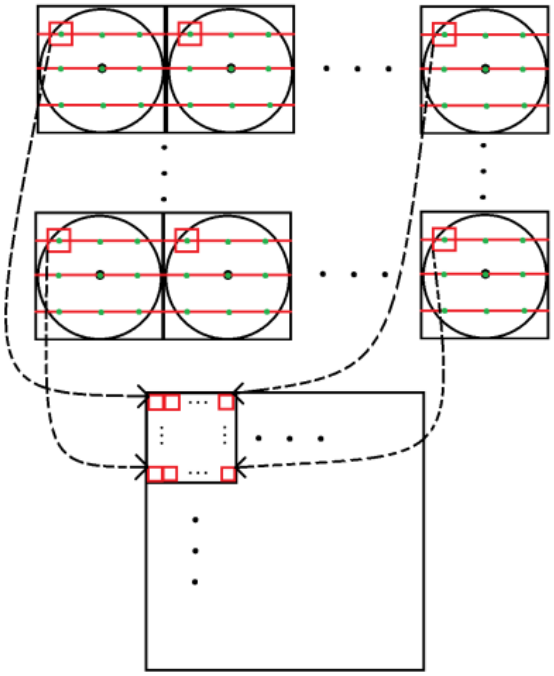

Figure A.2: Scheme of the plenoptic image reconstruction in the program (Rey, 2019).

Table A.1: The input parameters and properties of the plenoptic object created by OOMAO.

Input Parameters	**Parameter name**	**Input TOGS**
required	Lenslets	11
	Resolution	Same as telescope
	Focal length	0.2 m
	Sensor size	Same as telescope
	Diameter	0.7 m
	Telescope pupil	Call from telescope
Output parameters	Slopes	
	Noise	

regular flashlight as light source is used that was shined upon a blank paper to ensure a uniform distributed light source. The light is then reflected back to the optical path of the system. The reflected light will pass through the objects as described in the first setup in Figure A.3. Note that the relay between the WFS and DM was not yet placed within the test set-up as, at that moment, it was not yet deemed to be necessary.

The light would then be measured by the wavefront sensor using the software provided by GE Mikrotron. Its GUI allows to create a spotfield of the pupils as seen in Figure A.4(a), which will serve as the calibration image. This image will pass through a code that calculates the centroids of each of the concerned pupils using imaging processing, which results in the image seen in Figure A.4(b). The centroids will serve as a reference point when no aberrations are present. As seen, the selected pupils are less than the total pupils available from the calibration image. This is due to the fact that, when using a point source, such as a laser or a star, the number of illuminated pupils will be less than the case where a dispersed light is used. After obtaining the centroids in the x- and y-direction for all selected pupils, the pitch between the pupils as well as the inclination is calculated. The pitch, p, is the minimum

Table A.2: The properties of Mikrotron's EoSens GE Camera (EoSens, 2016).

Property	**Value**
Number of pixels, pixel size	1280 x 1024, 14 μm
Wavelength range	370-670 nm
Active area	17.92 (H) mm x 14.34 (V) mm
Full frame rate	81 fps
Fill factor	40%
Sensitivity	25 V/lux.s @ 550 nm
Dark current	90 dB
Pixel saturation level	30000 e-
QE x FF	35% @ 550 nm
Framerate and shutter timebase accuracy	± 50 ppm
Shock and vibration	70g, 7 grms
Dimensions	63 mm x 63 mm x 47 mm
Weight	300 g
BrightPix	< 10
DarkMeanOutput	0<x<235
50%MeanOutp0ut	390<x<547
Fixed Pattern Noise	<3.1%
TotDefects	<20

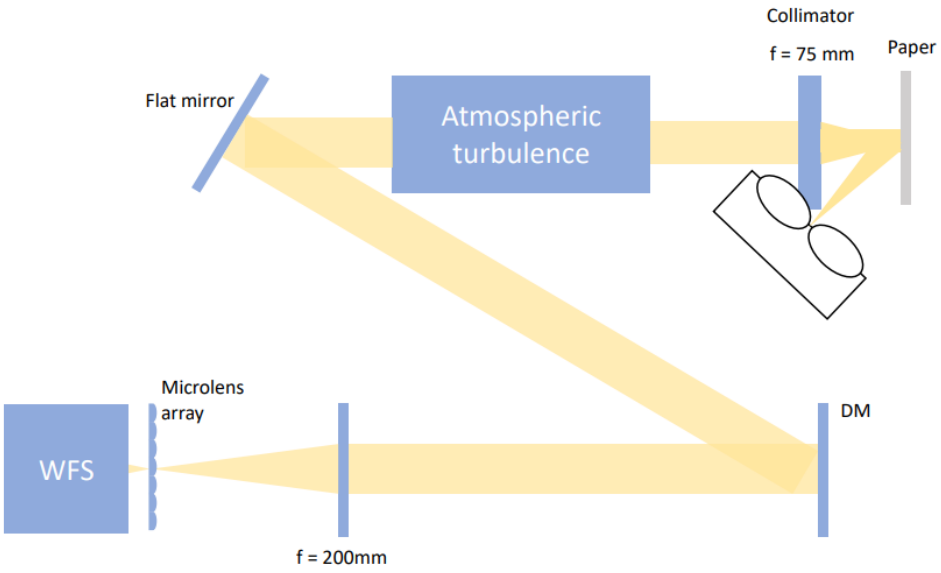

Figure A.3: Calibration set up with plenoptics camera

distance between pupils, which is the distance in diagonal in this case. Additionally, the inclination, i, is the angle between the x-axis horizontally and the path of the pupils. Selecting

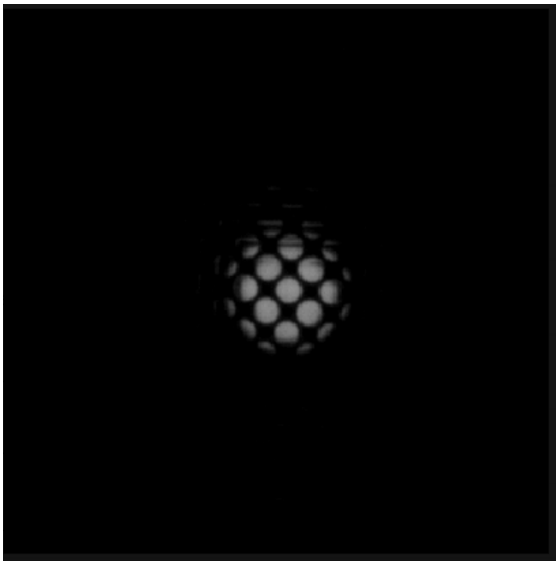

(a) Raw spot field image recreated for the calibration of a plenoptics camera

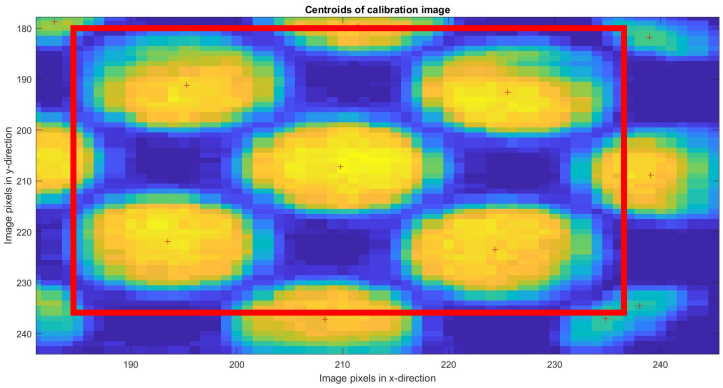

(b) Centroids of the calibration pupil for the selected pupils.

Figure A.4: Calibration image processing steps for the plenoptic camera.

two pupils as the reference, these parameters are calculated as follows:

$$\begin{aligned} p &= \sqrt{(C_{x1} - C_{x2})^2 + \left(C_{y1} - C_{y2}\right)^2} \\ i &= \tan^{-1}\left(\frac{C_{y1} - C_{y2}}{p}\right) \end{aligned} \tag{A.3}$$

The calibration process was encountered with many difficulties:

- When a diffused light source was used that was reflected against a white paper, the sensor did not detect the light.

  After a while, the discovery was made that the exposure time had to be increased to allow the sensor more time to detect the light.

- In the first set-up, the Thorlabs WFS20-5C Shack-Hartmann was used as plenoptics camera. but without its microlens array. However, when the laser was used as light source, the pupils were poorly detected by the sensor and did not have a round shape.

Therefore, the centroids were badly calculated by the code used to reconstruct the interaction matrix.

To solve this, the interaction matrix was considered to be reconstructed using a white light shining on a letter instead of a laser. This letter would be detected by the camera. However, to do this, the DM had to be moved into the pupil, which meant changing the whole set-up again.

Due to time constraints, it was decided to change the camera to the Mikrotron Eosens GE camera, where a microlens array was placed in front of the camera lens. The camera would then function as a plenoptics camera. Moreover, the lens placed in front of the camera was replaced from a single lens to a doublet, which reduced the aberrations. This solved the issue, but the alignment of the set up had to be redone partly.

- To reconstruct the calibration matrix, a flat mirror was initially used instead of the deformable mirror to ensure the source would not deflect due to the mirror surface not being flat. However, this caused alignment issues when reintroducing the deformable mirror to obtain the interaction matrix, as the illuminated pupils were shifted in centroids. More specifically, the calibration image should include the same centroids for the pupils as when the poke matrix is created.

  To solve this issue, the set up was readjusted and the deformable mirror was used to retrieve the calibration image, but all actuators were forced to have stroke equal to zero.

Furthermore, during the calibration process, other verification tests were performed. These tests are listed in Table A.3. One test failed, which is number **PC-01** related to the illumination of the laser. The laser did not illuminate uniformly. Two lasers were only available in the laboratory and both were installed, which required alignment of the set up twice. However, none of them passed the test. This means that this effect has to be accounted for in the results, especially when the pupils are not illuminated equally.

Table A.3: Verification of calibration set up.

ID	Test	Tools/Method	P/F
PC-01	Calibration light should illuminate lenslets uniformly.	Check the spotfield visually obtained from the GUI.	F
PC-02	The calibration image should include the centroid position correctly.	Check image obtained from the Matlab program.	P
PC-03	The lenslets should not overlap.	Check the spotfield obtained from the GUI, and adjust the lens aperture.	P
PC-04	The beam width of the laser should not change with increasing distance (collimated)	Visually check with a piece of paper that reflects laser.	P
PC-05	The lenslets should be round.	Check the spotfield obtained from the GUI.	P
PC-06	The values of pitch and the inclination of the calibration image will be checked by hand.	-	P
PC-07	The lenslets should be illuminated uniformly	Check the spotfield visually obtained from the GUI.	P
PC-08	The laser should illuminate four lenslet arrays in the centre.	Check the spotfield visually obtained from the GUI.	P
PC-09	The lenslets should be round.	Check the spotfield visually obtained from the GUI. Adjust focal length of lens, and alignment.	P
PC-10	The illuminated lenslets should change according when actuators of the DM are being moved.	Check the spotfield visually obtained from the GUI.	P
PC-11	The WFS measurements should not become saturated.	Check the spotfield visually obtained from the GUI. Adjust with filters.	P
PC-12	The WFS, including the lens and camera, should be aligned with its optical path.	A focaliser is placed in front of the laser and then at the end of the table. The laser should pass both times through the centre.	P